ABSTRACT

Title of dissertation: NONEQUILIBRIUM DYNAMICS IN OPEN QUANTUM SYSTEMS

Jeremy T. Young
Doctor of Philosophy, 2019

Dissertation directed by: Professor Alexey V. Gorshkov
Department of Physics

Professor Mohammad F. Maghrebi
Department of Physics and Astronomy
Michigan State University

Due to the variety of tools available to control atomic, molecular, and optical (AMO) systems, they provide a versatile platform for studying many-body physics, quantum simulation, and quantum computation. Although extensive efforts are employed to reduce coupling between the system and the environment, the effects of the environment can never fully be avoided, so it is important to develop a comprehensive understanding of open quantum systems. The system-environment coupling often leads to loss via dissipation, which can be countered by a coherent drive. Open quantum systems subject to dissipation and drive are known as driven-dissipative systems, and they provide an excellent platform for studying many-body nonequilibrium physics.

The first part of this dissertation will focus on driven-dissipative phase transitions. Despite the nonequilibrium nature of these systems, the corresponding phase

transitions tend to exhibit emergent equilibrium behavior. However, we will show that in the vicinity of a multicritical point where multiple phase transitions intersect, genuinely nonequilibrium criticality can emerge, even though the individual phase transitions on their own exhibit equilibrium criticality. These nonequilibrium multicritical points can exhibit a variety of exotic phenomena not possible for their equilibrium counterparts, including the emergence of complex critical exponents, which lead to discrete scale invariance and spiraling phase boundaries. Furthermore, the Liouvillian gap can take on complex values, and the fluctuation-dissipation theorem is violated, corresponding to an effective temperature which gets "hotter" and "hotter" at longer and longer wavelengths.

The second part of this dissertation will focus on Rydberg atoms. In particular, we study how the spontaneous generation of contaminant Rydberg states drastically modifies the behavior of a driven-dissipative Rydberg system due to the resultant dipole-dipole interactions. These interactions lead to a complicated competition of both blockade and anti-blockade effects, leading to strongly enhanced Rydberg populations for far-detuned drive and reduced Rydberg populations for resonant drive.

NONEQUILIBRIUM DYNAMICS IN OPEN QUANTUM SYSTEMS

by

Jeremy T. Young

Dissertation submitted to the Faculty of the Graduate School of the
University of Maryland, College Park in partial fulfillment
of the requirements for the degree of
Doctor of Philosophy
2019

Advisory Committee:
Professor Steven L. Rolston, Chair
Professor Alexey V. Gorshkov, Advisor
Professor Mohammad F. Maghrebi, Advisor
Professor Mohammad Hafezi, Dean's Representative
Professor Maissam Barkeshli

Acknowledgments

Although countless people have been involved in getting me to this point, it is impossible to list them all. Below, I would like to acknowledge some of the people who have had the most direct impact on my studies during my time as a graduate student.

I would first like to thank my advisors Alexey Gorshkov and Mohammad Maghrebi, both of whom have made major contributions to the work presented in this dissertation as well as my development as a scientist. Alexey has always been enthusiastic in his support of my research, and Mohammad was always willing to teach me new concepts in spite of the distance between our universities. Many other professors here have also been crucial in helping me get to where I am today, including Trey Porto, Ian Spielman, and the members of my committee: Steve Rolston, Mohammad Hafezi, and Maissam Barkeshli.

During my time here, I have been fortunate to learn from and collaborate with many postdocs, including Przemek Bienias, Igor Boettcher, Thomas Boulier, Michael Foss-Feig, Jim Garrison, Elizabeth Goldschmidt, Zhexuan Gong, Anzi Hu, Rex Lundgren, Seth Whitsitt, and Ryan Wilson. I have also had the opportunity to get to know and learn from many graduate students as well. Among them, I'd like to acknowledge several people whose collaborations and conversations I have benefited from: Ron Belyansky, Abhinav Deshpande, Zach Eldredge, Hilary Hurst, Eric Magnan, Pradeep Niroula, and Yidan Wang, as well as my officemates Su-Kuan Chu, Jon Curtis, Ranchu Matthew, and Ali Hamed Moosavian.

I would like to conclude by thanking some of the people I have known outside of my graduate studies. My family has continued to support me in various ways throughout my life, and I wouldn't be here without them. I also greatly appreciate the support and friendship of Jacky Chong, Kuo Tan, and Michael Zhuang, as well as many others throughout my life. Finally, I would like to thank Amritha Mallikarjun for her love and support and always being there for me.

Table of Contents

Acknowledgements ii

Table of Contents iv

List of Tables vi

List of Figures vii

Citations to Previously Published Work ix

1 Introduction 1
1.1 Motivation . . . 1
1.2 Driven-Dissipative Systems . . . 2
1.3 Critical Phenomena . . . 6
1.4 Rydberg Atoms . . . 14
1.5 Outline of Dissertation . . . 19

2 Nonequilibrium fixed points of coupled Ising models 21
2.1 Introduction . . . 21
2.2 Main Results . . . 25
2.2.1 Scaling Phenomena . . . 31
2.2.2 Phase Diagram . . . 36
2.2.3 Spectral Properties . . . 38
2.3 Model . . . 40
2.3.1 Mean Field Theory . . . 41
2.3.2 Nonequilibrium Ising Model for Two Fields . . . 47
2.4 Renormalization Group Analysis . . . 49
2.4.1 RG Equations . . . 50
2.4.2 Fixed Points of RG Flow . . . 59
2.4.3 Universal Scaling Behavior . . . 62
2.4.4 Phase Diagram . . . 69
2.4.5 Liouvillian Gap Closure . . . 72
2.5 Experimental Realization . . . 76
2.6 Conclusion and Outlook . . . 78

3 Dissipation-Induced Dipole Blockade and Antiblockade in Driven Rydberg Systems 81
3.1 Introduction . . . 81
3.2 Theoretical Models . . . 86
3.2.1 Cumulant expansion . . . 89
3.2.2 Inhomogeneous Rate Equations . . . 91
3.3 Cumulant Expansion Results . . . 92
3.3.1 Divergences . . . 92
3.3.2 Blockade Radius Reduction . . . 96
3.3.3 Rydberg Population Scaling . . . 101
3.4 Rate Equation Results . . . 105
3.5 Conclusion and Outlook . . . 112

A Appendices to Chapter 2 114
A.1 Langevin Equations Near the Multicritical Points . . . 114
A.2 Redundant Operators . . . 119
A.3 Perturbative RG . . . 123
A.3.1 Diagrammatic Techniques . . . 124
A.3.2 One-Loop Diagrams . . . 125
A.3.2.1 Mass Terms . . . 125
A.3.2.2 Coupling Terms . . . 127
A.3.3 Two-Loop Diagrams . . . 129
A.4 Method of Characteristics . . . 136

B Appendices to Chapter 3 140
B.1 Gutzwiller Mean Field Theory . . . 140
B.2 Cumulant Expansion Equations of Motion . . . 142
B.3 Quantum Trajectories . . . 144
B.4 Comparison of Different Rate Equation Approaches . . . 146
B.5 Experimental Methods . . . 148

Bibliography 151

List of Tables

2.1 Fixed point values of the coupling coefficients and critical exponents to the lowest order. 67

A.1 Langevin equation parameters for soft modes ϕ_1, ϕ_2 117

List of Figures

1.1 Block-spin renormalization. 8
1.2 Block-spin renormalization of Ising model. 9
1.3 Qualitative illustration of a Rydberg atom. 16
1.4 Rydberg blockade and antiblockade 18

2.1 Schematic illustration of the physical setup. 24
2.2 A schematic RG flow diagram projected to the g_{12}-g_{21} plane. 30
2.3 Summary of the main features of the NEFPs contrasted with effective EFPs. 33
2.4 Phase diagram associated with the NEFPs of the nonequilibrium Ising model of two coupled fields for $h = 0$. 37
2.5 Mean field dynamics near the NEFP within the doubly ordered phase with $|M_1| = |M_2|$. 40
2.6 Dynamics of gapped (fast/massive) and soft (slow/massless) modes. . 45
2.7 Phase diagram for (one of the two) the nonequilibrium tetracritical points as a function of effective mass terms and magnetic field. 71

3.1 Theoretical three-level system. 83
3.2 Approximate divergence diagrams for cumulant expansion in 3D. . . . 93
3.3 Rydberg population fits in divergent regions. 95
3.4 Steady state correlations between s and p atoms. 99
3.5 Blockade radius reduction. 100
3.6 Rydberg population scaling as a function of interaction strength. . . . 102
3.7 Quadratic to linear scaling crossover for the cumulant expansion. . . . 103
3.8 Quadratic to linear scaling crossover in experiment. 104
3.9 Resonant Rydberg population time dependence for inhomogeneous rate equations. 107
3.10 Near-Lorentzian lineshapes from inhomogeneous rate equations. . . . 108
3.11 Resonant steady-state s population scaling as a function of Rabi frequency and interaction strength. 109
3.12 Steady-state linewidth scaling as a function of Rabi frequency and interaction strength. 110
3.13 Scaling coefficients as a function of $(\gamma_p/\gamma_R)^{1/2}$. 111

A.1 Diagrammatic representation of Gaussian propagators. 124
A.2 Interaction vertices. 125
A.3 One-loop corrections to $r_1\phi_1\tilde{\phi}_1$. 126
A.4 One-loop corrections to $u_1\phi_1^3\tilde{\phi}_1$. 128
A.5 One-loop corrections to $u_{12}\phi_2^2\phi_1\tilde{\phi}_1$. 128
A.6 Two-loop corrections to γ_1 and D_1. 130
A.7 A generic internal two-loop diagram leading to a renormalization of γ_i and D_i. 131
A.8 Two-loop corrections to $\gamma_1 T_1$. 133
A.9 Generic internal two-loop diagram leading to corrections to $\gamma_i T_i$. . . 134

B.1 Relative error of cumulant expansion with respect to quantum trajectories. 146
B.2 Example lineshapes for several implementations of decoherence. . . . 147
B.3 Experimental excitation and measurement scheme. 149

Citations to Previously Published Work

Much of the work presented in this dissertation has appeared in previously published papers. Here, we indicate those publications along with related work which is not presented in this dissertation.

- Chapter 2: "Non-equilibrium fixed points of coupled Ising models," J. T. Young, A. V. Gorshkov, M. Foss-Feig, and M. F. Maghrebi, arXiv:1903.0259 (2019), to appear in Phys. Rev. X.
  - Further work related to phase transitions in driven-dissipative phase transitions is presented in "Emergent equilibrium in many-body optical bistability," M. Foss-Feig, P.Niroula, J. T. Young, M. Hafezi, A. V. Gorshkov, R. M. Wilson, and M. F. Maghrebi, Phys. Rev. A **95**, 043826 (2017).
  - Further work related to determining the steady state of driven-dissipative systems is presented in "A solvable family of driven-dissipative many-body systems," M. Foss-Feig, J. T. Young, V. V. Albert, A. V. Gorshkov, and M. F. Maghrebi, Phys. Rev. Lett. **119**, 190402 (2017).
- Chapter 3: "Dissipation-induced dipole blockade and antiblockade in driven Rydberg systems," J. T. Young, T. Boulier, E. Magnan, E. A. Goldschmidt, R. M. Wilson, S. L. Rolston, J. V. Porto, and A. V. Gorshkov, Phys. Rev. A **97**, 023424 (2018).
  - Closely related experimental work on blockade and antiblockade in driven Rydberg systems is presented in "Anomalous Broadening in Driven Dis-

sipative Rydberg Systems," E. A. Goldschmidt, T. Boulier, R. C. Brown, S. B. Koller, J. T. Young, A. V. Gorshkov, S. L. Rolston, and J. V. Porto, Phys. Rev. Lett. **116**, 113001 (2016) as well as "Spontaneous avalanche dephasing in large Rydberg ensembles," T. Boulier, E. Magnan, C. Bracamontes, J. Maslek, E. A. Goldschmidt, J. T. Young, A. V. Gorshkov, S. L. Rolston, and J. V. Porto, Phys. Rev. A **96**, 053409 (2017).

– Further work related to using Rydberg atoms for quantum computation and simulation is presented in "Fast State Transfer and Entanglement Renormalization Using Long-Range Interactions," Z. Eldredge, Z.-X. Gong, J. T. Young, A. Hamed Moosavian, M. Foss-Feig, and A. V. Gorshkov, Phys. Rev. Lett. **119**, 170503 (2017) as well as "Nondestructive cooling of an atomic quantum register via Rydberg interactions," arXiv:1903.0259 (2019), to appear in Phys. Rev. Lett.

Chapter 1: Introduction

1.1 Motivation

In the past few decades, the fields of atomic, molecular, and optical (AMO) physics have undergone dramatic changes. These changes have been driven by rapid improvements in the ability to both prepare many-body systems, control the underlying physics governing their behavior, and to measure the resultant physics that emerges. These platforms include ultracold atoms in optical lattices [1, 2] or optical tweezers [3–5], trapped molecules [6–8], trapped ions [9, 10], and cavity arrays [11–13]. Collectively, these platforms have provided new avenues into exploring various forms of many-body quantum physics, a pursuit which had been previously confined primarily to condensed matter systems. These include new methods for studying quantum criticality [14, 15], topological phases of matter [16–19], quantum magnetism [20–22], and a variety of other types of many-body quantum systems [23]. Important new directions include long-range interactions [24–26] as well as the realization of photonic interactions and phases [13, 27]. As these systems provide an excellent platform for quantum simulation, it is natural that they also provide excellent platforms for quantum computation. Neutral atoms and trapped ions in particular are two of the most viable candidates for the creation of scalable quantum

computers [28–30], both of which have demonstrated high fidelity entangling gates experimentally [31–35].

Although extensive efforts are used to isolate AMO systems, in general there is usually some form of coupling to the environment. Thus when studying many-body physics in these systems, it is important to take into account the fact that these are open quantum systems. For example, if a quantum computation entails exciting atoms to their excited states, spontaneous emission can lead to errors in the final output. However, although the open nature of AMO systems is often viewed as a detrimental feature which tends to destroy interesting quantum effects, it can often lead to incredibly rich forms of nonequilibrium physics, which can provide new tools for quantum computation, quantum state generation, and the realization of novel quantum phases [36–40]. The aim of this dissertation will be to understand the types of novel nonequilibrium many-body physics which can arise in a particular type of open quantum system: driven-dissipative systems.

The remainder of this chapter will be structured as follows. The next three sections will provide introductory discussions of several key topics which are discussed in this dissertation: driven-dissipative systems, critical behavior, and Rydberg atoms. The final section will provide an outline for the following chapters.

1.2 Driven-Dissipative Systems

Driven-dissipative systems are systems which are defined by a competition of coherent drive and incoherent dissipation [36]. As a result of these two processes,

these systems generally will exhibit nonequilibrium dynamics which cannot be easily captured by the powerful tools developed for equilibrium systems, such as thermodynamic ensembles. Instead, these systems are best understood in terms of the master equation, which takes the general form

$$\partial_t \rho = -i[H, \rho] + \mathcal{D}[\rho], \tag{1.1}$$

where ρ is the density matrix of the system [41, 42]. There are two parts to the master equation. The first term describes the evolution of the system due to the Hamiltonian H. In the absence of the second term, the master equation simply describes the familiar unitary evolution associated with quantum mechanics. The second term, then, corresponds to the effects of incoherent processes which cannot be described by H, such as dissipation, which destroy the unitary evolution of the system.

In general, there are often two important assumptions that can be made about the environment which gives rise to $\mathcal{D}$. The first is that the correlation time τ_c of the environment is much smaller than any relevant dynamics of the system, i.e. the evolution is Markovian. This was implicitly assumed in Eq. 1.1, where the evolution of ρ depends only on the current state of the system. The second is that the environment is much larger than the system, so the effect of the system on the environment itself is small. Together, these two assumptions constitute the Born-Markov approximation [41, 42]. Under this approximation, $\mathcal{D}$ takes the Lindblad form

$$\mathcal{D}[\rho] = \sum_{n,m} D_{nm} \left(d_n \rho d_m^\dagger - \frac{1}{2}\{d_m^\dagger d_n, \rho\} \right), \tag{1.2}$$

where D_{nm} is a positive semidefinite Hermitian matrix, $\{d_n\}$ defines an orthonormal basis which spans the Hilbert space of the system, and $\{A, B\} = AB + BA$ is the anticommutator [42]. In the most familiar case of dissipation, the second of these two terms corresponds to loss of population and coherence, while the first of these two terms captures the population gain due to these loss processes, thus preserving the trace $\mathrm{Tr}\rho = 1$. In driven-dissipative systems, these Lindblad terms will typically describe single site loss processes. As a simple example, let us consider dissipation at a rate γ from the excited state $|e\rangle$ to the ground state $|g\rangle$ of a two-level system. The corresponding Lindblad evolution takes the form

$$\dot{\rho} = \gamma \left(\sigma^- \rho \sigma^+ - \frac{1}{2}\{\sigma^+\sigma^-, \rho\} \right), \tag{1.3}$$

where σ^α are Pauli matrices and $\sigma^-|e\rangle = |g\rangle$. Defining $\rho_{\alpha\beta} = \langle\alpha|\rho|\beta\rangle$, the resulting master equation is

$$\dot{\rho}_{gg} = \gamma\rho_{ee}, \qquad \dot{\rho}_{ee} = -\gamma\rho_{ee}, \qquad \dot{\rho}_{eg} = -\frac{\gamma}{2}\rho_{eg}, \tag{1.4}$$

where the evolution of ρ_{gg} and the evolution of ρ_{ee}, ρ_{eg} come from the first and second terms in Eq. (1.3), respectively. From this, we see explicitly how the second term of Eq. (1.3) gives rise to population loss in the excited state as well as loss of coherence between the excited and ground states, while the first term captures the fact that the loss in the excited state population will lead to an increase in the ground state population.

In driven-dissipative systems, an important concept is the steady state, which describes the long-time behavior of the system. In terms of the master equation,

the steady state is defined by

$$\dot{\rho} = 0. \tag{1.5}$$

In the simple case of dissipation discussed above, the steady state is simply $\rho_{ss} = |g\rangle\langle g|$, i.e. the system is in its ground state at long times. Naturally, such states are not particularly interesting, nor is the relaxation to the steady state. This is where the importance of the coherent drive becomes evident. By including both a coherent drive and dissipation, the long-time behavior of the system can not be understood in terms of familiar unitary dynamics or the "ground state" of some dissipative process. Instead, it must be understood in terms of a competition between these two distinct forms of dynamics, giving rise to the possibility of long-time dynamics that cannot be understood in terms of equilibrium or unitary processes. For example, consider introducing a resonant drive via the Hamiltonian,

$$H = \Omega\sigma^x, \tag{1.6}$$

where Ω is the Rabi frequency describing the drive strength. Then the resulting steady state of the system is

$$\rho_{ss} = \frac{1}{\gamma^2/4 + 2\Omega^2} \begin{pmatrix} \gamma^2/4 + \Omega^2 & -i\Omega\gamma/2 \\ i\Omega\gamma/2 & \Omega^2 \end{pmatrix}. \tag{1.7}$$

Even in this simple example of a driven-dissipative two-level system, we can see immediately that the steady state is not governed according to a Boltzmann distribution $\rho \propto e^{-H/T}$ for some temperature T, as the off-diagonal elements are complex. Thus once we move to an interacting many-body context, new forms of nonequilibrium physics may emerge that behave qualitatively different from the familiar

context of equilibrium systems.

1.3 Critical Phenomena

An emergent notion in many-body systems is macroscopic phases of matter [43,44]. Although the microscopic behaviors of a many-body system can in principle be endlessly complex, they tend to arrange themselves in such a way that different parts of the system exhibit nearly identical macroscopic properties. Additionally, as the parameters of a given system are modified, although certain quantitative properties of the system tend to undergo changes, the qualitative features of the system nevertheless remain unchanged, and it is these qualitative features that define the phase of the system. The most familiar examples of phases are those of water, particularly water vapor, liquid water, and ice. Although water vapor and liquid water are both fluids, ice possesses a crystalline structure and is thus qualitatively different from either fluid. However, as the temperature of liquid water is reduced, it freezes and becomes ice; gradual quantitative changes lead to a sudden qualitative change. This change from one phase to another describes a phase transition.

There are in general two ways such a phase transition may occur. The first is a first-order or discontinuous phase transition. In this case, at the phase transition both phases coexist, although they continue to behave qualitatively differently. As the phase transition is crossed, the system discontinuously changes between these two phases, resulting in discontinuities in the thermodynamic properties of the system. The liquid-gas phase transition is one such example, where the density discon-

tinuously changes as the phase transition is crossed. In contrast, the second type of phase transition is a second-order or continuous phase transition. In this case, the two phases are identical at the phase transition, and one continuously changes to the other. This too can occur in the liquid-gas transition, although only at the critical point where the first-order phase transition line terminates. Another well-known example is the Curie point of ferromagnets, where the material continuously develops a nonzero magnetization as the temperature is decreased.

Near a continuous phase transition, the system undergoes a change in which the behaviors of all parts of the system collectively change together. Since the same changes are happening at macroscopic length scales, phase transitions are in general a highly-correlated process. Away from the phase transition, correlations typically fall off exponentially via

$$C(\mathbf{x}_1, \mathbf{x}_2) \equiv \langle \phi(\mathbf{x}_1)\phi(\boldsymbol{x}_2)\rangle - \langle \phi(\boldsymbol{x}_1)\rangle\langle \phi(\boldsymbol{x}_2)\rangle \propto e^{-|\boldsymbol{x}_1-\boldsymbol{x}_2|/\xi}, \tag{1.8}$$

where ϕ is the order parameter which captures the ordering of the system, $\boldsymbol{x}_i$ are position coordinates, and ξ is the correlation length. The correlation length describes the scale over which fluctuations in the system are highly correlated. When two parts of the system are at distances larger than ξ, their fluctuations are effectively independent of one another. Generally, this correlation length is small and on the order of the inter-particle spacing of the system. However, at the critical point where the entire system undergoes a macroscopic, continuous change, the correlation length ξ diverges. In the case of the first-order phase transitions, ξ typically remains finite.

One of the key features of the divergent correlation length in a continuous

(a) (b)

Figure 1.1: Illustration of block-spin renormalization procedure using 3×3 blocks where white (black) denotes the spin is $+1$ (-1). (a) Majority of spins are white, leading to an effective white spin. (b) Majority of spins are black, leading to an effective black spin.

phase transition is that microscopic details of the system become less and less important as the critical point is approached. This is because for distances smaller than the correlation length, everything is highly correlated, so microscopic differences on these length scales are less important from the perspective of macroscopic length scales. A physically intuitive way to understand this is provided by Kadanoff's block-spin renormalization group [45]. In this approach, one considers separating the system into "blocks" of nearby spins which are described by the average properties of their constituents, washing out the microscopic variations (see Fig. 1.1). Such a process can be iterated, allowing microscopic variations to be increasingly ignored at larger and larger length scales. As long as these length scales are smaller than the correlation length, the system will continue to look qualitatively the same. Physically, this process is analogous to "zooming out" to look at the behavior of the system at larger length scales. Once these length scales are on the order of the system size, only macroscopic properties remain, such as the average spin of the system.

As an example, let us consider the classical Ising model on a square lattice,

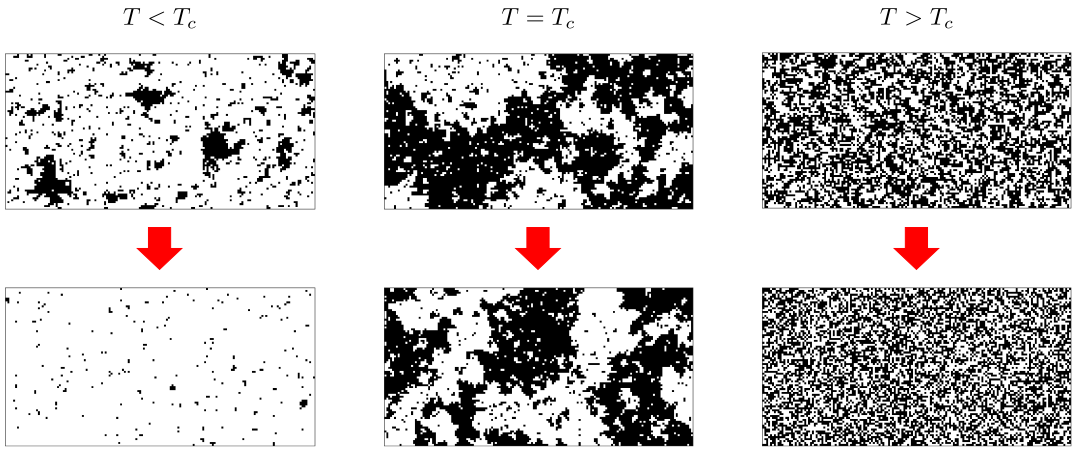

Figure 1.2: Block-spin renormalization of Ising model. The top figures illustrate a typical system state prior to renormalization. The bottom figures illustrate the system state after applying block-spin renormalization using 9×9 blocks and rescaling each new large block to the original block size. (a) In the ferromagnetic phase, the renormalization procedure leads to a more paramagnetic state. (b) At the critical point, the renormalization procedure leads to a similar state with large correlations. (c) In the disordered paramagnetic phase, the renormalization procedure leads to a more disordered state.

whose Hamiltonian is

$$H = -J \sum_{\langle ij \rangle} \sigma_i \sigma_j, \tag{1.9}$$

where J is the nearest-neighbor interaction strength, $\sigma_i \in \{-1, 1\}$ is a classical spin at site i, and $\langle ij \rangle$ indicate that i and j are nearest neighbors [46]. At large temperatures $T \gg J$, the system is paramagnetic and the spins do not align. At small temperatures $T \ll J$, the system is ferromagnetic and the spins all align to ± 1. At a critical temperature T_c, these two phases continuously change from one to the other, corresponding to a continuous phase transition. In Fig. 1.2, we illustrate Kadanoff's block renormalization group for a typical spin configuration at three temperatures: one in the paramagnetic phase $T > T_c$, one in the ferromagnetic phase $T > T_c$, and one at the critical point $T = T_c$. After applying the renormalization

procedure with 9×9 spin blocks, we see that while certain microscopic details are lost, the system still possesses the properties associated with its phase. For $T < T_c$, the alignment of the spins becomes more apparent, while for $T > T_c$, the system looks more disordered, losing microscopic structure. However, for $T = T_c$ the system continues to exhibit highly correlated structures that possess the same statistical properties.

If we were to continue this process for much larger system sizes, this trend would continue: the ferromagnetic phase would look more ferromagnetic, the paramagnetic phase would look more paramagnetic, and the critical point would continue to display correlated structures. This behavior in which the system remains unchanged is indicative of scale invariance, i.e. the system continues to look the same no matter how much the relevant length scales are increased. Although this discussion has been very qualitative, it may be formalized more rigorously, and it is this scale invariance which is at the heart of the various renormalization group techniques that have been developed in the past century [47–52].

By examining how the system changes as the relevant length scales are increased, it is possible to ascertain various properties of the system. In the paramagnetic and ferromagnetic phases, the system "flows" under this RG procedure to a corresponding scale invariant point: a fully paramagnetic phase and a fully ferromagnetic phase. In both cases, the scale invariant point is fully uncorrelated with $\xi = 0$. This is because for any finite correlation length, this RG procedure will eventually only consider length scales larger than the initial correlation length, so these microscopic correlations are lost. The crucial exception to this case is natu-

rally the critical point itself, where the correlation length is infinite. In this case, no matter how large the length scale is, correlations will continue to play a crucial role. Thus scale invariant points of the RG flow, which we shall refer to as fixed points from here on out, correspond to phases when $\xi = 0$ and continuous phase transitions when $\xi = \infty$.

At the critical point where $\xi = \infty$, the description of the correlations in Eq. (1.8) is no longer adequate. Rather than the emergence of a constant correlation at arbitrary distances, many properties of the system can be described according to power laws because, unlike exponential decay, power laws are scale invariant. If we assume that microscopic fluctuations are completely unimportant, then these power laws can be obtained via simple dimensional analysis considerations. For example, at the phase transition of the three-dimensional version of the above classical Ising model, this would imply the correlation function takes the form

$$C(r) = \frac{1}{r} f(r/\xi), \tag{1.10}$$

for $r = |\boldsymbol{x}_1 - \boldsymbol{x}_2|$ and some dimensionless function f. However, although often a good approximation, this form is not quite correct. This is because continuous phase transitions are defined by the importance of highly-correlated fluctuations, which take place on all length scales including microscopic length scales. As a result, we cannot fully ignore the effect of these fluctuations, and the form of the correlation function is slightly modified to

$$C(r) = \frac{1}{r^{1+\eta}} f(r/\xi, a/\xi), \tag{1.11}$$

where η, known as an anomalous dimension, captures modifications to the power-

law scaling due to fluctuations and a describes the microscopic length scale. Thus the power laws describing the phase transition will be composed of contributions from both simple scaling analysis as well as corrections due to fluctuations. The set of exponents which describe these power laws are known as critical exponents [43].

In fact this power-law behavior extends into a small region around the critical point as well. While the points in this region will eventually flow to the fixed point corresponding to their phase, they also possess very large correlation lengths. Thus until the RG procedure reaches length scales comparable to ξ, the correlation length is effectively infinite and the system will be well-described by the fixed point associated with the critical point. As a result, power laws emerge which describe properties of the system as a function of the distance from the critical point. For example, the magnetization M in the ferromagnetic phase and the correlation length scale as

$$M \equiv \left\langle \frac{1}{N} \sum_i \sigma_i \right\rangle \propto (T_c - T)^{\beta}, \qquad \xi \propto |T - T_c|^{-\nu}, \tag{1.12}$$

where β and ν are the corresponding critical exponents and N is the total number of spins.

While the emergence of power-law behavior at a critical point is an interesting feature, on its own it does not appear to give deeper insight into the nature of phase transitions. For example, if instead of the isotropic Ising model in Eq. (1.9) we were to consider an anisotropic Ising model with Hamiltonian

$$H = -J_x \sum_{\langle ij \rangle_x} \sigma_i \sigma_j - J_y \sum_{\langle ij \rangle_y} \sigma_i \sigma_j, \tag{1.13}$$

where $J_x \neq J_y$ and $\langle ij \rangle_x, \langle ij \rangle_y$ indicate i, j are nearest neighbors in the x- and y-

directions respectively, then we might expect a different set of power laws associated with the corresponding phase transition. However, contrary to this expectation this is not the case. Even when some amount of anisotropy is introduced, the critical exponents governing the phase transition remain the same [53, 54]. Moreover, this equivalence of critical behavior goes well beyond connecting models with similar microscopic structure. For example, the critical point of the liquid-gas phase transition exhibits critical exponents that are *identical* to that of the Ising models above [55]. In spite of the fact that water and ferromagnets are completely different systems microscopically, they behave the same when near the critical point. Thus we see that critical points can exhibit universal properties that connect dramatically different systems.

This universality of behavior is a consequence of the fact that RG captures macroscopic features at large length scales. As a result of this, many microscopic details become unimportant, and properties which can persist at infinitely large scales, such as symmetries, will be the primary factors in determining the critical properties of the system. This universal behavior motivated the concept of universality classes, where two phase transitions are said to fall into the same universality class if they exhibit the same critical properties [56]. Thus by determining a set of critical exponents for a given phase transition, the corresponding universality class may be identified along with the critical properties that had not been determined. In contrast, if there is no universality class associated with a new set of critical exponents, this indicates the existence of a new universality class. Although a large variety of universality classes have been identified and understood in equilibrium

contexts, universality in nonequilibrium settings is less developed [57]. One of the primary goals of the work in this dissertation is to develop an understanding of universality in driven-dissipative phase transitions, which is presented in Chapter 2.

1.4 Rydberg Atoms

Rydberg atoms are atoms whose valence electron(s) has been excited to large principal quantum numbers n [58]. At these high principal numbers, the valence electron is weakly bound to the nucleus and is generally far from the nucleus and core electrons, as schematically illustrated in Fig. 1.3. As a result of this, these highly-excited states display a variety of exaggerated properties, including long lifetimes and strong, long-range interactions. In this section, we will discuss the origin of some of these properties and why they position Rydberg systems as an excellent platform for quantum computation and simulation.

Due to the fact that the valence electron is typically far from the nucleus, Rydberg atoms can be understood as hydrogen-like atoms to excellent approximation, and many of the concepts used to understand the hydrogen atom carry over to Rydberg atoms. The first important scaling behavior is in the energy levels of the Rydberg states

$$E_{nlj} = -\frac{Ry}{(n-\delta_{nlj})^2} = -\frac{Ry}{{n^*_{nlj}}^2}, \tag{1.14}$$

where l is the orbital angular momentum quantum number, j is the total angular momentum (excluding nuclear spin) quantum number, and Ry is the Rydberg constant. The δ_{nlj} term is known as the quantum defect, and it is only weakly de-

pendent on n, j. The quantum defects account for the fact that the Rydberg state is only approximately a hydrogen-like atom. For $l = 0$, these are typically no larger than 3 to 5 and quickly fall towards 0 as l is increased. Since typically $n \gg \delta_{nlj}$, in the rest of this section we will drop the subscript nlj and consider the Rydberg properties in terms of n^*. The second important scaling behavior is that of the dipole matrix elements. At large values of n^*, the radial wavefunction of the excited state is very similar to that of nearby Rydberg states, so the dipole matrix elements scale with n^* as

$$\langle n|r|n'\rangle \approx \sqrt{\langle n|r^2|n\rangle} \propto n^{*2}, \tag{1.15}$$

when $n' \approx n$. From this we see that like the atomic radius of the Rydberg state, the dipole matrix elements between nearby Rydberg states scales as n^{*2}. To put this in perspective, if the ground state radius is on the order of one Bohr radius $a_0 \approx 5.3 \times 10^{-2}$ nm, then the radius of a $n^* = 50$ Rydberg state is on the order of 130 nm, which is comparable to the lattice spacing of optical lattices. When $n \gg n'$, these dipole matrix elements decrease as

$$\langle n|r|n' \pm 1\rangle \approx n^{*-3/2}. \tag{1.16}$$

Using the scaling behavior of the energy levels and the dipole matrix elements, we may identify the resulting scaling behavior of several other important properties of Rydberg atoms. Here, we will focus on two in particular: Rydberg state lifetimes and Rydberg interactions. According to Fermi's golden rule, the rate of spontaneous emission between two states is given by

$$\Gamma_{n\to n'} = \frac{4\alpha\omega^3|\langle n|r|n'\rangle|^2}{3c^2}, \tag{1.17}$$

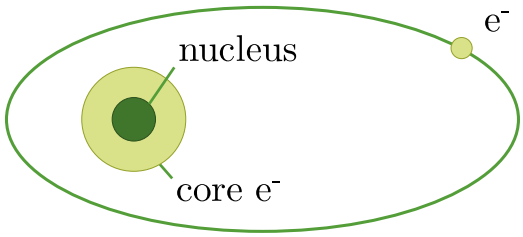

Figure 1.3: Qualitative illustration of a Rydberg atom. A single valence electron is excited to a large principal quantum number n so that it generally far away from the nucleus and core electrons.

where α is the fine structure constant, ω is the energy difference between $|n\rangle$ and $|n'\rangle$, and c is the speed of light. When $n \approx n'$, then Eq. (1.14) indicates that $\omega^3 \propto n^{*-9}$, so $\Gamma_{n\to n'} \propto n^{*-5}$. In contrast, when n' corresponds to a lowly excited state, then ω is approximately the ionization energy of the ground state and has no scale dependence. Thus in this case, $\Gamma_{n\to n'} \propto n^{*-3}$. When considering all of the different states that $|n\rangle$ can decay to, these low-lying states will dominate, and the lifetime scales as

$$\tau = \frac{1}{\sum_{n'} \Gamma_{n\to n'}} \propto n^{*3}. \tag{1.18}$$

From this, we see that for large n, these lifetimes can be quite large. For example, for an s state with $n = 50$, we find $\tau \approx .1$ ms [59].

Next, we consider interactions between different Rydberg atoms. At distances larger than the Rydberg state radius, Rydberg atoms interact via a dipole-dipole interaction

$$V_{dd} = \frac{\boldsymbol{\mu}_1 \cdot \boldsymbol{\mu}_2 - 3(\boldsymbol{\mu}_1 \cdot \hat{\boldsymbol{r}})(\boldsymbol{\mu}_2 \cdot \hat{\boldsymbol{r}})}{r^3}, \tag{1.19}$$

where $\boldsymbol{\mu}_i$ is the electric dipole moment of the ith Rydberg atom and $\boldsymbol{r}$ is the displacement vector between the two Rydberg atoms. Since the dipole matrix elements

are proportional to n^{*2}, the dipole-dipole interaction scales as

$$V_{dd} \propto \frac{n^{*4}}{r^3}. \tag{1.20}$$

In the absence of an electric field, which gives each state a permanent dipole moment, $\langle\psi\psi'|V_{dd}|\psi''\psi'''\rangle \neq 0$ only when $l = l'' \pm 1$ and $l' = l''' \pm 1$ due to parity. This means that atoms in the same state do not experience dipole-dipole interactions. Resonant dipole-dipole interactions involving two Rydberg states will be particularly important in this dissertation. These interactions take the form

$$V = \frac{C_3}{r^3}(1 - 3\cos^2\theta_{12})|\psi\psi'\rangle\langle\psi'\psi| + H.c., \tag{1.21}$$

where $C_3 = e^2|\langle\psi|r|\psi'\rangle|^2$ and θ_{12} is the angle $\boldsymbol{r}$ makes with the quantization axis. These off-diagonal "flip-flop" interactions cause the Rydberg states of the two atoms to coherently swap.

Although two atoms in the same Rydberg state do not experience dipole-dipole interactions, they experience a van der Waals (vdW) interaction through off-resonant dipole dipole interactions. According to second-order perturbation theory, two atoms in the same state experience the interaction

$$V_{vdW} = \sum_{\psi'\psi''} \frac{|\langle\psi|V_{dd}|\psi'\rangle\langle\psi|V_{dd}|\psi''\rangle|^2}{2E_\psi - E_{\psi'} - E_{\psi''}}, \tag{1.22}$$

where $|\psi''\rangle = |n''l''j''m_j''\rangle$ and E_α is the energy of state $|\alpha\rangle$. The numerator will be largest and the denominator will be smallest when $n', n'' \approx n$. Thus the numerator scales like n^{*8}/r^6 while the denominator scales like the energy level spacing of nearby states, i.e. n^{*-3}. Altogether, the vdW interactions scale like

$$V_{vdW} \propto \frac{n^{*11}}{r^6}. \tag{1.23}$$

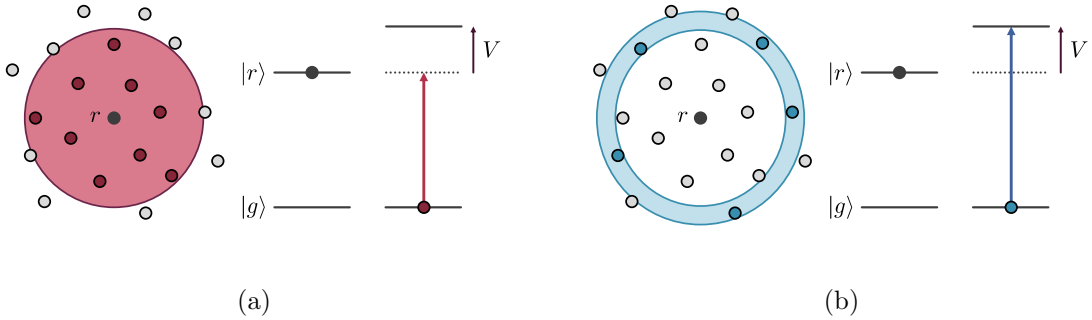

Figure 1.4: Illustration of Rydberg (a) blockade and (b) antiblockade for diagonal Rydberg interactions where $|g\rangle$ ($|r\rangle$) denotes the ground (Rydberg) state. The excitation of the Rydberg atom r shifts the effective energy level of the Rydberg state for the red (blue) atoms by an interaction strength V, preventing resonant (facilitating off-resonant) excitations, leading to Rydberg blockade (antiblockade).

From this, we see that as n is increased, the vdW interactions rapidly increase, allowing for strong, long-range interactions between atoms in the same Rydberg state.

Two important concepts when studying Rydberg atoms are blockade and antiblockade (also known as facilitated resonance), which emerge when external fields are used to excite more than one atom to a Rydberg state [60–63]. In both cases, consider an external drive that couples the ground state to a Rydberg state. When the first Rydberg state is excited, it will effectively shift the energy level of the corresponding Rydberg state of the nearby Rydberg atoms by this interaction strength. Blockade occurs when the drive is resonant, and the effect of the Rydberg interaction is to make the drive effectively off-resonant, blockading the subsequent excitations of Rydberg atoms (see Fig. 1.4a). In contrast, antiblockade occurs when the drive is off-resonant. In this case, when the Rydberg interaction is properly chosen, it can make the drive effectively resonant, thus facilitating the excitation of a subsequent

Rydberg atom (see Fig. 1.4b). In the case of diagonal vdW interactions, the resulting interaction shifts will add together. However, for off-diagonal dipole-dipole interactions, the effect of multiple interactions is more complicated. Chapter 3 will discuss how for off-diagonal dipole-dipole interactions, a complex interplay of both blockade and antiblockade processes can emerge.

1.5 Outline of Dissertation

In Chapter 2, we consider more generally the behavior of multicritical points in driven-dissipative systems where two order parameters describe the system's critical behavior. We show that near such a multicritical point, new nonequilibrium criticality can emerge. In particular, using dynamical perturbative RG, we show that in addition to several well-known equilibrium universality classes, a new *nonequilibrium* universality class emerges. We study this new universality class and identify several novel behaviors that are not typically possible in conventional equilibrium systems.

In Chapter 3, we consider an example of an experimentally-motivated driven-dissipative many-body Rydberg system. In particular, we consider how blackbody radiation from the driven Rydberg s state to nearby (in n) p states induces strong, long-range dipole-dipole interactions. These interactions give rise to a complex interplay of blockade and antiblockade effects, leading to reduced populations for resonant drive and strongly enhanced populations for far detuned drive. We study this problem theoretically using two different approaches and compare their performance

against experimental results in Ref. [64].

Chapter 2: Nonequilibrium fixed points of coupled Ising models

2.1 Introduction

The increasing control over atomic, molecular, and optical (AMO) systems has provided new avenues into studying many-body physics that are not accessible in conventional condensed matter systems. In particular, driven-dissipative systems, defined by the competition between a coherent drive and dissipation due to the coupling to the environment, have emerged as a versatile setting to investigate nonequilibrium physics [36]. They are very naturally realized by a variety of emerging AMO quantum simulation platforms ranging from exciton-polariton fluids [65–70], to trapped ions [71, 72], to Rydberg gases [73–76], to circuit-QED platforms [12, 77]. At long times, these systems approach a nonequilibrium steady state due to the interplay of drive and dissipation. The steady states can potentially harbor novel phases and exhibit exotic dynamics. Situated far from equilibrium, understanding the properties of these steady states requires methods beyond those suitable in or near equilibrium. The quest to realize and characterize macroscopic phases of these nonequilibrium systems has sparked a flurry of theoretical and experimental investigations.

Given their nonequilibrium dynamics, driven-dissipative systems are expected

to exhibit universal, critical properties different from their equilibrium counterparts. In spite of this, it has become increasingly clear that an effective temperature, and thus an effectively classical equilibrium behavior, emerges in a large class of driven-dissipative phase transitions [78, 79]. In particular, the equilibrium Ising universality class and more generally the model A dynamics of the Hohenberg-Halperin classification—describing the critical behavior of a non-conserved order parameter in or near equilibrium—have emerged in a variety of driven-dissipative phase transitions; these include bosonic/photonic Bose-Hubbard systems [80–83], various driven-dissipative spin models near an Ising [84–90], antiferromagnetic [87–95], or limit-cycle phase [88–91], as well as driven-dissipative condensates consisting of polaritons [96, 97]. A possible exception is a two-dimensional driven-dissipative condensate, where it has been argued that the nonequilibrium Kardar-Parisi-Zhang (KPZ) universality class governs the long-wavelength dynamics [98, 99]. While existing experiments are consistent with an effective thermal behavior [100, 101], KPZ physics is expected to emerge under different experimental conditions. In general, an important goal of the field is to identify whether generic driven-dissipative systems can escape the pull of an effective equilibrium behavior and instead give rise to new nonequilibrium universality classes. In particular, it has proved difficult to identify nonequilibrium universal behavior which is genuinely of a quantum nature; see Refs. [102–104] for recent proposals to achieve nonequilibrium quantum criticality and Ref. [105] for numerical evidence of an equilibrium quantum critical point in a driven-dissipative system.

An effective equilibrium behavior is not special to driven-dissipative quantum

systems. In *driven-diffusive* classical systems too, where the drive as well as the dynamics are entirely classical, effective equilibrium seems to be remarkably robust. For instance, an Ising-type dynamics governing a non-conserved order parameter is proved to be stable against all dynamical, nonequilibrium perturbations [106]. More generally, the universal dynamics of various models in the Hohenberg-Halperin classification [56] are shown to be robust against nonequilibrium perturbations which violate detailed balance [107–116]; truly nonequilibrium behavior emerges under more constrained dynamics, for example, in the presence of a conserved order parameter in an anisotropic medium [117–121]. In much of the previous work, situations have been considered where the phase transition is governed by a single order parameter. Due to the restriction that this places on the dynamics, a description based on an effective Hamiltonian often becomes available, hence the emergence of an effective equilibrium behavior.

In this work, we consider a driven-dissipative model that gives rise to multicritical points defined by the joint transition of *two* order parameters. In particular, we investigate the interplay of two phase transitions, each of which has been studied extensively in driven-dissipative settings: One is the many-body analog to optical bistability, and in the other a sublattice symmetry is spontaneously broken, leading to an antiferromagnetic ordering. A schematic illustration of this combination is shown in Fig. 2.1. With two order parameters, the nonequilibrium dynamics is much less constrained than that of equilibrium and an immediate identification of an effective Hamiltonian is no longer possible. Remarkably, we show that a new, genuinely nonequilibrium universal behavior emerges at the multicritical point, giving rise to

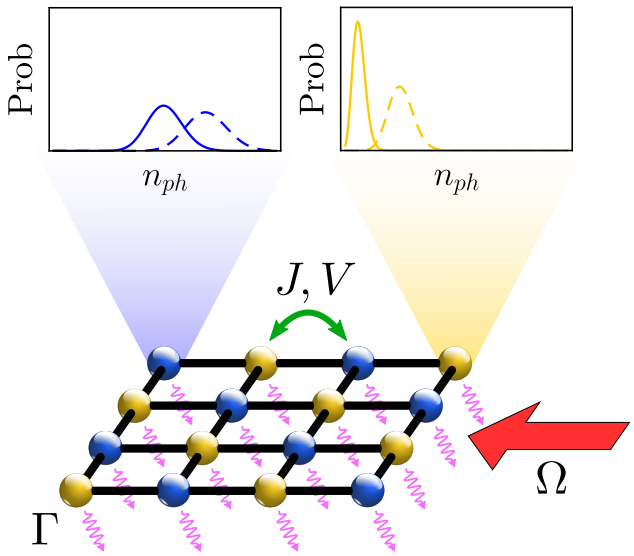

Figure 2.1: Schematic illustration of the physical setup. The contrast of the two checkerboard (light yellow and dark blue) sublattices defines the antiferromagnetic order parameter. On each sublattice, there is a low-population (low n_{ph}; solid curve) and a high-population (high n_{ph}; dashed curve) steady state, corresponding to the bistability order parameter. The large arrow indicates the drive, while the wavy arrows represent the dissipation. J and V denote the hopping and nearest-neighbor interactions, respectively.

exotic critical behavior and dynamics. Our proposal to observe nonequilibrium critical behavior relies on tuning the system parameters (such as drive and detuning, which are easy to control) to a multicritical point. In fact, the driven-dissipative setting of our model can be experimentally realized using cross-Kerr nonlineraties in cavity arrays [93, 94, 122].

In order to determine the critical behavior, we will employ the Keldysh-Schwinger and functional integral formalism suited for the nonequilibrium setting of driven-dissipative systems [82, 87, 96–99, 102, 103, 123–127]. While the presence of two order parameters prevents an immediate Hamiltonian description, the long-wavelength universal behavior—and whether or not the macroscopic behavior escapes an equilibrium fixed point (EFP)—is determined by investigating how the

parameters evolve under a dynamical version of renormalization-group (RG) techniques [128].

The remainder of this chapter is organized as follows. In Sec. 2.2, we present the main results of this chapter and a summary of the nonequilibrium critical properties emerging in our driven-dissipative model. In Sec. 2.3, we discuss the phase diagram of the model and identify the multicritical points where two distinct phase transitions meet. In Sec. 2.4, we present the RG analysis and show that a pair of new classical nonequilibrium fixed points (NEFPs) emerge that exhibit a variety of novel critical behaviors. In Sec. 2.5, we discuss an experimental setting based on cavity arrays to realize the multicritical points of our model. Finally, in Sec. 2.6, we conclude this chapter with a discussion of possible future directions which are motivated by the results of our work. In Appendix A, we present technical details omitted from the main text.

2.2 Main Results

In this section, we present the main results of this chapter. We consider a driven-dissipative model which displays two distinct phase transitions, each of which arise generically in various settings. The first one is a many-body version of bistability where two stable solutions arise with a low or high population of photons (or excitation of spins). In the thermodynamic limit, the bistable region is reduced to a line of first-order phase transitions that terminates at a critical point, reminiscent of a liquid-gas phase transition. The second type of phase transition is

one to an antiferromagnetic phase where the population takes different values on the two sublattices (a/b) of the system. We shall consider a model where these phase transitions coalesce at a multicritical point and investigate the exotic dynamics due to the interplay of the respective order parameters. These features are provided, for example, in a driven-dissipative model of weakly interacting bosons with nearest-neighbor density-density interactions on a d-dimensional cubic lattice. The coherent dynamics of the model is governed by the Hamiltonian

$$H = \sum_i -\Delta a_i^\dagger a_i + \Omega(a_i^\dagger + a_i) + \sum_{\langle ij \rangle} -J(a_i^\dagger a_j + a_j^\dagger a_i) + V a_i^\dagger a_i a_j^\dagger a_j, \tag{2.1}$$

where Δ is the detuning of the drive, Ω the drive strength, J the hopping strength, and V the strength of the nearest-neighbor interactions. The incoherent dynamics is due to loss of bosons, characterized by the Lindblad operators $L_i = \sqrt{\Gamma} a_i$, where Γ defines the loss rate. The (mixed) state of the system ρ evolves under the quantum master equation

$$\dot{\rho} = -i[H, \rho] + \sum_i L_i \rho L_i^\dagger - \frac{1}{2}\{\rho, L_i^\dagger L_i\}, \tag{2.2}$$

until it approaches a nonequilibrium steady state at long times where $\dot{\rho} = 0$. The interplay of the coherent drive (the linear term in the Hamiltonian) and dissipation together with the interactions tends to give rise to bistability, while the nearest-neighbor interactions can lead to an antiferromagnetic phase. We stress that our general results should hold beyond the specific model considered here; for example, the addition of on-site interactions or density-dependent hopping terms to our model also gives rise to multicritical points whose universal properties should be independent of the microscopic model considered. More generally, the relevant features of

our bosonic model also arise in a variety of driven-dissipative systems including spin models [82, 86, 87, 89, 91, 93, 94]. We have chosen this particular model as a minimal driven-dissipative setting that gives rise to multicritical points, although our general conclusions should apply to a large class of models.

Each phase transition in our model is characterized by an Ising-like order parameter (low/high density in bistability and sublattice a/b in the antiferromagnetic transition). The simple structure of the order parameter, together with the incoherent nature of the dynamics, puts a strong constraint on the universal properties of the phase transition. Thus, it may be expected that each phase transition alone is described by the Ising universality class that also governs the Ising-type transitions in equilibrium. It can be argued, on more formal grounds, that this is indeed the case. Associating the order parameter ϕ_1 with bistability and ϕ_2 with antiferromagnetic ordering, their long-wavelength properties in the steady state are governed by a thermal distribution but with respect to the effective (classical) Hamiltonians

$$\mathcal{H}_1 = \int_{\mathbf{x}} \frac{D_1}{2}|\nabla\phi_1|^2 - h\phi_1 + \frac{r_1}{2}\phi_1^2 + \frac{g_1}{4}\phi_1^4, \tag{2.3a}$$

$$\mathcal{H}_2 = \int_{\mathbf{x}} \frac{D_2}{2}|\nabla\phi_2|^2 + \frac{r_2}{2}\phi_2^2 + \frac{g_2}{4}\phi_2^4, \tag{2.3b}$$

with D_i characterizing the stiffness, g_i the interaction strength, r_i the distance from the critical point, and h an effective magnetic field. Note that due to sublattice symmetry, there is no magnetic field associated with the antiferromagnetic phase. Furthermore, the incoherent nature of the model leads to stochastic Langevin-type dynamics of the order parameters as [128]

$$\gamma_i \partial_t \phi_i = -\frac{\delta \mathcal{H}_i}{\delta \phi_i} + \xi_i, \tag{2.4}$$

where γ_i is a "friction" coefficient and ξ_i describes Gaussian white noise with correlations

$$\langle \xi_i(t,\mathbf{x})\xi_j(t',\mathbf{x}')\rangle = 2\gamma_i T_i \delta_{ij}\delta(t-t')\delta(\mathbf{x}-\mathbf{x}'), \tag{2.5}$$

where T_i is the effective temperature of the system. Near equilibrium, the "friction" coefficients γ_i control the rate at which the system relaxes to a thermal state via dissipating energy and thus is a purely dynamical quantity. The noise itself is related to the dissipation (i.e., friction) through temperature in what is known as the Einstein relation, which itself is a consequence of the fluctuation-dissipation theorem [128]. In the nonequilibrium context of driven-dissipative models, where there is no intrinsic temperature, the ratio of the noise level to the dissipation can be used to define an effective temperature at long wavelengths. Even a nonequilibrium system that is effectively (i.e., at large scales) governed by the Hamiltonian dynamics [as in Eq. (2.4)] is effectively in thermal equilibrium. This condition is typically satisfied for a single Ising-like order parameter [120]. Notice that, with the appropriate scaling of the fields ϕ_i, the effective temperatures can be set to $T_i = 1$. Therefore, as long as the two order parameters are not coupled, their distribution in the steady state is given by $e^{-\mathcal{H}_1-\mathcal{H}_2}$.

The situation is entirely different in the vicinity of multicritical points where the two order parameters are generally coupled. Given the underlying symmetries, the dynamics can always be brought to the form

$$\gamma_1\partial_t\phi_1 = -\frac{\delta\mathcal{H}_1}{\delta\phi_1} - g_{12}\phi_1\phi_2^2 + \xi_1, \tag{2.6a}$$

$$\gamma_2\partial_t\phi_2 = -\frac{\delta\mathcal{H}_2}{\delta\phi_2} - g_{21}\phi_2\phi_1^2 + \xi_2. \tag{2.6b}$$

Notice that the new terms that couple the two fields respect the underlying Ising symmetry of both order parameters. The noise correlations are given by Eq. (2.5); we shall again exploit our freedom in scaling the fields to set $T_1 = T_2 = 1$. With the two order parameters coupled, the condition for an effective equilibrium description becomes much more restrictive. A thermal description requires the entire dynamics to be described by a single Hamiltonian. This only occurs when $g_{12} = g_{21}$, leading to the effective Hamiltonian

$$\mathcal{H} = \mathcal{H}_1 + \mathcal{H}_2 + \frac{g_{12}}{2} \int_{\mathbf{x}} \phi_1^2 \phi_2^2, \tag{2.7}$$

in which case the steady-state distribution is given by $e^{-\mathcal{H}}$. However, this will not generally be the case, so we must consider how various parameters flow under RG. While the microscopic (though coarse-grained) dynamics is not immediately described by a thermal state, it could very well be the case that the RG flow pulls the system into a thermal fixed point where $g_{12}^* = g_{21}^*$ at macroscopic scales. Indeed, we show that this is the case roughly when the microscopic values of the coupling constants are both positive, i.e., when $g_{12},\ g_{21} > 0$. It is rather remarkable that equilibrium restores itself under RG, showcasing another instance in which equilibrium proves to be a robust fixed point even when the system is driven far from equilibrium. This is, however, not the end of the story: We show that, when the microscopic couplings have opposite sign ($g_{12} g_{21} < 0$), a pair of two NEFPs emerge where $g_{12}^* = -g_{21}^*$. (Both EFPs and NEFPs are shown in Fig. 2.2.) Furthermore, we will argue that for the model under consideration, the critical behavior will be governed by one of the NEFPs. These fixed points give rise to a new nonequilibrium

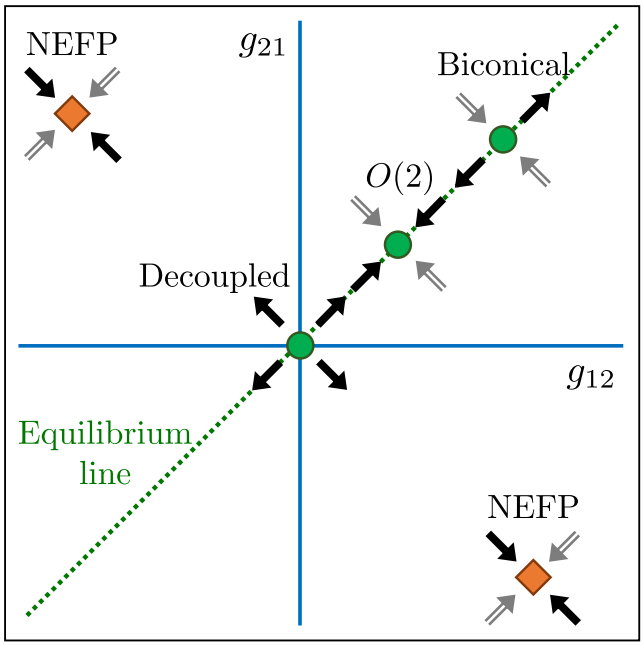

Figure 2.2: A schematic RG flow diagram projected to the g_{12}-g_{21} plane. (The full RG flow requires a 5-dimensional space; see Sec. 2.4.) In addition to the EFPs where $g_{12} = g_{21}$ (green circles), a pair of stable NEFPs (orange diamonds) emerge in the sector defined by the opposite signs of g_{12} and g_{21}. These new fixed points exhibit exotic critical behavior reflecting their truly nonequilibrium nature. Filled (black) arrows represent the stability while partial (gray) arrows indicate the expected stability of the various fixed points in different directions. Stability is known to lowest order in $\epsilon = 4 - d$ only in directions which preserve the ratio g_{12}/g_{21}. The RG flow cannot cross the g_{12}, g_{21} axes, which is represented by double lines. The stable EFP is characterized by an emergent $O(2)$ symmetry, while the unstable EFPs include a biconical fixed point as well as various decoupled fixed points (which all lie at the origin in this diagram) corresponding to combinations of Ising and Gaussian fixed points.

universality class exhibiting a variety of exotic features that generically do not, or even cannot, arise in any equilibrium setting. A summary of the most interesting features, including the critical behavior, of the new NEFPs is illustrated in Fig. 2.3. In the following subsections, we discuss these features in detail.

2.2.1 Scaling Phenomena

In the vicinity of an RG fixed point governing a phase transition, the system exhibits universal scaling behavior characterized by critical exponents, regardless of the microscopic model. The scaling behavior of the correlation and response functions at a NEFP or in its vicinity takes, respectively, the form

$$C(\mathbf{q},\omega) \equiv \mathcal{F}\langle\{a^\dagger(\mathbf{x},t), a(0,0)\}\rangle_c/2 \propto |\mathbf{q}|^{-2+\eta-z}\tilde{C}\left(\frac{\omega}{|\mathbf{q}|^z}, \frac{r}{|\mathbf{q}|^{1/\nu'}}, P\left(\frac{\log|\mathbf{q}|}{\nu''}\right)\right), \tag{2.8a}$$

$$\chi(\mathbf{q},\omega) \equiv i\mathcal{F}\Theta(t)\langle[a^\dagger(\mathbf{x},t), a(0,0)]\rangle \propto |\mathbf{q}|^{-2+\eta'}\tilde{\chi}\left(\frac{\omega}{|\mathbf{q}|^z}, \frac{r}{|\mathbf{q}|^{1/\nu'}}, P\left(\frac{\log|\mathbf{q}|}{\nu''}\right)\right), \tag{2.8b}$$

where $\mathcal{F}$ denotes the Fourier transform in both space ($\mathbf{x}$) and time (t) with $\mathbf{q}$ the momentum and ω the frequency, the curly brackets denote the anti-commutator, and the subscript c indicates the connected part of the correlation function. Here, $r = \sqrt{r_1^2 + r_2^2}$ is the distance from the multicritical point, P is a 2π periodic function, and the functions $\tilde{C}$ and $\tilde{\chi}$ are dimensionless scaling functions. While in principle the scaling behavior could be different for the two order parameters (ϕ_1 and ϕ_2), we shall argue, based on a systematic RG analysis, that a stronger notion of scaling emerges where the critical (static and dynamic) behavior and exponents characterizing the two order parameters become identical. This is why we can express either the correlation or the response function via a single scaling function (and not one for each order parameter) with the same set of exponents. The exponents η and η' define the anomalous dimensions corresponding to correlation and response functions, respectively, and z is the dynamical critical exponent characterizing the

relative scaling of time with respect to spatial coordinates. The correlation length ξ is described by the critical exponent ν' via $\xi \propto r^{-\nu'}$. Typically, it is the exponent ν, associated with the scaling behavior of r_1 and r_2, that describes the scaling of the correlation length. However, the latter exponent becomes complex-valued at the NEFPs, $\nu^{-1} = \nu'^{-1} + i\,\nu''^{-1}$, with the real part determining the scaling of correlation length and the imaginary part leading to a discrete scale invariance, as we shall discuss shortly. Altogether, there are five independent critical exponents of interest: $\nu', \nu'', \eta, \eta', z$.

Critical points are generically associated with a continuous scale invariance where the system becomes self similar upon an arbitrary rescaling of the momentum and frequency. However, due to the "log-periodic" function in the scaling functions, the correlations are self similar upon the rescaling $\mathbf{q} \to b_*\,\mathbf{q}$ and $\omega \to b_*^z\,\omega$ for a particular scaling factor

$$b_* = e^{2\pi\nu''}, \tag{2.9}$$

or any integer powers thereof. Rather than a typical continuous scale invariance, this behavior is indicative of a *discrete* scale invariance, which is reminiscent of fractals, shapes that are self similar under particular choices of scaling [129]. A schematic depiction of the correlation functions with discrete scale invariance is shown in Fig. 2.3(a). Additionally, since the origin of the discrete scale invariance is the scaling behavior of r_i that characterize the distance from the critical point, the phase boundaries themselves also exhibit a form of discrete scale invariance in r_i; see Fig. 2.4 and the discussion in the next subsection titled "Phase Diagram".

Figure 2.3: Summary of the main features of the NEFPs contrasted with effective EFPs. (a) Schematic correlation functions. A generic continuous scale invariance characteristic of criticality is reduced to a discrete scale invariance at the NEFP. (b) Effective temperatures T_i representing the two order parameters as a function of the length scale (q^{-1}). The two temperatures become identical at long length scales, but, while they approach a constant at the EFP, they diverge at large scales at the NEFPs. (c) Gap closure upon approaching the critical point. $\Gamma_{\mathcal{L}}$ denotes the Liouvillian gap with the real part describing the relaxation rate (a.k.a. the dissipative gap) and the imaginary part characterizing the "coherence gap". For the EFP, the gap can close only along the real line, indicated by the arrow. In contrast, the gap for the NEFP can take complex values and close along any path lying in the shaded region, making a maximum angle of $\pi/3$ with the real line. (d) Critical exponents to lowest non-trivial order in $\epsilon = 4-d$. The exponent ν, typically associated with the divergence of the correlation length, becomes complex-valued at the NEFPs with its imaginary part characterizing the discrete scale invariance [cf. part (a)]. η and η' are anomalous dimensions characterizing fluctuations and dissipation with $\eta \neq \eta'$ at the NEFPs indicating the violation of the fluctuation-dissipation theorem. z is the dynamical critical exponent.

Effective equilibrium	Nonequilibrium fixed points
(a) Scale invariance	
Continuous scale invariance	Discrete scale invariance
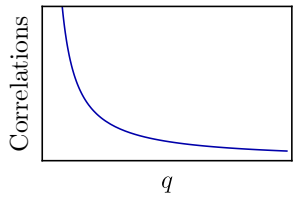	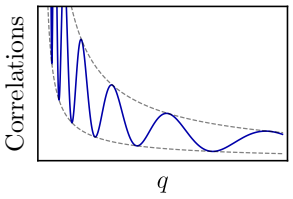
(b) Effective temperature behavior	
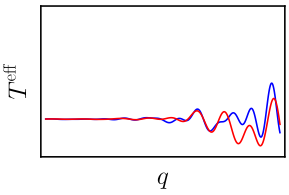	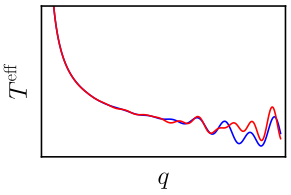
(c) Liouvillian gap closure	
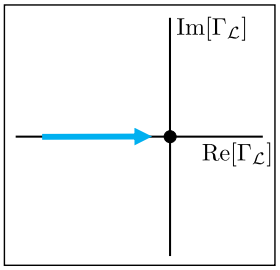	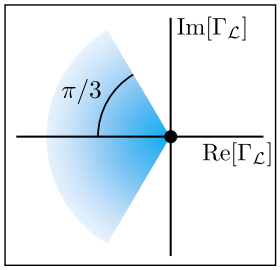
(d) Critical exponents	
$\text{Im}[\nu^{-1}] = 0$ $\eta > 0$ $\eta' = \eta$ $z - 2 = \eta'(6\log(4/3) - 1)$	$\nu^{-1} = 2 - \left(\frac{1}{2} \pm \frac{i}{2\sqrt{3}}\right)\epsilon$ $\eta = \frac{\epsilon^2}{36}(1 - 12\log(4/3)) < 0$ $\eta' = \frac{\epsilon^2}{36}$ $z - 2 = \eta'(6\log(4/3) - 1)$

The critical exponents η and η' characterize the anomalous dimensions corresponding to fluctuations and dissipation, respectively. In an equilibrium setting, the fluctuation-dissipation theorem dictates that the correlation and response functions are related as [128]

$$C(\mathbf{q},\omega) = \frac{2T}{\omega}\mathrm{Im}\chi(\mathbf{q},\omega). \tag{2.10}$$

(We have assumed the classical limit of the fluctuation-dissipation theorem at low frequencies and at a finite temperature.) In an equilibrium setting, the temperature T is just a constant set by an external bath and thus is scale invariant. Therefore, the overall scaling behavior of the correlation and response functions is identical apart from the dynamical scaling (due to ω^{-1} on the rhs of the above equation) set by the critical exponent z. This in turn puts a constraint on the critical exponents as $\eta = \eta'$ for effectively equilibrium phase transitions. However, we find $\eta \neq \eta'$ at the NEFPs, indicating the violation of the fluctuation-dissipation theorem and resulting in a new exponent characterizing the nonequilibrium nature of the fixed point. This in turn results in an effective temperature that remains scale-dependent at all scales. Inspired by the fluctuation-dissipation theorem, we define an effective "temperature" as

$$\mathrm{Env}[C(\mathbf{q},\omega)] = \frac{2T^{\mathrm{eff}}(\mathbf{q},\omega)}{\omega}\mathrm{Env}[\mathrm{Im}\left[\chi(\mathbf{q},\omega)\right]]. \tag{2.11}$$

To factor out the log-periodic nature of the correlation and response functions, we have made a convenient choice by postulating a fluctuation-dissipation relation between the envelope (Env) functions of the correlation and response functions. This relation can be defined via either the upper or lower envelope functions. We can then

identify the scaling behavior of the effective temperature at the NEFP. Interestingly, the system gets "hotter" and "hotter" at longer and longer scales, characterized by an effective temperature that scales as $T^{\text{eff}} \sim |\mathbf{q}|^{\eta-\eta'}$ at long wavelengths and fixed $\omega/|\mathbf{q}|^z$. Of course, the divergence of the effective temperature at long wavelengths does not imply an infinitely energetic state; rather, it reflects the fact that, at longer wavelengths, the correlation function is increasingly larger compared to the response function than one would expect in an equilibrium setting based on the fluctuation-dissipation theorem. This behavior is illustrated in Fig. 2.3(b) individually for the two effective temperatures corresponding to the two order parameters. At long wavelengths, these effective temperatures become identical to each other and to $T^{\text{eff}}(\mathbf{q}, \omega)$ defined above. Finally, the values of the critical exponents at the NEFPs are provided to the lowest non-trivial order in $\epsilon = 4 - d$ in Fig. 2.3(d).

2.2.2 Phase Diagram

The critical point described by the new fixed points is a tetracritical point, illustrated in Fig. 2.4. In the vicinity of the tetracritical point (with $h = 0$), there are four different phases where none, one, or both order parameters undergo a continuous phase transition. A particularly exotic feature of the phase diagram is that it exhibits spiraling phase boundaries. This leads to the discrete scale invariance of the phase diagram itself, a property that follows from the same feature of the scaling functions in Eq. (2.8). In contrast, depending on the microscopic model, the EFPs can give rise to either a bicritical point—in which case there will not be

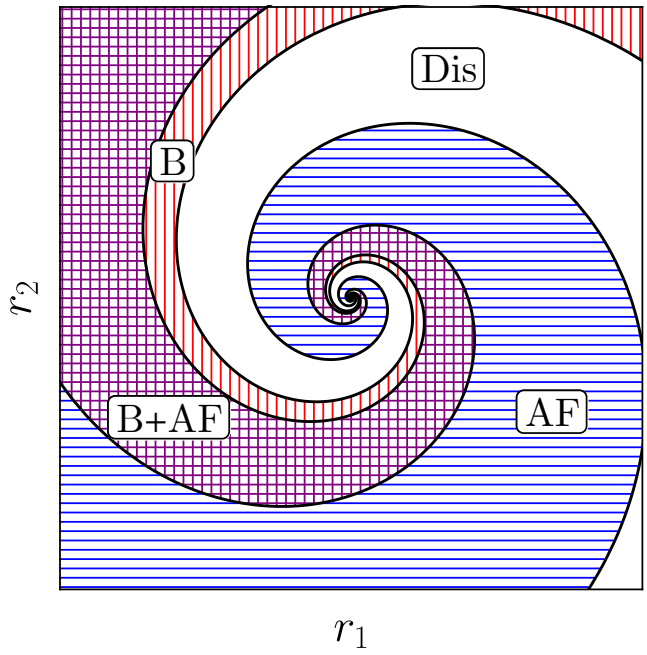

Figure 2.4: Phase diagram associated with the NEFPs of the nonequilibrium Ising model of two coupled fields for $h = 0$. The white region indicates the disordered phase, B (red vertical shading) corresponds to the phase where the bistability order parameter undergoes spontaneous symmetry breaking, AF (blue horizontal shading) denotes antiferromagnetic ordering, and B+AF (purple square shading) corresponds to the phase where both order parameters are nonzero. The solid black lines denote second-order phase transitions. The NEFP phase diagram exhibits logarithmic spirals in the phase boundaries. The other NEFP is described by an analogous diagram upon switching the roles of the two order parameters (B $\leftrightarrow$ AF, $r_1 \leftrightarrow r_2$).

a phase where both order parameters undergo a continuous phase transition—or a tetracritical point; neither of these will exhibit spiraling phase boundaries. Note that since the $\mathbb{Z}_2$ symmetry associated with the bistability transition ($\phi_1 \to -\phi_1$) is only an emergent one (when $h = 0$), the full phase diagram (including $h \neq 0$) can be better described as a three-dimensional plot that also includes the first-order phase transitions characteristic of bistability; see Fig. 2.7. The contrast between the EFPs and NEFPs can further provide a route to experimentally identify the new fixed points. An overview of the properties of bicritical and tetracritical points in equilibrium systems can be found in Refs. [130–136].

2.2.3 Spectral Properties

The NEFP can be further distinguished by its particular dynamics that governs the relaxation of the system to the steady state. In the nonequilibrium setting of our model, the dynamics is described by the Liouvillian $\mathcal{L}$ via [cf. Eq. (2.2)]

$$\partial_t \rho = \mathcal{L}[\rho], \tag{2.12}$$

rather than a Hamiltonian. However, in analogy with the ground state that is described by the smallest eigenvalue of the Hamiltonian, the steady state(s) is given by the 0 eigenvalue(s) of the Liouvillian; all the other eigenvalues of the Liouvillian have a negative real part characterizing the decay into the steady state. Furthermore, the spectral gap of the Hamiltonian is naturally generalized to the eigenvalue of the Liouvillian with the smallest (in magnitude) nonzero real part. We denote this eigenvalue by $\Gamma_{\mathcal{L}}$. For a continuous phase transition, just like the spectral gap,

the closing of the Liouvillian gap results in the divergence of a time scale associated with a slow or soft mode of the dynamics. The fashion that the latter gap closes reveals characteristic information about the nature of the phase transition. In equilibrium phase transitions at finite temperature, this gap becomes real (i.e., purely dissipative) as the critical point is approached. Even when the microscopic dynamics is far from equilibrium, the Liouvillian gap may (and typically does) become real, leading to effectively thermal equilibrium. In contrast, the dynamics near the NEFPs can close away from the real axis. This indeed occurs in the doubly-ordered phase; let $M_i = \langle \phi_i \rangle \neq 0$ define the nonzero order parameters there and redefine the fields as $\phi_i \to \phi_i + M_i$. We then find the linearized equations of motion as

$$\gamma_1 \partial_t \phi_1 = -2g_1 M_1^2 \phi_1 - 2g_{12} M_1 M_2 \phi_2, \tag{2.13a}$$

$$\gamma_2 \partial_t \phi_2 = -2g_2 M_2^2 \phi_2 - 2g_{21} M_1 M_2 \phi_1, \tag{2.13b}$$

where, at the NEFPs, $g_{12}^* = -g_{21}^*$ and $g_1^* = g_2^*$ while we can choose $\gamma_1^*/\gamma_2^* = 1$; noise, gradient, and higher-order terms have been dropped. Due to the opposite signs of g_{12} and g_{21} in the two equations, we find a spiral relaxation to the steady state. This in turn is characterized by a complex Liouvillian gap—defined by a conjugate pair of complex eigenvalues—which exhibits both a dissipative (real) and a "coherent" (imaginary) part depending on the values of M_1 and M_2. We find that when $|M_1| = |M_2|$, the angle of this complex gap relative to the real line achieves its maximum value of $\pi/3$. This is illustrated in Fig. 2.3(c). The corresponding mean-field relaxational dynamics is illustrated in Fig. 2.5.

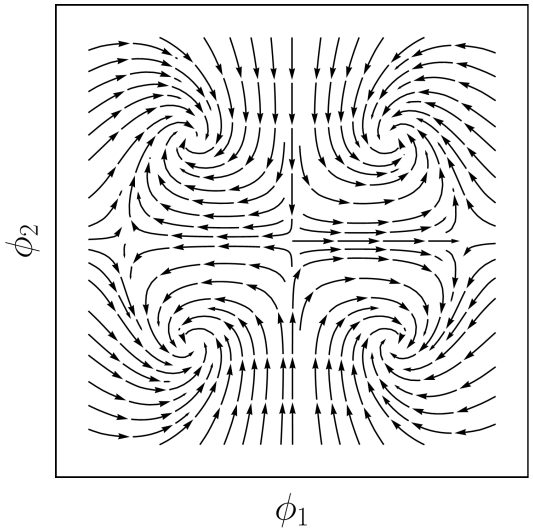

Figure 2.5: Mean field dynamics near the NEFP within the doubly ordered phase with $|M_1| = |M_2|$. The arrows denote how the fields ϕ_i evolve in time, with four possible steady states. At each steady state, there is a dissipative relaxation process as well as a "coherent" rotation, resulting in a spiraling relaxation to the steady state. Two of the steady states spiral clockwise while two spiral counter-clockwise.

2.3 Model

The representative model we have focused on is a driven-dissipative system of weakly interacting bosons defined in Eqs. (2.1,2.2). In order to understand how this model gives rise to bistability and antiferromagnetic ordering, we begin this section with a detailed discussion of mean field theory and corrections, or fluctuations, on top of the mean field solutions. Along the way, we will identify the soft modes of the dynamics that ultimately describe the critical behavior of the multicritical point. Finally, we conclude this section by presenting a mapping of our nonequilibrium model to a model of coupled Ising-like order parameters with a $\mathbb{Z}_2 \times \mathbb{Z}_2$ symmetry, corresponding to the sublattice symmetry as well as the emergent Ising symmetry due to bistability.

2.3.1 Mean Field Theory

In order to analyze the phase diagram of our model, we begin with a mean-field analysis, in which we assume different sites are uncorrelated; that is, for any two operators A_i and B_j on neighboring sites, we have $\langle A_i B_j \rangle = \langle A_i \rangle \langle B_j \rangle$ [137, 138]. Additionally, we assume that individual sites are described by coherent states. While the latter assumption follows from the former in our model, this will generally not be the case, for example, when on-site Hubbard interactions are present. However, a systematic path-integral formalism (adopted in subsequent sections) beyond mean field theory is perfectly suited to analyzing the latter type of interaction. Finally, in anticipation of the antiferromagnetic phase transition, we separate the system into two sublattices a/b and assume each to be described by a single coherent state.

Following these assumptions and using the fact that $\partial_t \langle O \rangle = Tr(\dot{\rho} O)$ for an arbitrary operator O, the resulting mean field equations of motion are given by

$$i\dot{\psi}_{\mathrm{a}} = (-\Delta - i\Gamma/2)\psi_{\mathrm{a}} - \mathfrak{z} J \psi_{\mathrm{b}} + \mathfrak{z} V |\psi_{\mathrm{b}}|^2 \psi_{\mathrm{a}} + \Omega, \tag{2.14a}$$

$$i\dot{\psi}_{\mathrm{b}} = (-\Delta - i\Gamma/2)\psi_{\mathrm{b}} - \mathfrak{z} J \psi_{\mathrm{a}} + \mathfrak{z} V |\psi_{\mathrm{a}}|^2 \psi_{\mathrm{b}} + \Omega, \tag{2.14b}$$

where ψ_i corresponds to the coherent state $\langle a \rangle$ on sublattice $i \in \{\mathrm{a}, \mathrm{b}\}$ and $\mathfrak{z}$ is the coordination number; from here on, we absorb $\mathfrak{z}$ in the microscopic parameters via $\mathfrak{z} J \to J$ and $\mathfrak{z} V \to V$. It is clear from these equations that the density-density interaction behaves as an effective detuning that depends on the density of the other sublattice. This results in a similar physics as Rydberg excitations in stationary atoms, in which case the presence or absence of a Rydberg excitation on one site

can either prevent (blockade) [60, 139, 140] or facilitate (anti-blockade) [141, 142] a Rydberg excitation on a neighboring site by shifting it away or towards the effective resonance.

Setting $\psi_{\mathrm{a}} = \psi_{\mathrm{b}}$, one can immediately see that the mean-field equations become identical to those describing bistability; cf. Ref. [82] where the nonlinearity due to the Hubbard interaction should be replaced by the density-density interactions in this context. The emergence of bistability can be understood in simple terms: Away from resonance, there is a low population on each site. However, once a sufficient number of sites are highly excited, they begin to facilitate the excitation of neighboring sites, resulting in a high-population steady state. This process occurs when the shift in detuning due to interactions is comparable to the detuning. This condition is satisfied approximately when $\frac{\Omega^2}{\Gamma^2/4+(\Delta+J)^2}V \approx \Delta + J$, where J behaves like an effective detuning while the product of the interaction strength V and the non-interacting steady-state population $[\Omega^2/(\Gamma^2/4+(\Delta+J)^2)]$ gives the interaction-induced shift of the detuning. For $\Gamma \gtrsim \Delta + J$, this reasoning becomes blurred as the drive is effectively always on resonance due to the larger linewidth. As a result, a finite region of bistability emerges with low- and high-population steady states. Beyond mean field theory, the bistable region is replaced by a line of first-order phase transitions that terminates at a critical point.

The presence of antiferromagnetic ordering in this system can be understood by inspecting the role of the density-density interactions. Since the interaction affects neighboring sites only, the blockade effects occur between sublattices but not within each sublattice. For example, if one sublattice has a high population,

it can prevent further excitations in the other sublattice. Similar to the case of bistability, the phase boundary occurs approximately when the shift in detuning due to interactions takes the system out of resonance. This approximately occurs when $|\frac{\Omega^2}{\Gamma^2/4+(\Delta+J)^2}V - \Delta - J| \gtrsim \Gamma$, i.e., when one sublattice is effectively more than a linewidth out of resonance due to interactions. Unlike bistability, this process does not break down as Γ and Ω are increased. As the decay Γ is increased, the drive strength Ω can be further increased so that the interaction-induced shift in the detuning compensates for the increase of the linewidth.

In order to better understand the mean-field structure of the model, it is convenient to introduce a new set of fields corresponding to the two order parameters as

$$\psi_B = \frac{\psi_\mathrm{a} + \psi_\mathrm{b}}{2}, \tag{2.15a}$$

$$\psi_{AF} = \frac{\psi_\mathrm{a} - \psi_\mathrm{b}}{2}. \tag{2.15b}$$

The field ψ_B captures the effects of bistability while ψ_{AF} describes the antiferromagnetic ordering. The mean-field equations can be in turn cast in terms of these fields as

$$i\dot{\psi}_B = (-\Delta - J - i\Gamma/2)\psi_B + V(\psi_B^2 - \psi_{AF}^2)\psi_B^* + \Omega, \tag{2.16a}$$

$$i\dot{\psi}_{AF} = (-\Delta + J - i\Gamma/2)\psi_{AF} + V(\psi_{AF}^2 - \psi_B^2)\psi_{AF}^*. \tag{2.16b}$$

At the multicritical point, $\psi_{AF} = 0$ and the equation governing the steady-state value of ψ_B is no different than if we had not considered antiferromagnetic ordering. Thus, the critical values of $\Delta + J$, V, Ω as well as the steady-state value of ψ_B are determined according to the critical point associated with bistability only. This

leaves a single free parameter in the equation of motion for ψ_{AF}: $\Delta - J$. By properly tuning the latter parameter, the antiferromagnetic phase boundary can be manipulated so that it intersects the critical point associated with bistability. Working in units of $\Delta + J = 1$, two multicritical points occur at

$$\begin{gathered}(\Delta_c, J_c) = \left(\frac{1}{3}, \frac{2}{3}\right) \quad \text{or} \quad \left(\frac{2}{3}, \frac{1}{3}\right), \\ \text{and} \quad \Gamma_c = \sqrt{4/3}, \quad \Omega_c = (2/3)^{3/2}/\sqrt{V},\end{gathered} \tag{2.17}$$

as well as $\Psi_c = \sqrt{2/3V}e^{-i\pi/3}$ as the steady-sate value of ψ_B at the critical point (by virtue of symmetry, $\psi_{AF} = 0$ there).

The two fields $\psi_{B/AF}$ are complex-valued, thus comprising four real (scalar) fields. However, given the Ising nature of each transition, we must anticipate that two scalar fields would be sufficient to describe the critical behavior of both types of ordering. Indeed, we find that, at the multicritical point, two massless fields emerge—defined by appropriate components of the original fields—corresponding to the soft (or slow) modes ϕ_i, while the other components ϕ_i' remain massive and are therefore noncritical (or fast). We then adiabatically eliminate the two noncritical modes by setting $\dot{\phi}_i' = 0$ and solving for ϕ_i' in terms of ϕ_i. Upon substituting our solutions for the massive fields into $\dot{\phi}_i$, we find an effective description in terms of the soft modes. We shall closely follow Refs. [82, 87] to identify these modes. For the bistability order parameter, we can identify

$$\psi_B = \Psi_c + e^{i\pi/3}\phi_1 + \phi_1', \tag{2.18}$$

with the real fields ϕ_1 and ϕ_1' characterizing the slow and fast modes, respectively. A similar identification has been made in Refs. [82, 87]; see also Refs. [143, 144] for

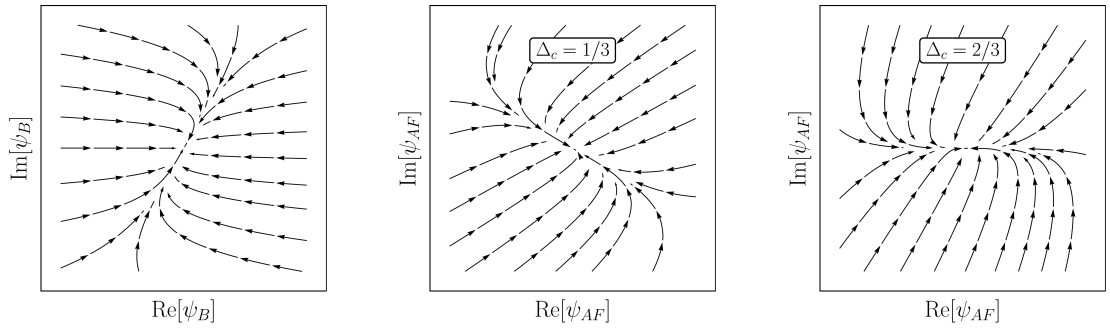

(a) (b) (c)

Figure 2.6: Dynamics of gapped (fast/massive) and soft (slow/massless) modes with arrows indicating the linear (in ϕ_i, ϕ_i') relaxation of the two modes. Near the critical point, the gapped mode quickly decays to a straight line defined by the slow direction of the soft mode. (a) Relaxation of the field ψ_B with the soft and gapped modes lying along the angles $\pi/3$ and 0, respectively. (b) Relaxation of the field ψ_{AF} for $\Delta_c = 1/3$ with the soft and gapped modes lying along the angles $-\pi/6$ and $\pi/6$ respectively. (c) Relaxation of the field ψ_{AF} for $\Delta_c = 2/3$ with the soft and gapped modes lying along the angles 0 and $\pi/3$ respectively. (We have adopted units where $\Delta + J = 1$.)

a similar reasoning, although the slow and fast modes identified there make a $\pi/2$ angle. For the antiferromagnetic field, the massless and massive components depend on the choice of the multicritical point in Eq. (2.17) as

$$\Delta_c = 1/3 : \qquad \psi_{AF} = \frac{1}{\sqrt{3}} \left(e^{-i\pi/6} \phi_2 + e^{i\pi/6} \phi_2' \right) , \tag{2.19a}$$

$$\Delta_c = 2/3 : \qquad \psi_{AF} = \frac{1}{\sqrt{3}} \left(\phi_2 + e^{i\pi/3} \phi_2' \right) . \tag{2.19b}$$

Again, the unprimed fields are massless while the primed fields are massive. The slow and fast modes of the fields are illustrated pictorially in Fig. 2.6.

Next we adiabatically eliminate the massive modes to find an effective description in terms of the soft modes. Including the gradient terms—describing the coupling between neighboring sites—as well as the noise terms due to the coupling

to the environment, we find the Langevin equations

$$\gamma_1\dot{\phi_1} = h - r_1\phi_1 + D_1\nabla^2\phi_1 + \xi_1 + A_{20}\phi_1^2 + A_{02}\phi_2^2 + A_{12}\phi_1\phi_2^2 + A_{30}\phi_1^3, \tag{2.20a}$$

$$\gamma_2\dot{\phi_2} = -r_2\phi_2 + D_2\nabla^2\phi_2 + \xi_2 + B_{11}\phi_1\phi_2 + B_{21}\phi_1^2\phi_2 + B_{03}\phi_2^3, \tag{2.20b}$$

with Gaussian noise

$$\langle \xi_i(t,\mathbf{x})\xi_j(t',\mathbf{x}')\rangle = 2\gamma_i T_i\delta_{ij}\delta(t-t')\delta(\mathbf{x}-\mathbf{x}'). \tag{2.21}$$

Higher-order terms that are irrelevant in the sense of RG have been neglected. We have expressed the noise coefficients in a convenient notation that mimics the dissipative dynamics in thermal equilibrium, in spite of the underlying nonequilibrium dynamics. Finally, the details of the adiabatic elimination together with the explicit values of all the coefficients (h, rs, Ds, As, Bs, γs and Ts) in terms of microscopic parameters of the model are provided in Appendix A.1.

It turns out that, at the level of mean field analysis, $A_{20} = 0$ in the vicinity of the multicritical point. The resulting mean-field dynamics (neglecting the gradient and noise terms) of the two soft modes is then described by a cusp-Hopf bifurcation; a detailed analysis of this type of bifurcation can be found in Ref. [145]. However, since A_{20} is not protected by any symmetries, the corresponding term can be generated in the course of RG and become of the order of the other quadratic terms. While we shall focus on the multicritical points, further details about the full mean field phase diagram of our model and slight variations on it can be found in Refs. [93,94].

2.3.2 Nonequilibrium Ising Model for Two Fields

Before proceeding with our perturbative RG analysis, it is important to identify what are known as redundant operators. These are terms in the action which are generated under suitably local symmetry-preserving transformations of the fields. Since such a transformation should not change the long-distance behavior of the system, this redundancy can be used to simplify our analysis. This is an important step for perturbative RG and to identify the upper critical dimension; see Ref. [146] for a discussion of redundant operators in an equilibrium setting.

As a simple illustrative example, consider the generic Hamiltonian of a scalar field ϕ in the absence of a $\mathbb{Z}_2$ symmetry:

$$\mathcal{H} = \int d^d\mathbf{x} \left[(\nabla\phi)^2 - h\phi + r\phi^2 + u_3\phi^3 + u\phi^4 \right]. \tag{2.22}$$

Shifting the field by a constant as $\phi \to \phi + \phi_0$, the Hamiltonian is given by the same expression (up to an unimportant additive constant) with possibly different coefficients. This underscores a redundancy in Hamiltonians that describe the same physical system. The change of the Hamiltonian $\Delta\mathcal{H}$ (or rather the integrand) due to a constant shift of the field defines a redundant operator. In particular, the cubic term transforms as

$$u_3 \to u_3 + 4u\phi_0. \tag{2.23}$$

By choosing the value of ϕ_0 properly, the ϕ^3 term can be dropped from the Hamiltonian while shifting the coefficients of the terms ϕ and ϕ^2.

Identifying redundant operators is particularly important to determine the

upper critical dimension. In the above example, the canonical scaling dimension of ϕ is given by $[\phi] = \frac{d-2}{2}$. From this, the canonical scaling of an interaction term can be determined; e.g., for a term of the form $u_n \int_{\mathbf{x}} \phi^n$ in the Hamiltonian, we have $[u_n] = d - n\frac{d-2}{2}$. An interaction term becomes marginal when the corresponding scaling dimension vanishes. Therefore, the upper critical dimension determined by the ϕ^n term is $d_c^{(n)} = \frac{n}{n/2-1}$. Had we naively started with the Hamiltonian in Eq. (2.22), the dimensional analysis would have led us to conclude that the upper critical dimension is six due to the cubic term. However, once we have taken the redundant operator into account, the latter term vanishes while the quartic term determines the upper critical dimension to be four.

Similar to the above example, we should first identify the redundant operators in the nonequilibrium setting of the two coupled scalar fields ϕ_1 and ϕ_2. In this case, we allow for a more general, nonlinear transformation which is suitably local and retains the underlying symmetries. We find that the set of redundant operators in our model is sufficient to remove all the quadratic terms in the Langevin equation (or equivalently the cubic terms in the action, similar to the Hamiltonian in the above example); the details of this analysis are presented in Appendix A.2. In particular, we find that, under this transformation, $A_{12}/B_{21} \to 2A_{02}/B_{11}$; therefore, the relative sign of the quadratic terms (prior to the transformation) determines the relative sign of the cubic terms in the final equations of motion. In the model that we have considered here, the two quadratic terms have opposite signs (see Appendix A.1). This fact will be important in determining the fixed point of the RG flow. In fact, we show that the above sign difference leads the system to one of the NEFPs.

With the above considerations, the Langevin equations can be finally brought into a canonical form as

$$\gamma_1 \partial_t \phi_1 = D_1 \nabla^2 \phi_1 + h - r_1 \phi_1 - g_1 \phi_1^3 - g_{12} \phi_1 \phi_2^2 + \xi_1, \tag{2.24a}$$

$$\gamma_2 \partial_t \phi_2 = D_2 \nabla^2 \phi_2 - r_2 \phi_2 - g_2 \phi_2^3 - g_{21} \phi_2 \phi_1^2 + \xi_2, \tag{2.24b}$$

with Gaussian noise

$$\langle \xi_i(t, \mathbf{x}) \xi_j(t', \mathbf{x}') \rangle = 2\gamma_i T_i \delta_{ij} \delta(t - t') \delta(\mathbf{x} - \mathbf{x}'). \tag{2.25}$$

Therefore, the dynamics exhibits a $\mathbb{Z}_2 \times \mathbb{Z}_2$ symmetry when $h = 0$, corresponding to the emergent symmetry $\phi_1 \to -\phi_1$ in addition to the sublattice symmetry $\phi_2 \to -\phi_2$. Such emergent symmetry has been previously identified in the bistability transition [82, 86, 87]; our analysis shows that such symmetry emerges even in the vicinity of a multicritical point where bistability and antiferromagnetic transitions coalesce. We must point out that, even in the absence of the latter symmetry, the sublattice symmetry alone prevents any mixing of the gradient and mass terms between the two fields as well as the noise terms, a property that should hold to all orders of perturbation theory.

2.4 Renormalization Group Analysis

In this section, we derive the perturbative RG equations to the two-loop order (for reasons that will be explained shortly), identify the fixed points, and characterize the critical exponents that determine the scaling properties of correlations near the multicritical point.

2.4.1 RG Equations

The Langevin-type equations can be cast in terms of the Martin-Siggia-Rose-Janssen-De Dominicis functional integral. This allows us to study our nonequilibrium model by extending the standard techniques of the RG analysis to a dynamical setting; see, for example, Ref. [128] for more details. The nonequilibrium partition function is defined by $Z = \int \mathcal{D}[\phi_i, i\tilde{\phi}_i] e^{-\mathcal{A}[\tilde{\phi}_i, \phi_i]}$ where the functional integral measure as well as the "action" $\mathcal{A}$ involve both fields ϕ_i with $i = 1, 2$ and their corresponding "response" fields $\tilde{\phi}_i$. In the language of Keldysh field theory, ϕ corresponds to the classical field while $\tilde{\phi}/2i$ corresponds to the quantum field. The statistical weight of $\phi_i(t, \mathbf{x})$ can be obtained by integrating out both response fields as $P[\phi_i] = \int \mathcal{D}[i\tilde{\phi}_i] e^{-\mathcal{A}[\tilde{\phi}_i, \phi_i]}$. While the partition function $Z = 1$ by construction, the expectation value of any quantity—the fields themselves or their correlations— can be determined by computing a weighted average in the partition function. For our model defined by Eqs. (2.24,2.25), we write the action as the sum of quadratic and nonlinear (beyond quadratic) terms as

$$\mathcal{A}[\tilde{\phi}_i, \phi_i] = \mathcal{A}_0[\tilde{\phi}_i, \phi_i] + \mathcal{A}_{int}[\tilde{\phi}_i, \phi_i], \tag{2.26a}$$

with the quadratic action given by

$$\mathcal{A}_0[\tilde{\phi}_i, \phi_i] = \int_{t,\mathbf{x}} -h\tilde{\phi}_1 + \sum_i \tilde{\phi}_i(\gamma_i \partial_t - D_i \nabla^2 + r_i)\phi_i - \gamma_i T_i \tilde{\phi}_i^2, \tag{2.26b}$$

and the nonlinear interaction terms

$$\mathcal{A}_{int}[\tilde{\phi}_i, \phi_i] = \int_{t,\mathbf{x}} g_1 \phi_1^3 \tilde{\phi}_1 + g_2 \phi_2^3 \tilde{\phi}_2 + g_{12} \phi_1 \phi_2^2 \tilde{\phi}_1 + g_{21} \phi_2 \phi_1^2 \tilde{\phi}_2. \tag{2.26c}$$

Our goal is to determine the RG flow of various parameters in the action and specifically of the coefficients g of the interaction terms.

We begin by considering the subspace defined by $g_{12}g_{21} = 0$ when either $g_{12} = 0$ or $g_{21} = 0$. This subspace is special in that it is closed under renormalization to all orders. The reason is that when $g_{12} = 0$ or $g_{21} = 0$, one of the two fields is not affected by the other at the microscopic level, a property that should hold at all scales. This can also be understood perturbatively in a diagrammatic scheme: If, say, $g_{12} = 0$ then all diagrams that could generate g_{12} involve a causality violation, hence it should remain zero to all orders. An important consequence of this fact is that the relative sign of g_{12} and g_{21} cannot change, as this would require passing through the closed subspace.

Before performing the RG analysis, we first use our freedom in rescaling the fields to cast the action in a more convenient form. In Sec. 2.2, we used this freedom to set both temperatures to unity; here, for the convenience of the RG analysis, we shall make a different choice. Note that rescaling $\phi_2 \to c\phi_2$ and $\tilde{\phi}_2 \to \tilde{\phi}_2/c$ maps $g_2 \to c^2 g_2$, $g_{12} \to c^2 g_{12}$, and $T_2 \to T_2/c^2$. Exploiting this freedom, we can set the rescaled value of g_{12} to be identical to g_{21} up to a sign. In doing so, we have effectively shifted the renormalization of g_{12}/g_{21} onto T_1/T_2, simplifying the RG analysis later. Note, however, since g_{12} is rescaled by a factor c^2, this transformation cannot change the relative sign of g_{12} and g_{21}. This is indeed consistent with the closure of the $g_{12}g_{21} = 0$ subspace discussed above. Having rescaled the fields appropriately, we

can write the action as (the quadratic action is repeated for completeness)

$$\mathcal{A}_0[\tilde{\phi}_i, \phi_i] = \int_{t,\mathbf{x}} h\tilde{\phi}_1 + \sum_i \tilde{\phi}_i(\gamma_i \partial_t - D_i\nabla^2 + r_i)\phi_i - \gamma_i T_i \tilde{\phi}_i^2, \tag{2.27a}$$

$$\mathcal{A}_{int}[\tilde{\phi}_i, \phi_i] = \int_{t,\mathbf{x}} u_1\phi_1^3\tilde{\phi}_1 + u_2\phi_2^3\tilde{\phi}_2 + u_{12}\phi_1\phi_2(\phi_2\tilde{\phi}_1 + \sigma\phi_1\tilde{\phi}_2), \tag{2.27b}$$

where $\sigma = \pm 1$ indicates the relative sign of g_{12} and g_{21} and the coefficients u_1, u_2, and u_{12} define the rescaled values of the interaction strengths (in an abuse of notation, we use the same notation for the other rescaled parameters of the model as well as the rescaled fields).

Let us first briefly consider $\sigma = 1$, in which case the action can be written in a suggestive form as

$$\mathcal{A}[\tilde{\phi}_i, \phi_i] = \int_{t,\mathbf{x}} \sum_i \tilde{\phi}_i \left(\gamma_i \partial_t \phi_i + \frac{\delta \mathcal{H}}{\delta \phi_i}\right) - \gamma_i T_i \tilde{\phi}_i^2, \tag{2.28}$$

where the function $\mathcal{H}$ is given by

$$\mathcal{H} = \int_{\mathbf{x}} \sum_{i=1,2} \left(\frac{D_i}{2}|\nabla\phi_i|^2 + \frac{r_i}{2}\phi_i^2 + \frac{u_i}{4}\phi_i^4\right) - h\phi_1 + \frac{u_{12}}{2}\phi_1^2\phi_2^2. \tag{2.29}$$

Put in this form, Eq. (2.28) bears close resemblance to an equilibrium setting where the dynamics is governed by a Hamiltonian (in this case, $\mathcal{H}$). However, with each field at a different temperature, their coupled dynamics does not generally satisfy fluctuation-dissipation relations and thus an (effective) equilibrium behavior cannot be established, at least at the microscopic level. (Note that unlike Sec. 2.2, we have already used the scaling freedom in redefining the interaction parameters which in turn fixes the ratio T_1/T_2.) One then should resort to an RG analysis to determine whether or not effective equilibrium is restored at long wavelengths, that is, if

$T_1/T_2 \to 1$ under RG. We shall see shortly that equilibrium proves to be a robust fixed point even when $T_1/T_2 \neq 1$ at the microscopic level.

In contrast, a Hamiltonian dynamics [similar to Eqs. (2.28,2.29)] is not possible when $\sigma = -1$ since a term proportional to $\phi_1^2\phi_2^2$ in the Hamiltonian leads to equations of motion that couple the two fields with the same coefficient and hence the same sign. Therefore, in this case, the dynamics cannot flow to an EFP even when $T_1 = T_2$, with the exception of a decoupled fixed point where $u_{12} = 0$ (or $g_{12} = g_{21} = 0$). Indeed we shall argue that a pair of genuinely nonequilibrium fixed points emerge in this case.

At a technical level, an RG analysis would be complicated as we need to consider diagrams up to two loops. This is because at one loop, no renormalization occurs for the temperatures (due to causality) as well as the diffusion constants and friction terms (owing to their momentum and frequency dependence). This is while the interaction terms (u_1, u_2, and u_{12}) are all renormalized already at one loop. This observation—besides aesthetic reasons—has motivated the representation adopted here; in the original description in terms of g_{12} and g_{21}, the ratio g_{12}/g_{21} would not be renormalized at one loop.

To perform the RG analysis, we first define the renormalized parameters as

$$\begin{aligned} D_{i_R} &= Z_{D_i} D_i, & r_{i_R} &= Z_{r_i} r_i \mu^{-2}, \\ u_{i_R} &= Z_{u_i} u_i A_d \mu^{-\epsilon}, & u_{12_R} &= Z_{u_{12}} u_{12} A_d \mu^{-\epsilon}, \\ \gamma_{i_R} &= Z_{\gamma_i} \gamma_i, & T_{i_R} &= Z_{T_i} T_i, \end{aligned} \tag{2.30}$$

where $A_d = \Gamma(3-d/2)/(2^{d-1}\pi^{d/2})$ is a geometrical factor, $\Gamma(x)$ is the Euler's Gamma function, μ is an arbitrary small momentum scale (compared to the lattice spacing),

and $\epsilon = 4 - d$ defines the small parameter of the epsilon expansion. The effect of renormalization is captured in the Z factors that contain the divergences according to the minimal subtraction procedure. We shall determine these factors perturbatively to the lowest non-trivial order in ϵ or loops (the details are provided in Appendix A.3). The lowest-order corrections to Z_r and Z_u occur at one loop ($\sim \epsilon$), while those of Z_γ, Z_T, Z_D appear at two loops ($\sim \epsilon^2$). These perturbative corrections, while having some similarities with their equilibrium counterparts, are more complicated due to their nonequilibrium nature.

Using the above Z factors, we determine the RG flow and beta functions via

$$\gamma_p = \mu \partial_\mu \ln(p_R/p), \tag{2.31a}$$

$$\beta_{u_a} = \mu \partial_\mu u_{a_R}, \tag{2.31b}$$

where $p \in \{r_i, \gamma_i, D_i, T_i\}$ and $u_a \in \{u_1, u_2, u_{12}\}$. These functions describe the flow of various parameters in the action under the change of the momentum scale μ. In particular, the beta functions identify the fixed points of the interaction coefficients via $\beta_{u_a} = 0$. At any such fixed point, the scaling behavior of the remaining parameters is governed by power laws whose exponents depend on γ_p. Here, we report the beta functions for the interaction parameters u_a (the details are provided in Appendix A.3):

$$\beta_{u_1} = u_{1_R}\left(-\epsilon + 9\frac{T_{1_R}}{\gamma_{1_R}^2 \tilde{D}_{1_R}^2} u_{1_R}\right) + \sigma \frac{T_{2_R}}{\gamma_{2_R}^2 \tilde{D}_{2_R}^2} u_{12_R}^2, \tag{2.32a}$$

$$\beta_{u_2} = u_{2_R}\left(-\epsilon + 9\frac{T_{2_R}}{\gamma_{2_R}^2 \tilde{D}_{2_R}^2} u_{2_R}\right) + \sigma \frac{T_{1_R}}{\gamma_{1_R}^2 \tilde{D}_{1_R}^2} u_{12_R}^2, \tag{2.32b}$$

$$\beta_{u_{12}} = u_{12_R}\left(-\epsilon + 3\frac{T_{1_R}}{\gamma_{1_R}^2\tilde{D}_{1_R}^2}u_{1_R} + 3\frac{T_{2_R}}{\gamma_{2_R}^2\tilde{D}_{2_R}^2}u_{2_R} + \frac{4}{\gamma_{1_R}\gamma_{2_R}}\frac{T_1\tilde{D}_{2_R} + \sigma T_{2_R}\tilde{D}_{1_R}}{\tilde{D}_{1_R}\tilde{D}_{2_R}(\tilde{D}_{1_R} + \tilde{D}_{2_R})}u_{12_R}\right), \quad (2.32c)$$

where we have introduced $\tilde{D}_{i_R} \equiv D_{i_R}/\gamma_{i_R}$. These equations exhibit a number of important features. First, for $u_{12_R} = 0$, we can absorb a factor of $T_{i_R}/D_{i_R}^2$ into u_{i_R}, leaving the two beta functions for u_i independent of T_i, D_i, γ_i. We thus immediately recover a pair of uncoupled equilibrium Ising phase transitions, as one should expect. Second, under equilibrium conditions where $\sigma = 1$ and $T_{1_R} = T_{2_R} \equiv T_R$, we recover the standard beta functions in equilibrium. In a similar fashion, we can absorb the factors of $T_R/D_{i_R}^2$ into u_{i_R} and $T_R/(D_{1_R}D_{2_R})$ into u_{12_R}, again leaving the beta functions dependent only on the coupling coefficients. This observation underscores the important fact that, in equilibrium, static properties are entirely decoupled from the dynamics. On the other hand, in the setting of our nonequilibrium model, statics and dynamics are inherently intertwined. Indeed, no redefinition of the coupling terms can lead to beta functions that would be independent of T_{i_R} and $\tilde{D}_{i_R}$. This is not the case for γ_{i_R} as they can always be absorbed in other parameters; for example, we can still absorb $1/\gamma_{i_R}^2$ into u_{i_R} and $1/(\gamma_{1_R}\gamma_{2_R})$ into u_{12_R} in the beta functions. This reflects the fact that, through an appropriate rescaling of the fields, one can always rescale γ_i arbitrarily without changing $T_i, \tilde{D}_i$, or the overall structure of the action.

To set up the full RG equations, let us define the parameters

$$v \equiv \frac{T_2}{T_1}, \quad w \equiv \frac{\tilde{D}_2}{\tilde{D}_1}, \quad (2.33a)$$

$$\tilde{u}_i \equiv \frac{T_i}{D_i^2} u_i, \quad \tilde{u}_{12} \equiv \frac{T_1}{D_1 D_2} u_{12}. \tag{2.33b}$$

With these definitions, the beta functions for the new interaction parameters $\tilde{u}_a$ depend only on the renormalized parameters v_R and w_R. To obtain the full RG equations, we further need to determine the RG evolution of the latter parameters. As we shall see, their RG equations are also closed in the (five) parameters defined in Eq. (2.33). To see why, first notice that there are ten marginal parameters in the original action at the upper critical dimension $(\gamma_i, D_i, T_i, g_i, g_{12/21})$ which can define the basin of attraction for the RG flow. Since all four fields and time can be rescaled relative to an overall momentum scale, this leaves a total of five parameters needed to define the fixed point. The remaining parameters (r_i, h) define relevant directions of the RG flow and thus must be tuned to their critical values. In order to determine the RG equations for the parameters v and w, we use the identity

$$\beta_{p/q} = \frac{p}{q}(\gamma_p - \gamma_q). \tag{2.34}$$

We now report the full set of beta functions of the parameters of our model (with r_i and h set to zero at the fixed point)

$$\beta_{\tilde{u}_1} = \tilde{u}_{1_R}\left[-\epsilon + 9\tilde{u}_{1_R}\right] + \sigma v_R \tilde{u}_{12_R}^2, \tag{2.35a}$$

$$\beta_{\tilde{u}_2} = \tilde{u}_{2_R}\left[-\epsilon + 9\tilde{u}_{2_R}\right] + \sigma v_R \tilde{u}_{12_R}^2, \tag{2.35b}$$

$$\beta_{\tilde{u}_{12}} = \tilde{u}_{12_R}\left[-\epsilon + 4\frac{\sigma v_R + w_R}{1 + w_R}\tilde{u}_{12_R} + 3\tilde{u}_{1_R} + 3\tilde{u}_{2_R}\right], \tag{2.35c}$$

$$\beta_v = -v_R \tilde{u}_{12_R}^2 F(w_R)[v_R - \sigma][v_R + \sigma F(w_R^{-1})/F(w_R)], \tag{2.35d}$$

$$\beta_w = -w_R\left[C\left(\tilde{u}_{1_R}^2 - \tilde{u}_{2_R}^2\right) + \tilde{u}_{12_R}^2(v_R^2 G(w_R) - G(w_R^{-1})) + 2\sigma v_R \tilde{u}_{12_R}^2 (H(w_R) - H(w_R^{-1}))\right], \tag{2.35e}$$

where we have defined $C = 9\log(4/3) - 3/2$ and the functions

$$F(w) = -\frac{2}{w}\log\left(\frac{2+2w}{2+w}\right), \tag{2.36a}$$

$$G(w) = \log\left(\frac{(1+w)^2}{w(2+w)}\right) - \frac{1}{2+3w+w^2}, \tag{2.36b}$$

$$H(w) = \frac{1}{w}\log\left(\frac{2+2w}{2+w}\right) - \frac{3w+w^2}{8+12w+4w^2}. \tag{2.36c}$$

The functions F, G, H always appear in the RG equations in pairs, with one taking w_R and the other w_R^{-1} as an argument. This is because the diagrams that contribute to the beta functions come in pairs, corresponding to one from the renormalization of the terms involving ϕ_1 only and the other from those that involve ϕ_2 only. Similarly, under the mapping $\tilde{u}_{1_R} \leftrightarrow \tilde{u}_{2_R}$, $\tilde{u}_{12_R} \to \sigma v_R \tilde{u}_{12_R}$, $v_R \to v_R^{-1}$ and $w_R \to w_R^{-1}$, the beta functions are left unchanged. This reflects the fact that we can switch the role of ϕ_1 and ϕ_2 without changing the physics. As a result, if either $\sigma = -1$ or $v_R \neq 1$ at a given fixed point, there will always be a second fixed point paired with it.

The above equations determine the full RG equations of our nonequilibrium model, but it is instructive to first consider the RG equations under equilibrium conditions where the temperatures are equal, i.e., $v_R = 1$, and $\sigma = 1$. We then immediately find that the temperature ratio does not flow, $\beta_v = 0$, hence the two temperatures remain identical at all scales. Furthermore, the temperature itself—and not just the ratio—remains scale invariant as $\gamma_T = 0$, indicating (effective) thermal equilibrium. Finally, as remarked earlier, the RG equations for the interaction terms become independent of w_R under equilibrium conditions, highlighting once again the fact that, in equilibrium, the statics is decoupled from the dynamics.

There are two distinct scenarios with respect to the beta function β_w. The first scenario is that the beta function vanishes when $\gamma_{\tilde{D}_1} = \gamma_{\tilde{D}_2}$. Since the dynamical critical exponents are related to the flow of $\tilde{D}$ as $z_i = 2 + \gamma_{\tilde{D}_i}$, we find that $z_1 = z_2$ under this scenario. This means that both fields are governed by the same dynamical critical exponent, giving rise to a "strong dynamic scaling". The second scenario occurs when $\gamma_{\tilde{D}_1} \neq \gamma_{\tilde{D}_2}$, which would lead to the fixed point $w_R = 0$ or $w_R = \infty$ depending on the sign of $\gamma_{\tilde{D}_1} - \gamma_{\tilde{D}_2}$. This behavior is then described by a "weak dynamic scaling" where the two fields exhibit different dynamical scaling properties and exponents [48, 147, 148]; see also [128]. Similarly, one can consider the beta function β_v characterizing the RG flow of the ratio of the temperatures. In this case too, there are two scenarios: Either the beta function vanishes for a fixed temperature ratio or rather, depending on the sign of $\gamma_{T_1} - \gamma_{T_2}$, the RG flow leads to either $v_R = 0$ or $v_R = \infty$, which both correspond to the $g_{12}g_{21} = 0$ subspace. However, this subspace does not appear to be amenable to perturbative RG. In this sector, we find that w flows to either 0 or ∞, indicating weak dynamic scaling where the two fields are governed by distinct dynamical universality classes. However, in both cases, the fixed point values of the coupling terms diverge, resulting in a nonperturbative regime that is not accessible within the perturbative RG analysis. This indicates that an alternative approach from our present analysis should be considered in this scenario. In this work, we shall restrict ourselves to the case where v_R and w_R are both finite and nonzero.

2.4.2 Fixed Points of RG Flow

With the RG beta functions, we can now identify the resultant fixed points. In the $\sigma = 1$ sector, the only fixed points of the RG equations are those where $w_R^* = 1$, exhibiting a strong dynamic scaling, as well as $v_R^* = 1$, indicating that the two temperatures become identical at the fixed point. Indeed, aside from the case of $u_{12_R} = 0$, the only possible fixed point value of v_R at this order is 1. This can be seen by noting that the only other root of Eq. (2.35d) is $-F(w_R^{-1})/F(w_R)$, which is always negative and thus unphysical. Similarly, noting that the beta functions for u_{1_R}, u_{2_R} are identical at this order, all coupled fixed points in this sector will satisfy $u_{1_R} = u_{2_R}$. In light of this, we immediately identify $w_R = 1$ as the only possible solution of Eq. (2.35e). Remarkably, an effective equilibrium behavior emerges in this sector despite the underlying nonequilibrium nature of the dynamics. In particular, we recover the familiar equilibrium $O(2)$ and biconical fixed points as well as various decoupled fixed points involving combinations of Gaussian and Ising fixed points. However, there are no additional NEFPs in this sector (possibly with the exception of a kind of weak dynamical scaling in the $g_{12}g_{21} = 0$ subspace). Note that the emergent equilibrium is not achieved by a simple rescaling of the terms in the action to mimic an effective Hamiltonian but is truly the result of a nontrivial two-loop RG analysis.

In the $\sigma = -1$ sector, any nontrivial fixed point is truly nonequilibrium as it cannot be described by effective Hamiltonian dynamics that defines equilibrium. Therefore, we should first determine if there exists any nontrivial fixed point in

this sector or alternatively if the RG evolution flows to a trivial (decoupled) fixed point. Interestingly enough, the former is the case; we find a pair of genuinely nonequilibrium fixed points as

$$\begin{gathered} v_R^* = 1,\ w_R^* = 1, \\ u_{1_R}^* = \frac{\epsilon}{6},\ u_{2_R}^* = \frac{\epsilon}{6},\ u_{12_R}^* = \pm\frac{\epsilon}{2\sqrt{3}}. \end{gathered} \tag{2.37}$$

These fixed points also exhibit a strong dynamic scaling since $w_R^* = 1$, so the two fields are governed by the same dynamical scaling. Furthermore, we find $v_R^* = 1$, implying that the two temperatures are equal, which might suggest an equilibrium behavior; however, the latter temperatures only characterize the strength of the noise (more precisely, $\gamma_i T_i$ defines the noise) while a true equilibrium description (and a genuine notion of temperature) requires Hamiltonian dynamics [similar to Eq. (2.28)] which is inherently impossible in this sector.

While we have identified a new pair of NEFPs, this does not guarantee that they would govern the critical behavior near the multicritical point. If these fixed points are unstable under RG, further fine tuning would be necessary to access them. Even if they are stable, depending on the initial microscopic parameters, the system could still flow to an EFP under renormalization. Nevertheless, we shall argue that the multicritical point is indeed governed by the new NEFPs.

To determine the stability of the fixed points, we need to consider the stability matrix

$$\Lambda_{ab} = \frac{\partial \beta_a}{\partial s_{b_R}}, \tag{2.38}$$

where s_b denotes the set of parameters that enter the RG beta functions. A fixed

point is stable if all of the eigenvalues of Λ are positive. Although we have determined the lowest order corrections to all five parameters, we can only determine these eigenvalues up to $\mathcal{O}(\epsilon)$. This is because in order to fully determine Λ to $\mathcal{O}(\epsilon^2)$, we need to consider the two-loop corrections to the coupling terms u and the three-loop corrections to v, w. However, when a fixed point possesses a higher symmetry than the underlying field theory, then it is possible to determine some of the $\mathcal{O}(\epsilon^2)$ eigenvalues without including higher-order corrections. This is a consequence of the fact that a symmetry-preserving perturbation will not generate a symmetry-violating term, so Λ finds a block-triangular form and the two sectors can be diagonalized separately. In the equilibrium limit of our model (in the sector $\sigma = 1$ when $v = 1$), a similar situation occurs with respect to statics and dynamics, where perturbations in the dynamics (w) cannot affect the behavior of the statics (u). This makes it possible to inspect the stability of w up to $\mathcal{O}(\epsilon^2)$ at the same order of the RG calculations. In the full nonequilibrium model, the statics is not decoupled from the dynamics, so the stability in w cannot be determined using such an approach. However, for the EFPs, equilibrium plays a role similar to a higher symmetry because equilibrium perturbations do not generate nonequilibrium terms. As a result, it is possible to determine the stability in v for the two coupled EFPs, and we find both to be stable in v. However, for all of the coupled fixed points, w remains marginal. In short, to the lowest order in our perturbative expansion, the system flows to the NEFP (EFP) in the $\sigma = -1$ ($\sigma = 1$) sector. While, in principle, non-perturbative effects or higher-order terms in ϵ could modify this behavior, this is a generic feature of perturbative RG and not specific to our model. A qualitative

sketch of the expected RG flow is illustrated in Fig. 2.2 in terms of the original g_{12}, g_{21} couplings.

Finally, we remark that in the case of the original microscopic model, A_{02} and B_{11} have opposite signs, which thus carries over to the relative sign of g_{12} and g_{21}. Thus it is plausible to expect a critical behavior governed by the NEFPs.

2.4.3 Universal Scaling Behavior

Any fixed point—equilibrium or not—exhibits critical behavior and exponents characterizing correlations and dynamics among other properties of the system. In particular, we consider the anomalous dimensions η and η' of the original and response fields, the dynamical critical exponent z, as well as the exponent ν characterizing the divergence of the correlation length as the critical point is approached. These exponents describe the scaling behavior of the correlation and response functions at or near criticality as

$$C_i(\mathbf{q}, \omega, \{r_j\}) \propto \mathbf{q}^{-2+\eta-z} \hat{C}_i \left(\frac{\omega}{|\mathbf{q}|^z}, \left\{ \frac{r_j}{|\mathbf{q}|^{1/\nu_j}} \right\} \right), \tag{2.39a}$$

$$\chi_i(\mathbf{q}, \omega, \{r_j\}) \propto \mathbf{q}^{-2+\eta'} \hat{\chi}_i \left(\frac{\omega}{|\mathbf{q}|^z}, \left\{ \frac{r_j}{|\mathbf{q}|^{1/\nu_j}} \right\} \right), \tag{2.39b}$$

where $\hat{C}_i, \hat{\chi}_i$ are general scaling (dimensionless) functions. We have dropped the subscript i from η, η', z due to the strong dynamic scaling and in anticipation of the same spatial scaling dimensions for the two fields; however, we have kept the subscript in r_j for $j = 1, 2$ since the RG equations couple them in a nontrivial way.

The exponents at the fixed point can be extracted via what is known as the method of characteristics (see Appendix A.4 for details). Noting that, for fixed bare

(microscopic) parameters, the correlation and response functions are not affected by changing the RG momentum scale μ, we can relate these critical exponents to the flow functions as

$$\eta = \gamma_T - \gamma_D, \quad \eta' = -\gamma_D, \quad z = 2 + \gamma_D - \gamma_\gamma. \tag{2.40}$$

The renormalization of the parameters r_j and the corresponding exponent ν_j requires a special treatment and will be discussed later in this section. At the nonequilibrium critical point, we find [cf. Eqs. (2.31a,2.37) together with the Z factors in Appendix A.3]

$$\gamma_\gamma = -\frac{\epsilon^2}{6}\log(4/3), \quad \gamma_D = -\frac{\epsilon^2}{36}, \quad \gamma_T = -\frac{\epsilon^2}{3}\log(4/3). \tag{2.41}$$

Interestingly, we see that in contrast to an EFP where the temperature becomes scale-invariant, the effective temperature at the NEFPs changes with the scale. In particular, the system becomes "hotter" at longer length scales since $\gamma_T < 0$. Using Eq. (2.40), the critical exponents at the NEFPs are given by

$$\eta = \frac{\epsilon^2}{36}\left(1 - 12\log\left(4/3\right)\right), \tag{2.42a}$$

$$\eta' = \frac{\epsilon^2}{36}, \tag{2.42b}$$

$$z = 2 + \eta'\left(6\log\left(4/3\right) - 1\right). \tag{2.42c}$$

While, in equilibrium, $\eta = \eta'$ as a consequence of the fluctuation-dissipation theorem, we have $\eta \neq \eta'$ since the temperature itself is scale dependent, $\gamma_T \neq 0$, at the NEFP. Note also that the critical exponents z, η, η' are the same for both fields. While strong dynamic scaling already guarantees the same dynamical critical exponent, the anomalous dimensions are also identical owing to the emergent symmetry

of the fixed point where $u_{1_R} = u_{2_R}$ and $v_R = w_R = 1$. However, the latter do not reflect any actual symmetry of the model and could be modified at higher orders in the epsilon expansion.

An interesting feature of the NEFPs is that $\eta < 0$ to the first nontrivial order in the epsilon expansion. This is in contrast with equilibrium where $\eta > 0$, a fact that can be even proved on general grounds (e.g., unitarity in a related quantum field theory) [149]. If this feature ($\eta < 0$) extends beyond perturbation theory to, say, two dimensions, it would indicate that the correlation function ($C(\mathbf{r}) \propto |\mathbf{r}|^{-d+2-\eta}$) diverges at large distances. This would, however, invalidate the starting point of our field-theoretical treatment based on an expansion in field powers since large-scale fluctuations grow without bound. However, it might also indicate the absence of ordering in low dimensions. This possibility seems particularly natural in light of the effective temperature increasing at larger scales, which in turn tends to disallow ordering in low dimensions. While this may be an artifact of perturbative RG, it indicates that the behavior of the NEFPs in low dimensions is governed by different principles than their equilibrium counterparts. Finally, we note that, to the lowest nontrivial order considered, the dynamical critical exponent z is related to η' in an identical fashion as in equilibrium.

Next we consider the renormalization of the mass terms. This requires special care as their renormalization is intertwined. Similar to our redefinition of u, we should instead consider the renormalization of r_i/D_i so that we only need to consider two flow equations, which is consistent with the scaling analysis in Appendix A.4. In a slight abuse of notation, we simply replace $r_i \to D_i r_i$. Defining

$\tilde{\mu}(l) = \mu l$ and the flowing parameters $\tilde{r}_i(l)$ with $\tilde{r}_i(1) = r_{i_R}$, we find the flow equations [cf. Eqs. (2.31a,2.37) together with the Z factors in Appendix A.3]

$$l\frac{d\tilde{r}_1(l)}{dl} = \gamma_{r_1}\tilde{r}_1 = \left(-2+\frac{\epsilon}{2}\right)\tilde{r}_1(l) \pm \frac{\epsilon}{2\sqrt{3}}\tilde{r}_2(l), \tag{2.43a}$$

$$l\frac{d\tilde{r}_2(l)}{dl} = \gamma_{r_2}\tilde{r}_2 = \left(-2+\frac{\epsilon}{2}\right)\tilde{r}_2(l) \mp \frac{\epsilon}{2\sqrt{3}}\tilde{r}_1(l), \tag{2.43b}$$

where the $\pm$ refer to the two NEFPs with opposite signs of $\tilde{u}_{12_R}$. The flow equations can be solved as

$$\tilde{r}_1(l) = l^{-1/\nu'}\left[r_{1_R}\cos\frac{\log l}{\nu''} + r_{2_R}\sin\frac{\log l}{\nu''}\right], \tag{2.44a}$$

$$\tilde{r}_2(l) = l^{-1/\nu'}\left[r_{2_R}\cos\frac{\log l}{\nu''} - r_{1_R}\sin\frac{\log l}{\nu''}\right], \tag{2.44b}$$

where

$$\nu'^{-1} = 2-\frac{\epsilon}{2}, \quad \nu''^{-1} = \pm\frac{\epsilon}{2\sqrt{3}}. \tag{2.45}$$

These equations can be cast in a more compact notation as

$$\tilde{r}_1(l) + i\tilde{r}_2(l) = l^{-1/\nu'-i/\nu''}(r_{1_R} + ir_{2_R}). \tag{2.46}$$

Defining $r \equiv r_1 + ir_2$, we can recast this equation as $\tilde{r}(l) = l^{-1/\nu}r_R$ where the critical exponent ν emerges as

$$\nu^{-1} = \nu'^{-1} + i\,\nu''^{-1} = 2 - \left(\frac{1}{2} \pm \frac{i}{2\sqrt{3}}\right)\epsilon. \tag{2.47}$$

Interestingly, the exponent ν becomes complex-valued at the NEFP. We can then express the scaling functions in Eq. (2.39) as

$$\hat{C}_i = \tilde{C}_i\left(\frac{\omega}{|\mathbf{q}|^z}, \frac{|r_R|}{|\mathbf{q}|^{1/\nu'}}, P\Big(\frac{\log|\mathbf{q}|}{\nu''} - \angle r_R\Big)\right), \tag{2.48a}$$

$$\hat{\chi}_i = \tilde{\chi}_i \left(\frac{\omega}{|\mathbf{q}|^z}, \frac{|r_R|}{|\mathbf{q}|^{1/\nu'}}, P\Big(\frac{\log |\mathbf{q}|}{\nu''} - \angle r_R \Big) \right), \tag{2.48b}$$

where $|r_R| = |r_{1_R} + i r_{2_R}| = \sqrt{r_{1_R}^2 + r_{2_R}^2}$ while $\angle r_R$ denotes the polar angle in the r_{1_R}-r_{2_R} plane. Additionally, P is a 2π-periodic function. To obtain these equations, we have used the fact that $r/l^{1/\nu' + i/\nu''}$ can be instead written as a function of $|r|/l^{1/\nu'}$ and $e^{i(\log l)/\nu'' - i\angle r}$. The former expression often appears in scaling functions of this type and characterizes the scaling of the correlation length; however, the latter gives rise to a log-periodic function as a change of $\log l \to \log l + 2\pi\nu''$ leaves the exponential invariant.

The appearance of log-periodic functions has important consequences for the critical nature of the fixed points. They lead to a discrete scale invariance rather than the characteristic continuous scale invariance at a typical critical point [129]. Rather than a self-similar behavior at all length scales, a preferred scaling factor emerges as

$$b_* = e^{2\pi\nu''}, \tag{2.49}$$

rescaling by which, or any multiple integer thereof, leaves the system scale invariant. In this sense, discrete scale invariance mimicks a fractal-like structure, in which rescaling the system by a particular factor leaves the system self similar. Note, however, that the discrete scale invariance and the fractal-like structure only emerges at long length scales (in the continuum) as opposed to the microscopic structure of a fractal (in discrete space). Additionally, if we were to consider, e.g., the effect of a physical momentum cutoff Λ, this would enter the periodic function as a phase shift, thus determining the phase of the oscillations.

Fixed Point	u_1	u_2	u_{12}	ν^{-1}	η	η'	$z-2$
NEFP	$\frac{\epsilon}{6}$	$\frac{\epsilon}{6}$	$\frac{\pm\epsilon}{2\sqrt{3}}$	$2-\left(\frac{1}{2}\pm\frac{i}{2\sqrt{3}}\right)\epsilon$	$\frac{\epsilon^2}{36}(1-12\log\frac{4}{3})$	$\frac{\epsilon^2}{36}$	$\eta'(6\log\frac{4}{3}-1)$
$O(2)$	$\frac{\epsilon}{10}$	$\frac{\epsilon}{10}$	$\frac{\epsilon}{10}$	$2-\frac{2}{5}\epsilon$	$\frac{\epsilon^2}{50}$		
Biconical	$\frac{\epsilon}{18}$	$\frac{\epsilon}{18}$	$\frac{\epsilon}{6}$	$2-\frac{1}{3}\epsilon$	$\frac{\epsilon^2}{54}$		
$\mathbb{Z}_2+\mathbb{Z}_2$	$\frac{\epsilon}{9}$	$\frac{\epsilon}{9}$	0	$2-\frac{1}{3}\epsilon$	$\frac{\epsilon^2}{54}$		

Table 2.1: Fixed point values of the coupling coefficients and critical exponents to the lowest order. In all cases, $v_R = w_R = 1$. At the NEFP, $\sigma = -1$. The decoupled $\mathbb{Z}_2+\mathbb{Z}_2$ fixed point and the biconical fixed point in this case are unstable to the order $\mathcal{O}(\epsilon)$, while the other two fixed points are stable to the same order. The $\mathbb{Z}_2+\mathbb{Z}_2$ and biconical fixed points exhibit the same critical behavior since they can be mapped to each other through a $\pi/4$ rotation in the ϕ_1-ϕ_2 plane. Fixed points involving the Gaussian fixed point are not included.

Similar phenomena appear to arise in stock markets [150], earthquakes [151], equilibrium models on fractals [152] and several other systems [129]. Log-periodic functions and the emergence of a preferred scale have been identified in the early developments of renormalization group theory [153–155], but they have been rejected as artifacts of position-space RG. On the other hand, their recent surge in diverse contexts from earthquakes to stock markets has instead relied on simple dynamical systems (with one or few variables) where the dynamics involves a discrete map itself [129]. This phenomenon has also emerged in recent works in the context of driven-dissipative quantum criticality [102, 156] as well as the dynamics of strongly-interacting nonequilibrium systems [157]. A particularly well-known example of RG limit cycles is the behavior of Efimov states [158, 159], whose binding energies form a geometric progression similar to discrete scale invariance. These quantum RG limit cycles have been noted to be closely related to Berezinskii-Kosterlitz-Thouless (BKT) phase transitions [160, 161]. Disordered systems provide another

context where complex-valued exponents and discrete scale invariance have been noted in both classical [162–166] and quantum [167] settings. The discrete scale invariance reported in this work, however, appears to be unique as it has emerged in an effectively classical yet nonequilibrium model in the absence of disorder.

The discrete scale invariance approaches a continuous one as the upper critical dimension, $d_c = 4$, is approached. In three dimensions, perturbative values at the NEFP (with $\epsilon = 1$) yield a very large scaling factor ($b_* \sim 10^9$); however, with the exponential dependence on the critical exponents, the scaling factor is sensitive even to small corrections of the exponent beyond the lowest-order perturbation theory. Nevertheless, our results should be viewed as a proof of principle for the emergence of discrete scale invariance in macroscopic nonequilibrium systems. Additionally, higher harmonics in the periodic function P can be significant, which then should be observed over smaller variations in the physical scale.

Finally, we elaborate on a possible connection between the log-periodic behavior and limit cycles. Indeed, the microscopic mean-field phase diagram near the multicritical point also includes a limit-cycle phase that displays persistent oscillations. For a rapidly oscillating limit cycle, the corresponding phase transition can be described from the viewpoint of a rotating frame (defined by the oscillation frequency) and by making the rotating-wave approximation. With this mapping, a limit-cycle phase transition is no different from a dissipative phase transition with an emergent $U(1)$ symmetry [89]. Near our multicritical point, however, the frequency of oscillations becomes small and thus no such mapping is possible. On the other hand, the discrete scale invariance discussed above also leads to an oscillatory

behavior (in both space and time), albeit one that is log-periodic. Nevertheless, a natural possibility is that, at some intermediate regime away from the multicritical point, the discrete scale invariance merges into a limit-cycle solution. Moreover, we shall see that in the doubly-ordered phase, the Liouvillian gap becomes complex-valued (see Sec. 2.4.5). This furthers the possible connection to the limit-cycle phase as a nonzero imaginary part implies that the system undergoes oscillations—which however decay—as the steady state is approached.

In Table 2.1, we summarize all of the fixed points (aside from those involving the trivial Gaussian fixed point) and their critical exponents to the lowest order.

2.4.4 Phase Diagram

The phase diagram itself is distinct in the vicinity of the NEFPs. In contrast with their equilibrium counterparts, these fixed points only give rise to a tetracritical point. With the effective magnetic field set to zero, $h = 0$, four different phases emerge: A disordered phase with $\phi_1 = \phi_2 = 0$; two phases with either $\phi_1 \neq 0$ corresponding to bistability or $\phi_2 \neq 0$ leading to antiferromagnetic ordering; and, finally, a doubly-ordered phase where both fields become ordered, $\phi_1 \neq 0 \neq \phi_2$. While the first three phases also emerge in the mean field theory of the microscopic model, the doubly-ordered phase only arises in the course of RG when the A_{20} term is generated.

The phase boundaries are governed by the scaling behavior of r_i. Let us set the effective magnetic field to zero, $h = 0$, and consider the scaling functions

characterizing the correlation and response functions in Eq. (2.39). To determine the phase boundary, it suffices to take the limit $\omega, \mathbf{q} \to 0$. In this case, the scaling functions are solely determined as a 2π-periodic function of $\frac{\nu'}{\nu''} \log(|r_R|) - \angle r_R$; this is achieved by eliminating the momentum scale in Eq. (2.48) in favor of r_R. Since the correlation functions only depend on the mass terms through the above combination, the phase boundary itself—characterized by the divergence of correlations—arises at a fixed value of this quantity (up to integer multiples of 2π). Therefore, the shape of the phase boundary is given by

$$\frac{\nu'}{\nu''} \log(|r_R|) - \angle r_R = \text{const}, \tag{2.50}$$

which is a spiral, leading to the phase diagram illustrated in Fig. 2.4. Similar to our discussion of the discrete scale invariance, the perturbative values of the exponents at $\epsilon = 1$ require very large scales to observe a full spiral. But again these scales are highly sensitive to corrections to perturbative RG. Moreover, partial spirals can still be observed for reasonable scales. Since the spiraling boundaries all spiral in the same direction, distinguishing them from equilibrium critical points, the effects of this may be seen even for very weak spiraling. Additionally, the two NEFPs are distinguished from each other by the direction of spiraling, since each has a different sign of ν''.

When the effective magnetic field is nonzero, there is no such symmetry as $\phi_1 \to -\phi_1$, leading to a surface of first-order phase transitions where ϕ_1 undergoes spontaneous symmetry breaking. This first-order transition occurs in both the uniform phase (defined by the B phase at $h = 0$) and the antiferromagnetic phase

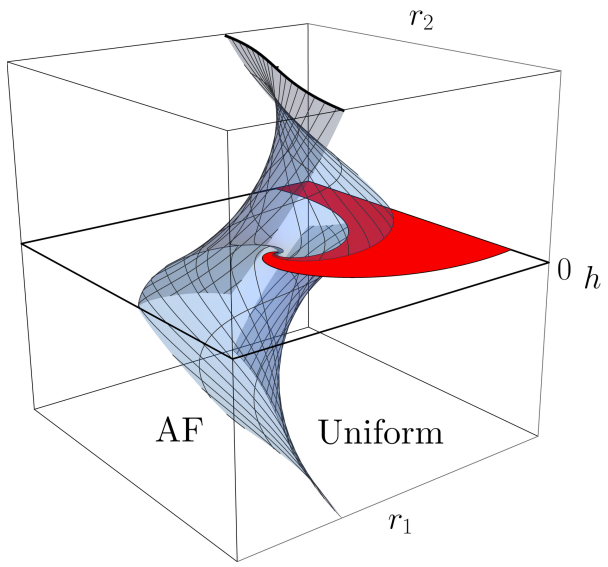

Figure 2.7: Phase diagram for (one of the two) the nonequilibrium tetracritical points as a function of effective mass terms and magnetic field. The transparent boundary indicates the location of an antiferromagnetic phase transition from a uniform phase. The horizontal (red) surface denotes a surface of first-order phase transitions. In both AF and uniform phases, the latter indicates a transition from a low- to a high-population phase; the sublattice population difference changes continuously across this surface. The (black) square boundary in the middle indicates the plane of $h = 0$. The diagram for the second nonequilibrium tetracritical point will spiral in the opposite direction.

(defined by the B+AF phase at $h = 0$). In both cases, the average population changes discontinuously while the sublattice population difference changes continuously. Finally, we take into account the magnetic field in determining the phase boundaries by considering an effective mass as $r_R + |h_R|^{1/\beta\delta}$ where β and $1/\delta$ describe the scaling behavior of the order parameter with r and h, respectively, within the ordered phase. The effect of the magnetic field h is to "unravel" the spirals for small r_i. The corresponding phase diagram for nonzero effective magnetic field is illustrated in Fig. 2.7.

2.4.5 Liouvillian Gap Closure

In this section, we investigate how the Liouvillian gap closes upon approaching the multicritical point. In contrast to the EFPs where the gap always closes along the real axis (hence, purely dissipative or relaxational dynamics), the NEFPs exhibit a qualitatively different behavior with the gap closing along a complex path, indicating an interplay between reversible and irreversible relaxation in this phase.

We consider the system in the doubly-ordered phase where both fields take nonzero expectation values M_i; for notational convenience, we make the change of variable $\phi_i \to \phi_i + M_i$ where the fields ϕ_i now represent the fluctuations around the order parameter. In addition to the original action, this transformation introduces

new quadratic and linear terms as (including the original r_1 and r_2 terms too)

$$\begin{aligned}\int_{\mathbf{x},t} &(r_1 + 3u_1M_1^2 + u_{12}M_2^2)\phi_1\tilde{\phi}_1 + (r_2 + 3u_2M_2^2 + \sigma u_{12}M_1^2)\phi_2\tilde{\phi}_2 \\ &+ 2u_{12}M_1M_2\phi_2\tilde{\phi}_1 + 2\sigma u_{12}M_1M_2\phi_1\tilde{\phi}_2 \\ &+ M_1(r_1 + u_1M_1^2 + u_{12}M_2^2)\tilde{\phi}_1 + M_2(r_2 + u_2M_2^2 + \sigma u_{12}M_1^2)\tilde{\phi}_2.\end{aligned} \tag{2.51}$$

In addition, several cubic terms are also introduced, which are not reported for simplicity. We set the vertices $\tilde{\phi}_1$ and $\tilde{\phi}_2$ to zero since, by definition, ϕ_i solely represent the fluctuations. This in turns sets $r_1 = -u_1M_1^2 - u_{12}M_2^2$ and $r_2 = -u_2M_2^2 - \sigma u_{12}M_1^2$. Upon including the effect of fluctuations to $\mathcal{O}(u)$, the remaining quadratic vertices are then given by

$$2u_{1_R}M_1^2\phi_1\tilde{\phi}_1 + 2u_{2_R}M_2^2\phi_2\tilde{\phi}_2 + 2u_{12_R}M_1M_2(\phi_2\tilde{\phi}_1 + \sigma\phi_1\tilde{\phi}_2), \tag{2.52}$$

where the coupling terms have been replaced with their renormalized values due to the inclusion of fluctuations in the form of counterterms. The other parameters are not renormalized at this order, but if we were to include higher order fluctuations, they too would be replaced with their renormalized values since the ordered phases do not give rise to any new Z factors.

Putting these terms together with the quadratic part of the action, we find

$$S_0 = \int_{\mathbf{x},t} \sum_i \tilde{\phi}_i(\boldsymbol{\gamma}\partial_t - D\nabla^2 + R_i)\phi_i - \boldsymbol{\gamma}T\tilde{\phi}_i^2 + R_{12}(\phi_2\tilde{\phi}_1 + \sigma\phi_1\tilde{\phi}_2), \tag{2.53}$$

where $R_i = 2u_{i_R}M_i^2$ and $R_{12} = 2u_{12_R}M_1M_2$. The poles of the corresponding propagators are then obtained as

$$0 = \sigma R_{12}^2 - (D\mathbf{k}^2 + R_1 + i\boldsymbol{\gamma}\omega)(D\mathbf{k}^2 + R_2 + i\boldsymbol{\gamma}\omega), \tag{2.54}$$

or more explicitly as

$$-i\gamma\omega = D\mathbf{k}^2 + \frac{R_1 + R_2}{2} \pm \sqrt{\sigma R_{12}^2 + \left(\frac{R_1 - R_2}{2}\right)^2}. \tag{2.55}$$

From this equation, we can find a simple condition for when the poles do not lie along the imaginary axis (corresponding to the negative real eigenvalues of the Liouvillian) as

$$-\sigma R_{12}^2 > \left(\frac{R_1 - R_2}{2}\right)^2. \tag{2.56}$$

Indeed, in equilibrium, where $\sigma = 1$, this condition cannot be satisfied. This implies that the relaxation is purely relaxational in equilibrium as expected (in this case, for model A). However, at the NEFPs where $\sigma = -1$, the above condition can be satisfied. To see this, let us cast the above condition for $\sigma = -1$ in terms of u and M_i as

$$4u_{12_R}^2 M_1^2 M_2^2 > (u_{1_R} M_1^2 - u_{2_R} M_2^2)^2. \tag{2.57}$$

Recalling that $u_{1_R} = u_{2_R}$ at the NEFPs at least to the lowest order in the epsilon expansion, the above condition is trivially satisfied whenever $|M_1| = |M_2|$. In this case, the pole with the lowest nonzero decay rate takes the form (with $|M_1| = |M_2| \equiv M$ and $\mathbf{k} \to 0$)

$$-i\gamma\omega = 2M^2(u_{1_R} \pm i u_{12_R}). \tag{2.58}$$

In fact, with $|M_1| = |M_2|$, the Liouvillian gap achieves its largest imaginary value relative to its real part. We can identify the ratio of the imaginary part to the real part of the gap as $\frac{u_{12_R}}{u_{1_R}} = \sqrt{3}$, which corresponds to the Liouvillian gap closing at the angle $\pi/3$ with respect to the real axis. Again, higher orders in the epsilon

expansion may modify the value of this angle. A generalization of the model considered here to the $O(N) \times O(N)$ model of N-component vector-like order parameters leads to similar behavior. In fact, we find that, for $N = 2$ and $N = 3$, the corresponding Liouvillian gap closes at the angles $\pi/4$ and $\pi/6$, respectively. We should then conclude that different nonequilibrium universality classes of our model and its generalization give rise to different angles of the Liouvillian gap closure in the complex plane. Further details on these generalized models will be presented in follow-up papers.

The scaling of (the magnitude of) the gap itself as a function of the distance from the critical point can be directly obtained by observing that the gap defines an inverse time scale which itself is associated with the exponent z. Thus the gap scales as $r^{z\nu'}$, where the exponent ν' is due to the scaling of r itself. With the order parameters M_1 and M_2 scaling similarly, the angle that defines the gap closure in the complex plane only depends on (the absolute value of) their ratio. As remarked earlier, this angle achieves its maximum when $|M_1| = |M_2|$. We further note that the gap is purely real (relaxational) near phase boundaries where only one of the order parameters undergoes a transition since the lhs of Eq. (2.57) would be suppressed compared to the rhs.

Finally, much like the discrete scale invariance in the previous section, the complex Liouvillian gap is somewhat reminiscent of limit cycles, although a true limit-cycle phase is characterized by purely imaginary eigenvalues that characterize the steady state itself.

2.5 Experimental Realization

An ideal avenue for realizing these multicritical points is via the use of cavity or circuit quantum electrodynamics (QED). Individual cavities and circuits have been studied experimentally in great depth due to their potential applications in quantum computation [12, 168, 169]. Furthermore, both cavity-QED and circuit-QED have been proposed as platforms for realizing many-body states of light via nearest-neighbor coupling arrays of cavities or circuits [11, 13, 170, 171]. Generally, these cavities and circuits have non-negligible loss due to dissipation. While dissipation is detrimental when it comes to realizing the quantum ground state of a given system, it is a crucial ingredient in realizing driven-dissipative phase transitions. There has been a variety of theoretical proposals to realize different driven-dissipative models in cavity- and circuit-QED systems [90, 93, 94, 125, 172, 173]. Recent experiments have even identified a driven-dissipative many-body phase transition [77].

For the model considered in this work (see Sec. 2.2), many-body experimental platforms already exist that include drive, hopping, as well as dissipation. The remaining ingredient is then the nearest-neighbor interaction [the quartic term in Eq. (2.1)] to be contrasted with a Hubbard term that characterizes on-site interaction. Both types of interaction are generally known as Kerr nonlinearities; we are interested in what is known as a cross-Kerr nonlinearity, which has been utilized experimentally in several few-mode systems [174–176]. A more general version of our model has been considered in Refs. [93, 94], along with a discussion on how the nonlinear interaction terms can be tuned experimentally via Josephson nanocircuits.

In a recent theoretical proposal, a setting consisting of a capacitor in parallel with a superconducting quantum interference device (SQUID) is put forth as an alternative means of achieving tunable Kerr nonlinearities [122].

While generic experimental settings introduce other nonlinear terms (e.g., Hubbard interactions and correlated hopping) in addition to the density-density interactions, we do not expect them to dramatically affect the results of this chapter. While such terms can change the location of the multicritical point [93, 94], the universal properties of the latter should not be affected by the details of the microscopic model.

We close this section by a discussion of the sign of various terms (e.g., the negative cross-Kerr nonlinearity) arising in the proposals of Refs. [93,94,122]. While a negative interaction term could lead to unbounded energy spectra, it would not pose a problem in the context of driven-dissipative systems where the steady state is not concerned with a minimum-energy ground state. Furthermore, one can change the sign of various terms in the Hamiltonian of a driven-dissipative system with a proper mapping [177]. For example, by sending $\Omega \to -\Omega$ and $a \to -a$ on one of the two sublattices, the sign of J can be changed while leaving the remaining terms fixed. Similarly, one can also map $H \to -H$ by taking the complex conjugate of the master equation, which, together with the previous mapping, allows an appropriate choice for the sign of J, V. Finally, the overall phase of Ω is unimportant while the parameter Δ can be easily directly tuned to a desired sign.

2.6 Conclusion and Outlook

In this work, we have considered an experimentally relevant driven-dissipative system where two distinct order parameters emerge that characterize a liquid-gas type transition (associated with the average density) as well as an antiferromagnetic transition (associated with the difference in the sublattice density). The two phase transitions coalesce and form a multicritical point where both transitions occur at the same time. We have investigated the nontrivial interplay of two order parameters at the multicritical point. Using a field-theoretical approach—appropriate in the vicinity of the phase transition—we have shown that the critical behavior at this point can be mapped to a nonequilibrium stochastic model described by a $\mathbb{Z}_2 \times \mathbb{Z}_2$ symmetry. Using perturbative renormalization group techniques, we have determined the RG flow equations of the model and identified a pair of new classical nonequilibrium fixed points which exhibit several exotic properties. First, we obtain two different exponents for the critical scaling of fluctuations and dissipation at the critical point, underscoring the violation of the fluctuation-dissipation relation at all scales and resulting in a behavior where the system becomes hotter and hotter at larger and larger scales. Furthermore, these NEFPs are distinguished by the emergence of discrete scale invariance and a complex Liouvillian gap even close to the critical point. Additionally, the phase diagram near these multicritical points displays spiraling phase boundaries. The latter properties could be particularly useful in identifying these NEFPs in experiments.

While generic driven-dissipative phase transitions tend to have effective equi-

librium dynamics, we have shown that the interplay between several order parameters (in this case, two) could very well lead to exotic nonequilibrium behavior. This perspective opens a new avenue to investigate and experimentally realize nonequilibrium phases and phase transitions in the context of driven-dissipative systems without relying on the engineering of complicated non-local or non-Markovian dissipation.

Future experimental and numerical studies into the NEFPs discussed in this work are crucial to develop a more complete understanding of their properties. Characterizing the discrete scale invariance, either in the dynamics or the form of the phase boundary, defines a particularly important direction. Investigating the possible emergence and the critical behavior of such nonequilibrium phase transitions in low dimensions is worthwhile. It would be particularly interesting to identify low-dimensional ordering and phase transitions which are not otherwise possible in equilibrium settings. Another question that remains open is the fate of the subspace $g_{12}g_{21} = 0$, namely if it contains new NEFPs. Beyond these nonequilibrium generalizations of model A systems, one can further consider similar nonequilibrium versions of other equilibrium universality classes. While we focused on the particular case of an experimentally-relevant model with only two scalar order parameters, our analysis indicates that a large class of new nonequilibrium multicritical points are yet to be discovered. A natural extension of our work is to identify possibly new NEFPs in $O(N_\parallel) \times O(N_\perp)$ models involving vector-like order parameters [130–136]. While a driven-dissipative condensate of polaritons has been investigated theoretically in detail [96, 97], recent experimental studies into condensate supersolids [26, 178–181]

can provide excellent platforms for probing any emergent NEFPs. In addition to the $U(1)$ symmetry of the condensate, the two coupled optical cavities can provide either an additional $\mathbb{Z}_2 \times \mathbb{Z}_2$ symmetry (corresponding to a lattice supersolid) or an approximate $O(2)$ symmetry (corresponding to a continuous supersolid).

Chapter 3: Dissipation-Induced Dipole Blockade and Antiblockade in Driven Rydberg Systems

3.1 Introduction

Ultracold atomic systems are an ideal setting for studying many-body quantum systems due to their large degree of control and tunability. Rydberg atoms in particular are a key ingredient in many of these systems, primarily for their strong, long-range interactions and long lifetimes [30,182]. Because of these features, the possibilities Rydberg atoms provide are incredibly diverse, including simulating many-body driven-dissipative systems [76,91,92,183,184], simulating topological states of matter [185,186], and applications in quantum information [30,31,187]. One aspect of several of these systems is Rydberg dressing [22,185,186,188–192], which provides a means of creating soft-core potentials and is achieved by weakly dressing a ground state with a Rydberg state [193–196]. However, recently it has been found that through spontaneous decay and blackbody radiation, nearby contaminant Rydberg states can become populated and can drastically modify the system's behavior via the resultant dipole-dipole interactions [64,197,198]. While Rydberg dressing has been achieved with up to 200 atoms [199], the possible appearance of contaminant

states necessitates a form of post-selection, with far more post-selection required to increase the strength and range of the dressed potentials or to increase the system size. On the other hand, the manner in which the dipole-dipole interactions arise is unique. Rather than coherent processes (e.g. drive) leading to interactions, we instead have a system in which a dissipative process leads to interactions. As a result, this provides an interesting platform for studying driven-dissipative systems in which coherent processes both compete with and rely on dissipation, whereas they typically only compete in most Rydberg systems.

There are two primary mechanisms which lead to the broadening induced by the dipole-dipole interactions: blockade and antiblockade. Blockading is the process in which a nominally resonant excitation becomes off-resonant due to interactions [60], which can lead to the formation of superatoms with collectively enhanced Rabi frequencies [193, 200, 201]. Complementary to this, antiblockading (also known as facilitated resonance) is the process in which a nominally off-resonant excitation becomes resonant due to interactions and plays an important role in phenomena such as Rydberg aggregation [61–63]. Both of these mechanisms play a crucial role in all Rydberg systems, but most investigations have focused on $1/r^6$ diagonal van der Waals interactions. In such systems, when the drive is resonant, blockading dominates, while when the drive is off-resonant, antiblockade often dominates. However, we are interested in $1/r^3$ off-diagonal ("flip-flop") dipole-dipole interactions. As a result of the off-diagonal nature and angular dependence of dipole-dipole interactions, blockading and antiblockading will behave qualitatively differently than for van der Waals interactions, with both effects competing with one another in complicated

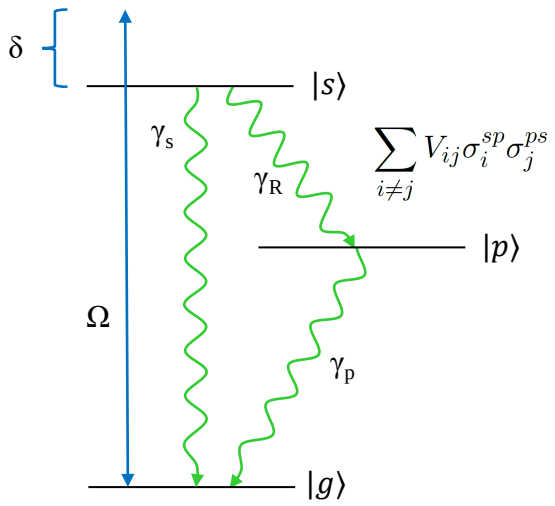

Figure 3.1: Theoretical three-level system. The g and s states are coupled via a classical laser with Rabi frequency Ω and detuning δ, while the s and p states interact via a dipole-dipole interaction $\sum_{i\neq j}\sigma_i^{sp}\sigma_j^{ps}$. There are three decay processes: $s\to g$, $p\to g$, and $s\to p$, with decay rates of $\gamma_s,\gamma_p,\gamma_R$ respectively.

ways. This complicates any attempt to truncate the Hilbert space via blockading or dephasing, which has been successful in studying Rydberg systems with diagonal interactions [202–204].

In this chapter, we study the steady states of a driven-dissipative model in which Rydberg dipole-dipole interactions are induced via dissipation as in Refs. [64, 197, 198]. In all three references, a ground state is driven to a Rydberg s state with Rabi frequency Ω and detuning δ. Through spontaneous decay and blackbody stimulated transitions, nearby (in principal quantum number) contaminant p states are populated. These p states interact strongly with subsequently driven s states via dipole-dipole interactions, leading to strong dephasing. A simplified model of this is illustrated in Fig. 3.1.

We approach this system theoretically in two different ways. The first is by

considering evolution under the full master equation and applying a cumulant expansion approximation, which allows for two-atom correlations but ignores higher-order correlations. This is motivated by the presence of dissipation, which causes high-order correlations to decay faster than low-order correlations, and allows the many-body problem to be treated numerically. This approach has previously been used in a variety of systems, including nonlinear optics [205], cavity quantum electrodynamics [206,207], and other driven-dissipative systems with similar interactions [89,208]. The second is a set of phenomenological inhomogeneous rate equations in which the decoherence strength for a given atom is determined by the population and interaction strength of neighboring contaminant states. Similar types of rate equations have been considered previously in other Rydberg systems [197,204,209,210].

For the cumulant expansion approach, we restrict our focus to the case of resonant drive ($\delta = 0$), and we consider both one-dimensional (1D) and three-dimensional (3D) systems. We find that in spite of the angular dependence and flip-flop nature of dipole-dipole interactions, a blockade radius interpretation still arises. However, the many-body blockade radius is found to be smaller than and to behave qualitatively differently from the two-body blockade radius. This occurs due to an interplay between both blockade and antiblockade effects. Additionally, the steady-state Rydberg population exhibits power law decay over several orders of magnitude as a function of interaction strength, although the decrease in population is not as pronounced as observed experimentally in Ref. [64], which is possibly due to the importance of higher-order correlations and many-body effects. Finally, we observe at high Rabi frequencies a trend away from the expected quadratic dependence of

the Rydberg population on Rabi frequency. For higher atomic densities, this trend occurs at lower Rabi frequencies. One reason to expect this is that at sufficiently low Rabi frequency, the density of Rydberg atoms becomes small and dipole-dipole interactions become irrelevant. We verify this experimentally by studying the low Rabi frequency behavior at two different densities. While there are still a number of qualitative and quantitative differences with theory, we find that the crossover occurs at lower Rabi frequencies for higher densities as expected. Furthermore, even when the scaling behavior is quadratic, the experimentally observed Rydberg populations are still much smaller than expected from single-particle physics, indicating that interactions still play an important role in this regime.

For the rate equation approach, we consider both resonant ($\delta = 0$) and off-resonant ($\delta \neq 0$) drive in 3D. While van der Waals interactions are diagonal and can be thought of as leading to an effective detuning, dipole-dipole interactions are off-diagonal and cannot be thought of in the same way. Therefore, we treat them as a source of decoherence, as the contribution to an effective detuning will depend strongly on the spatial configuration of the atoms and cannot be simply represented by a single value. Since stronger interactions will have a larger effect, we make this decoherence strength proportional to the interaction strength and population of the contaminant states. Finally, we focus on inhomogeneous rate equations to reflect the inherent inhomogeneity in the system due to spontaneous decay. We find that such an approach accurately captures the experimentally observed behavior of the Rydberg population in Ref. [64], both on resonance and off resonance. Furthermore, the exact details of how the decoherence is implemented primarily affects

the Rydberg population lineshapes, while the qualitative scaling behavior remains unchanged. However, this model fails to accurately capture both the early time and low Rabi frequency behavior. In these regimes the number of contaminant atoms is small and individual Rydberg atoms can affect the system more easily, so the spatial configuration of the atoms, and thus their correlations, play a more important role.

The remainder of the chapter is organized in the following manner. In Sec. 3.2, we describe our theoretical approaches to this system, including the details of the cumulant expansion approximation and our phenomenological inhomogeneous rate equations. In Sec. 3.3, we present the theoretical results of the cumulant expansion approximation as well as an experimental examination of the crossover from quadratic to linear dependence of the Rydberg population on Rabi frequency. In Sec. 3.4, we present the theoretical results of our phenomenological inhomogeneous rate equations and compare them to the experimental results of Ref. [64]. Finally, in Appendix B, we include several details omitted from the main text.

3.2 Theoretical Models

In order to study the effect of contaminant p states on driven-dissipative Rydberg systems, we consider a three-level system composed of states $|g\rangle$, $|s\rangle$, and $|p\rangle$, corresponding to the ground, ns, and mp states, where n and m are the principal quantum numbers of the s and p Rydberg states, respectively. Although there are generally multiple mp states with large enough dipole matrix elements with the ns state to affect the dynamics of the system, we consider here only one contaminant

p state for simplicity. We also assume a nonzero magnetic field, as is the case in Refs. [64, 197, 198]. Our effective three-level model is illustrated in Fig. 3.1.

The transition between $|g\rangle$ and $|s\rangle$ is driven via a classical laser with Rabi frequency Ω and detuning δ, where we have chosen to define our Rabi frequency as half of the traditional definition to avoid carrying around extra factors of two. Additionally, the $|s\rangle$ and $|p\rangle$ states will interact according to a flip-flop dipole-dipole interaction. While van der Waals interactions are typically present, we ignore them here since they are weak compared to the dipole-dipole interactions that we want to study. Together, these result in the following Hamiltonian

$$H = \sum_i [-\delta\sigma_i^{ss} + \Omega(\sigma_i^{gs} + \sigma_i^{sg})] + \sum_{i \neq j} V_{ij}\sigma_i^{sp}\sigma_j^{ps}, \tag{3.1}$$

where we define operators $\sigma_i^{\alpha\beta} = |\alpha\rangle_i\langle\beta|_i$. The last sum is over both i and j. The interaction strength between atoms i and j is given by

$$V_{ij} = \frac{C_3}{r_{ij}^3}(1 - 3\cos^2\theta_{ij}), \tag{3.2}$$

where C_3 defines the strength of the dipole-dipole interactions, r_{ij} is the separation between atoms i and j, and θ_{ij} is the angle the displacement vector $\mathbf{r}_{ij}$ makes with the quantization axis, which is determined by the magnetic field. While there are dipole-dipole interactions which have a different angular dependence, they are off-resonant due to Zeeman shifts from the magnetic field and are less relevant as a result. However, for sufficiently strong interactions relative to the Zeeman shifts, these interactions could potentially play a more important role.

In addition to Hamiltonian dynamics, decay also plays a crucial role as the source of the contaminant p states. We treat both aspects according to a master

equation description

$$\dot{\rho} = -i[H, \rho] + \gamma_s \mathcal{L}_s[\rho] + \gamma_p \mathcal{L}_p[\rho] + \gamma_R \mathcal{L}_R[\rho], \tag{3.3}$$

where γ_s, γ_p, and γ_R are the decay rates from $|s\rangle$ to $|g\rangle$, $|p\rangle$ to $|g\rangle$, and $|s\rangle$ to $|p\rangle$ respectively. We ignore blackbody radiation from the p state back to the s state since most of the corresponding blackbody radiation goes to other s and d states. Throughout this chapter, we will take $\gamma_s = \gamma_p = 1$ and $\gamma_R = .3$, which provides comparable branching ratios to Ref. [64], although this comparison is complicated by the fact that there are many relevant p states as well as decay to non-participating ground states. The associated Lindblad operators for decay $\mathcal{L}_s$, $\mathcal{L}_p$, and $\mathcal{L}_R$ are given below

$$\mathcal{L}_s[\rho] = \sum_i \left[\sigma_i^{gs} \rho \sigma_i^{sg} - \frac{1}{2}\{\rho, \sigma_i^{ss}\} \right], \tag{3.4a}$$

$$\mathcal{L}_p[\rho] = \sum_i \left[\sigma_i^{gp} \rho \sigma_i^{pg} - \frac{1}{2}\{\rho, \sigma_i^{pp}\} \right], \tag{3.4b}$$

$$\mathcal{L}_R[\rho] = \sum_i \left[\sigma_i^{ps} \rho \sigma_i^{sp} - \frac{1}{2}\{\rho, \sigma_i^{ss}\} \right]. \tag{3.4c}$$

We are most interested in the steady state of the above master equation. However, this can only be determined numerically for up to approximately ten atoms, far from any sort of long-range many-body behavior we are interested in. One common approach to this problem is to use Gutzwiller mean field theory, which ignores the effects of correlations and assumes the steady-state density matrix is a product state [137, 138]. In Appendix B.1, we explain why this technique fails to capture the behavior of our model. Instead, we will approach the problem via a cumulant expansion approximation, which we discuss below.

3.2.1 Cumulant expansion

Rather than truncate the hierarchy of differential equations at the level of single atom operators as in Gutzwiller mean field theory, we instead use a second-order cumulant expansion approximation, which continues one step further and allows for correlations between pairs of atoms [205–208]. Formally, this amounts to making the following approximation

$$\langle \mathcal{A}_i \mathcal{B}_j \mathcal{C}_k \rangle = \langle \mathcal{A}_i \mathcal{B}_j \rangle \langle \mathcal{C}_k \rangle + \langle \mathcal{C}_k \mathcal{A}_i \rangle \langle \mathcal{B}_j \rangle + \langle \mathcal{B}_j \mathcal{C}_k \rangle \langle \mathcal{A}_i \rangle - 2 \langle \mathcal{A}_i \rangle \langle \mathcal{B}_j \rangle \langle \mathcal{C}_k \rangle, \tag{3.5}$$

where i, j, k correspond to distinct atoms and $\mathcal{A}, \mathcal{B}, \mathcal{C}$ are single atom operators ($\sigma^{\alpha\beta}$ in our model). This is equivalent to setting all three-atom and higher connected correlations to zero. The nth-order connected correlation accounts for inherently n-body correlations which cannot be understood in terms of lower-order correlations. This truncation reduces a set of $\sim 9^N$ equations to a set of $\mathcal{O}(N^2)$ equations, where N is the number of atoms. This is justified under the assumption that two-atom correlations will dominate, which is often the case when dissipation and decoherence are involved. However, higher densities and interaction strengths mean a given atom will interact with a larger number of atoms, which leads to more relevant many-body effects, and the approximation is less valid in this limit.

Restricting our focus to a lattice with unit filling, we may use translational symmetry and truncate correlations past a certain distance (where they are negligible) in order to reduce this further to a set of $\mathcal{O}(M)$ equations, where M is the number of displacement vectors considered. For 3D, we take all correlations

involving distances greater than 16 times the lattice spacing to be zero. For 1D, we choose this distance to be 100 times the lattice spacing. Furthermore, we take advantage of the four different reflection symmetries present in the dipole interaction in 3D, reducing the number of nonlinear coupled ordinary differential equations by a further factor of 16. Finally, there is also a $U(1)$ symmetry present in the form of $|p\rangle \rightarrow e^{i\phi}|p\rangle$, which forces some terms in the density matrix to be zero in steady state. Since we are assuming correlations past a certain distance to be negligible, we restrict the strength of C_3 so that the interaction strengths beyond this distance are not large compared to the decay rates. By using these symmetries, we are able to consider large system sizes and, correspondingly, large interaction strengths. Steady-state behavior is found by numerically integrating the resultant effective equations of motion using a 4th-order Runge-Kutta method. Examples of the resultant effective nonlinear equations of motion are given in Appendix B.2.

To understand whether we can expect the cumulant expansion to give reasonably accurate results, we use a quantum trajectories approach [211–214]. We compare the results of the approximate cumulant expansion with the exact numerics of quantum trajectories for small system sizes. We find that both approaches produce results that are similar in this limit, with Rydberg populations generally differing by no more than 5%. While the rest of this chapter focuses on parameter regimes well outside this limit, this demonstrates that this approximation can capture the effects of the interactions. The results of this comparison are covered in detail in Appendix B.3.

3.2.2 Inhomogeneous Rate Equations

In addition to the cumulant expansion approach on resonance, we also study a set of phenomenological inhomogeneous rate equations. The fundamental assumption we make in forming these rate equations is that rather than an effective shift in the detuning of individual sites, nearby p atoms cause dephasing proportional to their interaction strength. This is motivated by the fact that the dipole-dipole interactions are off-diagonal, so their effect cannot be strictly understood in terms of effective detunings. Additionally, we take these rate equations to be spatially inhomogeneous by considering atoms which are independently and identically distributed according to a 3D Gaussian probability distribution. This is done to capture the fact that in a real system, the spontaneous decay will lead to a spatially inhomogeneous distribution of p atoms. These assumptions lead to the following set of rate equations

$$\dot{s}_i = R_i(g_i - s_i) - (\gamma_s + \gamma_R)s_i, \tag{3.6a}$$

$$\dot{p}_i = \gamma_R s_i - \gamma_p p_i, \tag{3.6b}$$

$$\dot{g}_i = -R_i(g_i - s_i) + \gamma_s s_i + \gamma_p p_i, \tag{3.6c}$$

where the pumping rate R_i is given by

$$R_i = \frac{\Omega^2}{\delta^2 + \Gamma_i^2/4}\Gamma_i, \tag{3.7}$$

and the dephasing rate Γ_i is given by

$$\Gamma_i = \gamma_s + \gamma_R + C_3 \left| \sum_{j \neq i} V_{ij} p_j \right|. \tag{3.8}$$

The variables s_i, p_i, g_i refer respectively to the s, p, g populations at site i.

One important feature of these rate equations is that the scaling behavior of the steady state population is generally insensitive to the exact manner in which the interactions are included in the dephasing rate, and several different choices produce the observed experimental scaling. They primarily differ in the coefficient of the linewidth and of the resonant Rydberg population scaling as well as the resultant lineshapes. For example, Ref. [198] considers a set of homogeneous rate equations with $\Gamma = \gamma_s + \gamma_R + n_{3\mathrm{D}} C_3 p$, where $n_{3\mathrm{D}}$ ($n_{1\mathrm{D}}$) is the density of atoms in 3D (1D). This model captures many features of the width behavior, but it predicts dome-like lineshapes rather than the experimentally observed Lorentzian lineshapes. Similarly, the spatial distribution of atoms in these types of models can also affect the lineshape, with a lattice distribution often leading to more dome-like lineshapes in general. Our choice of effective dephasing is the simplest choice we have found which results in near-Lorentzian lineshapes. We compare the lineshapes of these other approaches in more detail in Appendix B.4.

3.3 Cumulant Expansion Results

3.3.1 Divergences

In this section, we discuss the results of the cumulant expansion approximation, which takes third-order and higher connected correlations to be zero. As mentioned previously, we will set $\gamma_s = \gamma_p = 1$ and $\gamma_R = .3$ throughout this section, which produces similar branching ratios to the experimental setup in this chapter

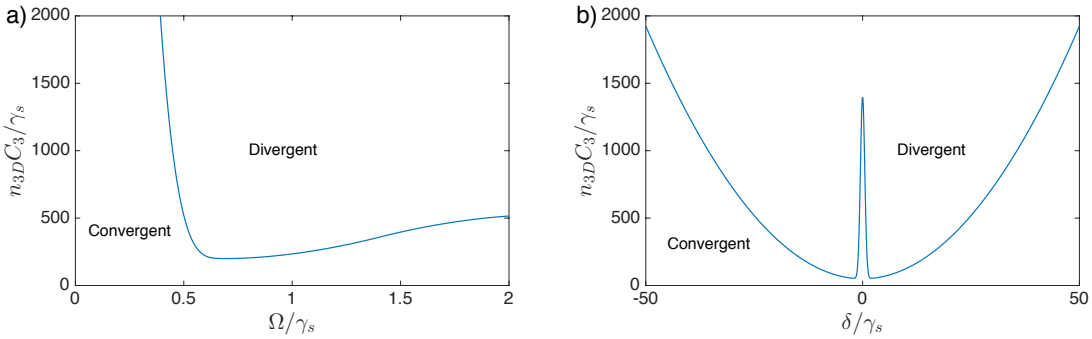

Figure 3.2: Approximate divergence diagrams for cumulant expansion in 3D. (a) Divergence diagram on resonance ($\delta = 0$). Most of the low Rabi frequencies on resonance are convergent, although they become less stable as the interactions are increased. Sufficiently large Rabi frequencies are also convergent, where steady-state populations begin to saturate. (b) Divergence diagram for $\Omega/\gamma_s = .4$. A very narrow region near resonance is convergent for sufficiently small interaction strengths. The outer edges of the divergent region grow approximately quadratically in detuning in this parameter regime.

and in Ref. [64].

One issue that can arise under this approximation is the presence of unphysical divergences. Although we focus our attention on resonance, these divergences generally occur at intermediate detunings and Rabi frequencies. Rather than divergences due to numerical error, these divergences appear to be fundamental instabilities of the nonlinear differential equations, where there is only a single, unstable steady state. Furthermore, these divergences are less present in 1D systems, but they are very relevant in 3D systems. The origin of these instabilities is most likely the importance of the higher-order correlations that we have ignored [205], although finite size effects could play a role as well.

In Fig. 3.2 we plot a diagram showing the approximate parameter regimes where the cumulant expansion leads to a divergence. The regions where one would expect high-order correlations to be more important are exactly those where the

divergences are present. The vast majority of the data in Ref. [64] is well into these divergent regions, with $C_3 n_{3\mathrm{D}}/\gamma_s$ often an order of magnitude larger than what we can treat numerically. Interestingly, the outer edge of the divergent region appears to grow approximately as $\delta \propto \sqrt{C_3 n_{3\mathrm{D}}/\gamma_s}$. This is exactly the experimentally observed scaling behavior of the linewidth as a function of interaction strength, so the observed scaling of the linewidths may be reflected in the behavior of the divergences. As the interaction strength is increased, the linewidth increases, expanding the region where high-order correlations are important. Additionally, if we increase γ_R or decrease γ_p, the size of these divergent regions tends to increase due to the increase in the number of p atoms relative to the number of s atoms. Thus if high-order correlations are the origin of the divergences, we would expect these divergences to grow in the same manner as the lineshapes themselves, which is exactly what we find.

In order to determine the Rydberg populations in divergent parameter regimes, we further consider two more terms in the master equation that represent decoherence on the $|s\rangle$ and $|p\rangle$ states.

$$\mathcal{L}_d^s[\rho] = \gamma_d^s \sum_i \left[\sigma_i^{ss} \rho \sigma_i^{ss} - \frac{1}{2}\{\rho, \sigma_i^{ss}\} \right], \tag{3.9a}$$

$$\mathcal{L}_d^p[\rho] = \gamma_d^p \sum_i \left[\sigma_i^{pp} \rho \sigma_i^{pp} - \frac{1}{2}\{\rho, \sigma_i^{pp}\} \right], \tag{3.9b}$$

where γ_d^s and γ_d^p correspond to the strength of decoherence on $|s\rangle$ and $|p\rangle$, respectively. We set $\gamma_d^s = \gamma_d^p = \gamma_d$ for simplicity. In terms of the differential equations themselves, this amounts to including extra decay on the coherences but not on the populations. When a sufficient amount of decoherence is included, parameter

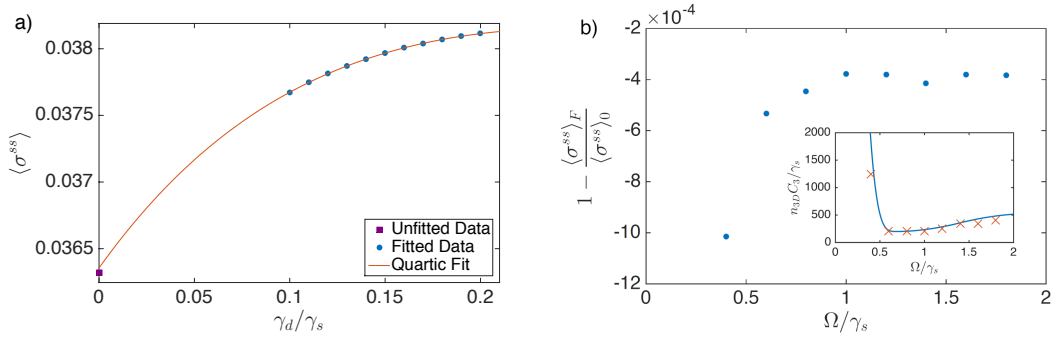

Figure 3.3: Illustration of how fitting the Rydberg population as a function of decoherence is used to approximate the Rydberg population in divergent regions. (a) $n_{3\mathrm{D}}C_3/\gamma_s = 1250, \Omega/\gamma_s = .4$. The orange line corresponds to a quartic fit of the blue circles where $\gamma_d/\gamma_s > .1$. The purple square denotes the population for $\gamma_d = 0$, which is convergent for these parameters. (b) Relative error of Rydberg population extracted from a $\gamma_d/\gamma_s > .1$ fit compared to actual Rydbeg population at $\gamma_d = 0$, denoted $\langle\sigma^{ss}\rangle_{\mathrm{F}}$ and $\langle\sigma^{ss}\rangle_0$ respectively, for several choices of parameters just outside of the divergent region. The inset shows the parameters used in the divergence diagram on resonance, where the orange $\times$'s denote the parameters used and the blue line separates the convergent and divergent regions, with the top right corresponding to the divergent region.

regimes which were formerly divergent become convergent. This is consistent with the understanding that the instabilities are a result of the importance of higher-order correlations, since decoherence decreases correlations. We focus on the cases of resonant drive because they only require a small amount of extra decoherence to become convergent. The amount of decoherence necessary for convergence ($\gamma_d/\gamma_s \approx .1$) is small compared to the decay rates and certainly smaller than any potential experimental source of decoherence which we have not included in our model.

More importantly, the effect of increasing decoherence modifies the steady-state population in a simple way. As one crosses from the convergent region to the divergent region, the convergent steady state continuously becomes a divergent steady state. This provides a way to estimate the expected population when no decoherence is included. We achieve this by fitting the numerics for different de-

coherences and extrapolating the population at $\gamma_d = 0$ according to the fit. The accuracy of this technique is illustrated in Fig. 3.3, where we apply it to several choices of parameters just outside of the divergent region. The populations we extrapolate from the fits differ from the actual populations at γ_d by at most one tenth of a percent. However, as one moves far into the divergent regime, this method becomes increasingly less accurate because stronger decoherence is necessary for convergence.

3.3.2 Blockade Radius Reduction

A concept that is often useful to consider in Rydberg systems is the blockade radius [60, 200, 201]. Although in this case we are not considering the usual $1/r^6$ diagonal van der Waals interactions, the general effect of interactions suppressing excitations will occur in a similar fashion. However, due to the off-diagonal nature of the interactions, the effect of blockading will be modified in a non-trivial way in many-body systems.

The blockade radius r_b is often defined as the distance at which the interaction strength is equal to the effective Rabi frequency, $V(r_b) = \Omega_{\text{eff}}$. The effective Rabi frequency is defined self-consistently as $\Omega_{\text{eff}} = \sqrt{N_b}\Omega$, where N_b is the number of atoms in a blockade volume. In this limit, where only one excitation is possible within a blockade volume, a superatom picture arises in which many atoms behave as an effective two-level atom [201, 215]. Since each Rydberg superatom blockades a volume of $V_b \propto r_b^3$, the total number of Rydberg atoms is proportional to $1/V_b$. One

might naïvely expect to apply a similar analysis in the case of the contaminant p states, with each producing a large blockade volume in which s atoms can no longer be excited or de-excited. However, were this the case, the Rydberg populations in Ref. [64] would be much lower than observed because the long-range behavior of the dipole-dipole interaction corresponds to blockade volumes that are on the order of the system size, while the corresponding populations of Rydberg states can be in the hundreds. As a result, the size of the blockade volume due to the contaminant states, if one exists, must be significantly smaller in order to account for the observed Rydberg populations.

In a many-body Rydberg system, individual atoms are affected by interactions due to multiple atoms. In the case of diagonal van der Waals blockading, these interactions will only serve to further blockade any given excitation. On the other hand, in the case of off-diagonal dipole-dipole interactions this will not be the case, even when all matrix elements V_{ij} are positive. This can be understood by considering two atoms whose dipole-dipole interaction has a strength of V. Because the interactions are off-diagonal, the corresponding eigenvalues are $\pm V$. As a result, if two p atoms are each blockading an atom in the ground state, then it becomes possible for the blockade effects to interfere and effectively cancel each other out, allowing the ground state atom to be excited. In a many-body system, this becomes more complicated, with many different atoms taking part in a given excitation.

In order to observe this effect, we will consider both 1D systems, whose matrix elements V_{ij} are all the same sign, and 3D systems, whose matrix elements V_{ij} may be positive or negative. Additionally, the blockade radius will be defined according

to the connected correlations between s and p states,

$$\langle \sigma_0^{pp} \sigma_{\mathbf{r}}^{ss} \rangle_c = \langle \sigma_0^{pp} \sigma_{\mathbf{r}}^{ss} \rangle - \langle \sigma_0^{pp} \rangle \langle \sigma_{\mathbf{r}}^{ss} \rangle. \tag{3.10}$$

These correlations describe how a p atom at the origin affects the likelihood there is an s atom at $\mathbf{r}$. When the strength of the dipole-dipole interaction between two atoms is strong compared to the Rabi frequency, the connected correlation will be negative and approximately constant. A negative connected correlation corresponds to the effect of blockade, as it indicates a decreased likelihood for an s atom to be present near a p atom. It is constant for large interaction strengths because increasing the interaction strength further only serves to move a far off-resonant excitation further away from resonance, so the s state will be strongly blockaded in either case.

Unlike in the case of the 1D system, the 3D system can have small interactions for short distances because of the dipole-dipole interaction's angular dependence. As a result, the concept of a blockade radius is slightly modified, so we will instead consider an effective distance

$$r_{\text{eff}} = r/|1 - 3\cos^2\theta|^{1/3}. \tag{3.11}$$

Under this definition, sites which do not interact with each other are considered as being infinitely far apart. While in reality these nearby sites will affect each other due to higher-order processes even if they do not interact, this effective distance reduces the effects of the anisotropic nature of the dipole-dipole interactions, providing a useful way to understand how the effect of blockading is modified in many-body systems.

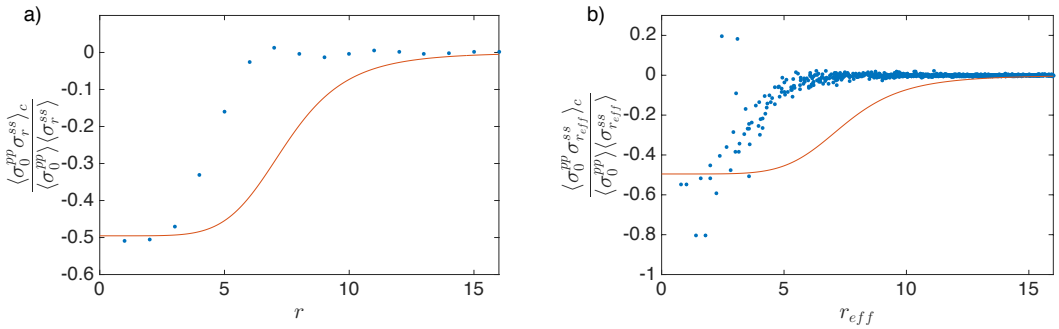

Figure 3.4: Correlations between s and p atoms for $\Omega/\gamma_s = .4$. The blue dots are from the cumulant expansion while the orange line corresponds to exact calculations for just two atoms separated a distance r. These are plotted in (a) 1D for $n_{1\mathrm{D}}^3 C_3/\gamma_s = 800$ and (b) 3D for $n_{3\mathrm{D}} C_3/\gamma_s = 800$.

In Fig. 3.4, we plot examples of the connected correlations for a 1D system and a 3D system. As expected, we see that for small distances the connected correlations are negative and approximately constant, with the 3D system showing more fluctuations due to many-body effects and the angular dependence of the interactions. As the distance is increased, these correlations drop off to zero, indicating a lack of any correlation due to negligible interaction strength. In 1D, there is some oscillation in the correlations after $r = 7$. This likely arises in a similar manner to the emergence of staggered order in other driven-dissipative Rydberg system, in which the blockading of nearby atoms prevents further atoms from being similarly blockaded [76, 91, 183]. There are also some outliers in the 3D correlations, which likely arise via a combination of many-body effects, the use of r_{eff}, and artifacts from the cumulant expansion approximation. Finally, we note that the many-body blockade radius is clearly smaller than the two-body blockade radius in both cases, illustrating the presence of antiblockade effects.

In order to extract an effective blockade radius from these connected corre-

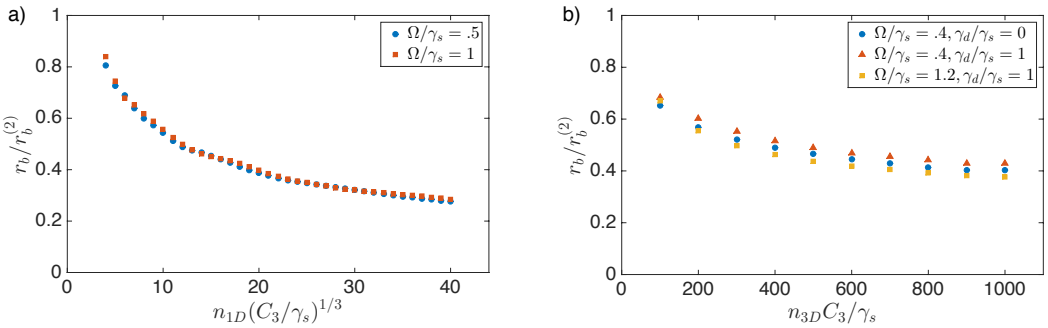

Figure 3.5: Ratio of the many-body blockade radius r_b to the two-body blockade radius $r_b^{(2)}$ as a function of interaction strength. (a) 1D system with $\gamma_d = 0$ for all points. (b) 3D system with examples of both $\gamma_d = 0$ and $\gamma_d \neq 0$.

lations, we will consider the distance or effective distance at which the connected correlations decrease by a factor of 1/2. To reduce the effect of the fluctuations in the 3D system, the correlation at an arbitrary effective distance is defined by an average of the correlations from the cumulant expansion in a range of $\Delta r_{\text{eff}} = 1$, effectively smoothing out the numerics.

In Fig. 3.5, we consider the ratio of the many-body blockade radius to the two-body blockade radius $r_b^{(2)}$, which is defined as the value of r at which the connected correlations decrease by a factor of 1/2 relative to the short distance connected correlations in a system of only two atoms. At small densities and interaction strengths, this ratio approaches one, as is expected. However, once we consider larger densities and interaction strengths, the ratio begins to decrease, demonstrating the effect of the competition between blockade and antiblockade effects.

Remarkably, the trend is qualitatively similar for both small and large Rabi frequency, regardless of whether the system is in 1D or 3D. Furthermore, including decoherence does not drastically change the quantitative behavior in 3D. However, this similarity in behavior does not appear to hold for arbitrary Ω. By solving the

cumulant expansion equations of motion perturbatively in Ω, it can be shown that to lowest order in Ω, the ratio of the many-body blockade radius to the two-body blockade radius is one. This result reflects the fact that when one goes to sufficiently small Rabi frequencies, the Rydberg population becomes small, so it is rare to have two or more nearby p atoms to give rise to many-body effects.

3.3.3 Rydberg Population Scaling

Next, we are interested in understanding how the Rydberg population is affected by dipole-dipole interactions. Although the many-body blockade radius is smaller than the two-body blockade radius at large interaction strengths, both increase as the interaction strength is increased, so we should expect to see a corresponding decrease in the Rydberg population. Fig. 3.6 illustrates the steady-state population's dependence on interaction strength for both 1D and 3D systems. The population appears to decrease according to a power law with a fitted exponent of $-.055$ for 1D and $-1/5$ for 3D, observed over four and two orders of magnitude respectively. These exponents appear to be relatively insensitive to changes in the decay rates. For example, if we double γ_p in 1D, the corresponding exponent remains close to $-.055$.

Particularly in 3D, there is some deviation from purely power law behavior, with a faster fall-off at small interaction strengths compared to large interaction strengths. This is the opposite of what one might normally expect for power law behavior. When there are no interactions, the population is given by some constant, so

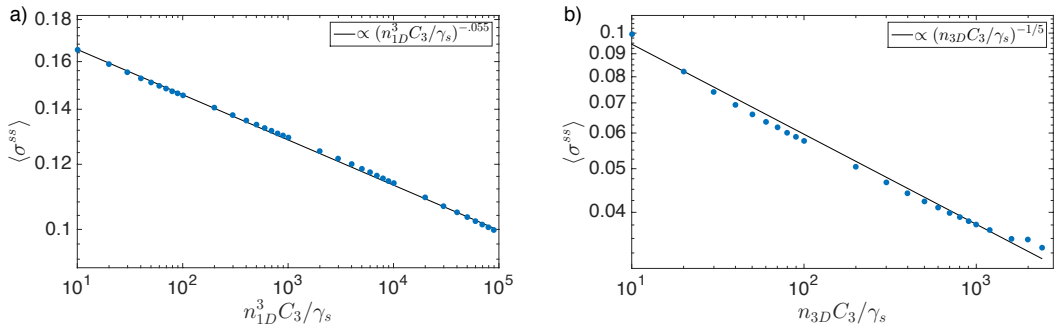

Figure 3.6: Steady-state s state population dependence on interaction strength for $\Omega/\gamma_s = .4$. (a) 1D system with best fit power-law with exponent of $-.055$. (b) 3D system with best fit power-law exponent of $-1/5$.

we would expect a slower fall-off at small interaction strengths. Since the cumulant expansion is more accurate for weak interactions, the fact that we do not see this indicates that if we were to solve the full master equation, we would probably see a faster fall-off at large interactions than what we see here. As a result, we expect the full master equation to result in a scaling behavior much closer to the experimentally observed exponent of $-1/2$ [64]. A likely source of this behavior is that at higher interaction strengths, higher-order correlations become more important, and ignoring these correlations ignores relevant blockading effects. However, in order to confirm this hypothesis theoretically, it is important to account for higher-order correlations, which is difficult to achieve in practice.

We are also interested in understanding the population's dependence on the Rabi frequency, which was originally observed to be closer to linear dependence rather than the quadratic behavior of a non-interacting system [64]. However, at sufficiently small Rabi frequencies, the density of s excitations will be so small that interactions will become irrelevant, at which point quadratic behavior should be restored. This can be seen by treating the system perturbatively in Ω, which results

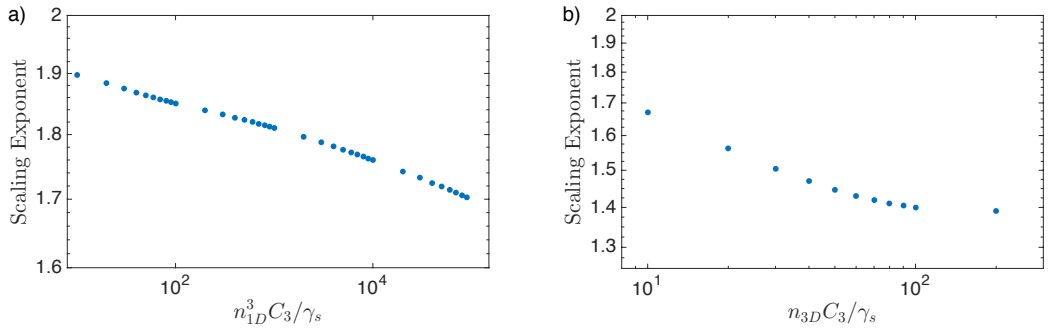

Figure 3.7: Scaling exponent b from fit of $\langle \sigma^{ss} \rangle = a\Omega^b$ for $\Omega/\gamma_s = .05, .1$ as a function of interaction strength. (a) 1D system. (b) 3D system with data only up to $n_{3D}C_3/\gamma_s = 200$ due to finite size effects.

in $\langle \sigma^{ss} \rangle \approx \frac{4\Omega^2}{(\gamma_s+\gamma_R)^2}$ to lowest order. This is the same perturbative result as for a non-interacting system.

We observe this effect in Fig. 3.7, where we find the fit of the population for two points $\Omega = .05\gamma_s, .1\gamma_s$ using the function $\langle \sigma^{ss} \rangle = a\Omega^b$. The value of b is essentially an approximation of the slope on a log-log plot for $\Omega \approx .05\gamma_s$. As the Rabi frequency is increased, this slope will decrease, transitioning from quadratic behavior towards linear behavior. As the interaction strength is increased, this exponent decreases, indicating that the departure from quadratic behavior is happening at lower Rabi frequencies, allowing for a possible linear behavior over a large range of Rabi frequencies. Additionally, since the Rydberg population is suppressed more for larger interactions, reaching saturation will require stronger Rabi frequencies, expanding the possible range of linear behavior even further. For 3D, we only consider a maximum interaction strength of $n_{3D}C_3/\gamma_s = 200$. This is because past this point, the interactions at the furthest distances we allow become comparable to the small Rabi frequencies considered and the numerics become less accurate. In spite of this restriction on the range of interaction strengths we can consider,

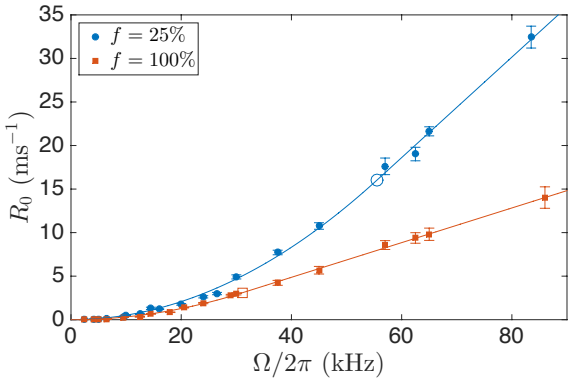

Figure 3.8: Resonant pumping rate as a function of Rabi frequency for two atomic densities, where f corresponds to the fractional density of atoms initially in the driven ground state and $f = 100\%$ corresponds to a density of 57 μm^{-3}. Blue circles (red squares) are from experimental data for $f = 25\%$ ($f = 100\%$) and lines are from fits of Eq. (3.12). The empty blue circle and red square correspond to the fitted crossover Rabi frequency Ω_c for each density, denoting the crossover from quadratic to linear scaling in Rabi frequency. Error bars represent the one standard deviation from exponential fits to extract the pumping rates.

we see that the extracted exponent decreases at a much faster rate in the higher dimensional system.

In order to determine whether this behavior corresponds to a real effect or simply an artifact of the cumulant expansion approximation, we study this change in scaling behavior experimentally. Using the same experimental setup as in Ref. [64], we consider the scaling behavior for two different densities which differ by a factor of four. In Fig. 3.8, we plot the resonant pumping rate as a function of Rabi frequency for the two different densities. The pumping rate gives the rate at which atoms are pumped out of the relevant three-level system of Fig. 3.1 once a quasi-steady-state has been reached. Further experimental details can be found in Appendix B.5. This pumping rate provides a good approximation of the steady-state population of Rydberg atoms $\langle \sigma^{ss} \rangle \approx \frac{R_0}{\gamma'}$, where γ' is the total decay rate from the s state,

including decay which takes an atom to an undriven ground state. For both densities, we have determined a best fit using the function

$$R_0 = \begin{cases} a\Omega^2 & \Omega < \Omega_c \\ a\Omega_c(2\Omega - \Omega_c) & \Omega \geq \Omega_c \end{cases} \tag{3.12}$$

This describes a continuous, smooth function which changes from quadratic scaling to linear scaling at a critical value of Rabi frequency Ω_c. While in reality the change in scaling behavior may be more gradual, this gives a useful way of determining where the scaling behavior change occurs. We find that $\frac{\Omega_c}{2\pi} = 31 \pm 1$ MHz for the higher density and $\frac{\Omega_c}{2\pi} = 55 \pm 2.5$ MHz for the lower density, where the uncertainty corresponds to one standard deviation from the fits. This clearly illustrates that the scaling behavior changes at smaller Rabi frequencies for higher density samples. We further note that although the quadratic regime is visible at low Rabi frequencies, the corresponding populations are still well below the single-particle limit. This indicates that the quadratic behavior extends beyond the single-particle physics considered above. While this crossover is fairly clear in the experiment, theoretically we see a much more gradual crossover. This could be due to finite size effects or van der Waals interactions, which we have ignored in our model.

3.4 Rate Equation Results

In this section, we will discuss the results of our phenomenological rate equation approach in Eqs. (3.6-3.8) with the aim of comparing the lineshapes, scaling behavior of the resonant Rydberg population, and the scaling behavior of the

linewidths to the experimental results in Ref. [64]. Due to computational constraints, we will restrict ourselves to considering 1080 atoms independently and identically distributed according to a 3D Gaussian probability distribution with relative spatial dimensions of $2 \times 4 \times 5$, which is similar to the experimental setup. The density n_{3D} will be taken to be the density at the center of the distribution. Using a uniform probability distribution gives similar results. Although we will vary $n_{3D}C_3$ rather than the total number of atoms, both approaches result in quantitatively similar behavior.

While the experiment takes place in a lattice, we consider a random distribution to help capture the fact that at any given time, the distribution of the p atoms themselves will be random due to dissipation and will not fully exhibit the structure of the lattice. Additionally, when a lattice distribution is used instead of a random, inhomogeneous distribution, this tends to make the resulting lineshapes highly non-Lorentzian. Further details about this may be found in Appendix B.4.

The existence of a steady state can be influenced by the manner in which interactions are included in the dephasing. For the choice we are considering here, there are some regions in which no steady-state solution exists. At the edges of such regions, the long-time behavior is periodic, exhibiting limit cycles. Further into these parameter regimes, this periodic behavior likely continues, although the time to reach the limit cycles becomes prohibitive due to the number of atoms in the system. However, in either case the average population of all atoms approaches an approximate steady-state value relatively quickly, with only small deviations from this value as a function of time. This is illustrated in Fig. 3.9, where $\langle \sigma^{ss} \rangle_{\text{ave}}$ denotes

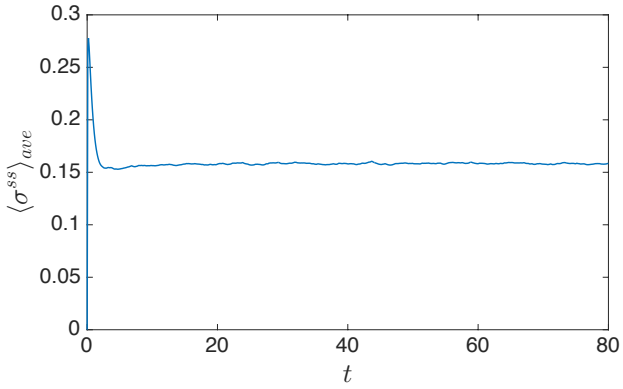

Figure 3.9: Example of the time dependence of the s population ensemble average $\langle\sigma^{ss}\rangle_{\text{ave}}$ on resonance in units of γ_s^{-1}. While neither a steady state nor a limit cycle is reached quickly, $\langle\sigma^{ss}\rangle_{\text{ave}}$ very quickly approaches an approximate steady-state value, whose time average we will denote by $\langle\sigma^{ss}\rangle$ for simplicity.

the time-dependent ensemble average of the Rydberg s population. Thus we may take a time average of the s state ensemble average in order to find a good approximation of the s population. From here on out, we will write the time average of the s state ensemble average as $\langle\sigma^{ss}\rangle$ for simplicity. We find that our phenomenological rate equations produce scaling behavior which is remarkably similar to the experimentally observed scaling behavior as well as very Lorentzian lineshapes.

As mentioned before, the exact manner in which the interactions are included in the decoherence can have an effect on the behavior of the steady-state populations. For example, if a homogeneous set of rate equations is used in which the decoherence is merely proportional to $n_{3\text{D}}C_3$ times the average p population, this will give reasonable scaling behavior, but it will also result in dome-shaped lineshapes which drop off much faster than a Lorentzian. However, this homogeneous approach ignores the importance of the spatial distribution of the p atoms, which influences the strength and nature of the interactions and thus the decoherence. In order to capture this behavior, some form of inhomogeneity should be included in

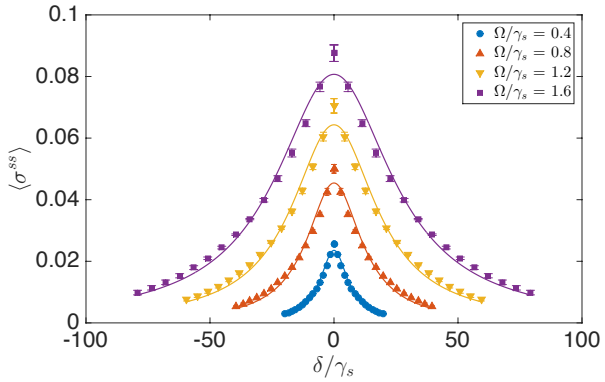

Figure 3.10: Examples of near-Lorentzian lineshapes from inhomogeneous rate equations at $n_{3D}C_3/\gamma_s = 5000$ for several Rabi frequencies. Error bars indicate standard error from five random distributions of atoms and the lines are best-fit Lorentzians.

the rate equations. Our choice of decoherence and atomic distribution provides a simple way of capturing these features and results in more accurate lineshapes.

In Fig. 3.10, we plot the resulting lineshapes for several different Rabi frequencies. We find that aside from the sharper behavior near resonance, the lineshapes appear to be quite Lorentzian, even at very large linewidths. Another simple choice of decoherence we might make is $\Gamma_i = \gamma_s + \gamma_R + C_3 \sum_{j\neq i} |V_{ij}| p_j$, which only allows decoherence from different sites to add constructively. The resulting lineshapes from this choice would be similar, but they would be more Lorentzian near resonance and drop off faster than a Lorentzian in the wings. Additionally, a steady state is present in all parameter regimes, in contrast to our choice of decoherence.

In Fig. 3.11, we compare the resonant population scaling behavior of the rate equation model to the scaling behavior observed experimentally. As before, we can relate the steady-state Rydberg population to the pumping rate via $\langle\sigma^{ss}\rangle \approx \frac{R_0}{\gamma'}$, where γ' corresponds to the total decay rate from the s state, including decay which takes the atom to an undriven ground state. Note that $\beta_3 = \sum |C_3^{(np)}| b_{np}/\Gamma_{np}$,

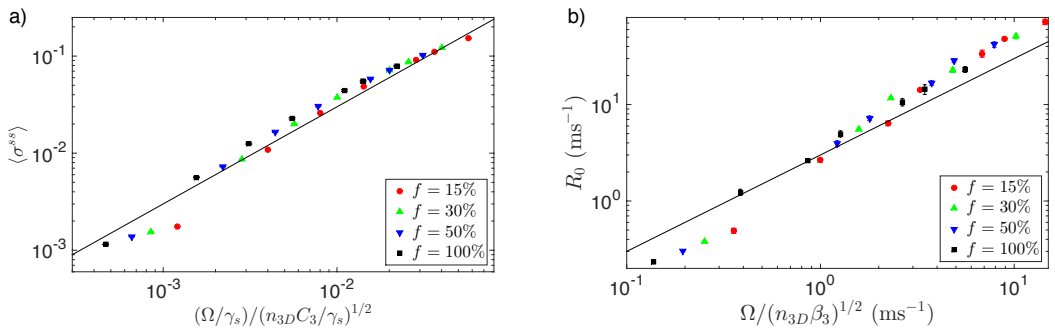

Figure 3.11: Resonant steady-state s population scaling as a function of Rabi frequency and interaction strength. Different points of the same color and symbol correspond to different Rabi frequencies and error bars represent one standard deviation from the Lorentzian fits. (a) Theoretical rate equation results, where $f = 100\%$ corresponds to $n_{3D}C_3/\gamma_s = 5000$. The solid line is a linear fit with a slope of 3. (b) Experimental resonant pumping rate results from Ref. [64] where $f = 100\%$ corresponds to $n_{3D}\beta_3 = 6612$. The solid line is a linear fit with a slope of 3. Note that our definition of Ω differs from the reference by a factor of two.

where $C_3^{(np)}$ is the corresponding value of C_3 for a p state times the root-mean-squared average of the angular dependence, b_{np} are the branching ratios from the driven s state to various p states, and Γ_{np} are their corresponding decay rates. This means that $n_{3D}\beta_3$ will be comparable to $n_{3D}C_3/\gamma_s$. Because γ' is the same order of magnitude as γ_s, we should expect similar dependence on Ω and $n_{3D}C_3$ or $n_{3D}\beta_3$ up to some constant factor. This is in fact the case, with the constant coefficient differing by less than a factor of two. Additionally, the change in behavior between smaller Rabi frequencies and larger Rabi frequencies is quantitatively similar as well, with both exhibiting a slight jump.

In Fig. 3.12, we compare the linewidth scaling behavior of our model to the scaling behavior observed experimentally. At the lowest Rabi frequencies, the linewidth approaches $1.3\gamma_s$, which is the bare linewidth due to γ_s and γ_R. Above these lower Rabi frequencies, we find that the general scaling behavior is again the

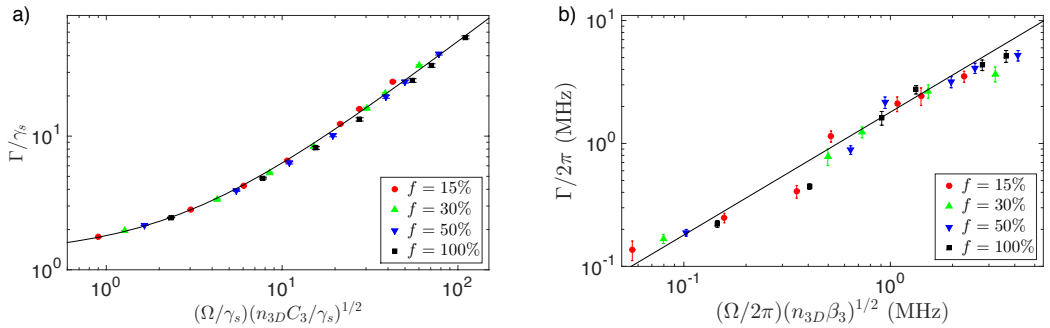

Figure 3.12: Steady-state linewidth scaling as a function of Rabi frequency and interaction strength. Different points of the same color and symbol correspond to different Rabi frequencies and error bars represent one standard deviation from the Lorentzian fits. (a) Theoretical rate equation results, where $f = 100\%$ corresponds to $n_{3\mathrm{D}}C_3/\gamma_s = 5000$. The solid line is a linear fit with a slope of .5 and y-intercept of 1.3 (the bare linewidth). (b) Experimental linewidth results from Ref. [64] where $f = 100\%$ corresponds to $n_{3\mathrm{D}}\beta_3 = 6612$. The solid line is a linear fit with a slope of 1.8. Note that our definition of Ω differs from the reference by a factor of two.

same for theory and experiment, differing only by a constant factor, which in this case is approximately four. While this is not as consistent as for the resonant scaling behavior, it is remarkably consistent considering the simplicity of our model.

Furthermore, we also consider how the scaling coefficients change as γ_p and γ_R are varied between $.4\gamma_s$ and $2\gamma_s$, which is comparable to the range possible for ^{87}Rb at $T = 300$ K. These scaling coefficients are plotted in Fig. 3.13. We find that the scaling coefficient for the resonant population and linewidth are approximately proportional to $\sqrt{\gamma_p/\gamma_R}$ and $\sqrt{\gamma_R/\gamma_p}$ respectively, which is consistent with the definition of β_3. This is natural since γ_p/γ_R corresponds to the ratio of s atoms to p atoms, so a higher ratio results in stronger dephasing in the same way that an increase in the interaction strength results in stronger dephasing. However, if we were to extend the range of possible γ_p and γ_R further, this behavior will eventually start to break down.

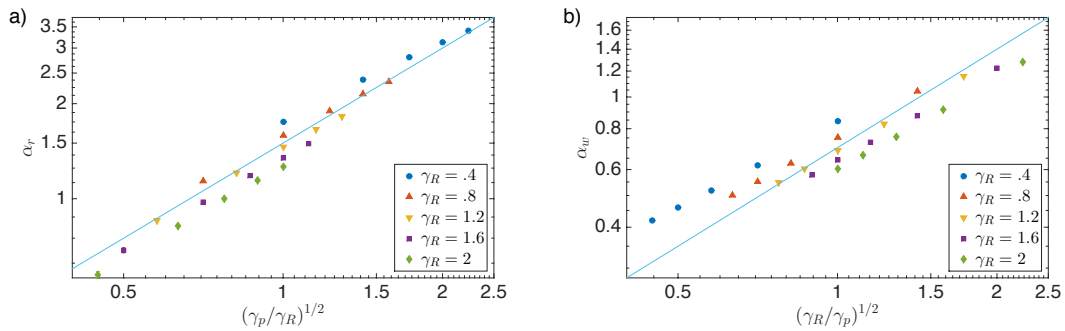

Figure 3.13: (a) Scaling coefficient for resonant population as a function of $(\gamma_p/\gamma_R)^{1/2}$. The coefficient α_r is extracted from fitting the resonant population according to $\langle\sigma^{ss}\rangle = \alpha_r(\Omega/\gamma_s)/(n_{3D}C_3/\gamma_s)^{1/2}$ for fixed γ_R, γ_p, where error bars correspond to one standard deviation from the fits. The solid line is a linear fit with a slope of 1.5. (b) Scaling coefficient for the widths as a function of $(\gamma_R/\gamma_p)^{1/2}$. The coefficient α_w is extracted from fitting the widths according to $\Gamma/\gamma_s = \alpha_w(\Omega/\gamma_s)(n_{3D}C_3/\gamma_s)^{1/2}$ for fixed γ_R, γ_p, where error bars (not visible) correspond to one standard deviation from the fits. The solid line is a linear fit with a slope of .7.

While the general scaling behavior of Ref. [64] is captured very well, there are two areas in which the rate equations fail qualitatively. The first qualitative failure is in the transition from quadratic to linear scaling in Rabi frequency. This model predicts the resonant linear behavior to continue into much smaller Rabi frequencies than observed experimentally in Fig. 3.8 (theory not shown). A possible reason for this is that at low Rabi frequencies, there is a small number of Rydberg atoms, so that the exact details of their interactions and correlations become more important and cannot be treated simply as dephasing. Another possible reason is that we have neglected van der Waals interactions, which may be more important in this regime. The second qualitative failure is the time required to reach steady state, which the model predicts to be much longer than observed experimentally, as noted for the homogeneous rate equations in Ref. [198]. This is most likely because the exact details of the interactions and correlations are more important when there is a

small number of Rydberg atoms. Rather than a diffuse population of p atoms slowly increasing the excitation rate, there is initially a single p atom which immediately brings directly into resonance many other possible excitations, leading to highly-correlated growth dynamics.

3.5 Conclusion and Outlook

We have investigated the effect that dissipation-induced dipole-dipole interactions have in a driven-dissipative Rydberg system using a cumulant expansion approach and phenomenological inhomogeneous rate equations. For the cumulant expansion approach, we showed that a modified many-body blockade radius picture arises, leading to steady-state populations which scale with the interaction strength like a power law. Additionally, we demonstrated a trend away from quadratic scaling in Rabi frequency at low Rabi frequencies for strong interactions. We theoretically predicted and experimentally observed that this transition occurs earliest for high densities. While the cumulant expansion behaves qualitatively similar to experimental observations, it is insufficient for quantitative agreement. This is because in spite of the large amount of dissipation, the strong, long-range nature of the dipole-dipole interaction gives rise to important many-body correlations which need to be taken into account. However, with a simple choice of phenomenological inhomogeneous rate equations in which decoherence is proportional to the interaction strength of nearby p atoms, we found remarkable quantitative agreement with the experimental results of Ref. [64], although the rate equations fail to properly capture

low Rabi frequency behavior and early time dynamics, where the actual structure of the correlations is particularly important.

In order to fully understand the underlying physics which gives rise to the anomalous Rydberg broadening, further theoretical and experimental study is necessary. While we have gone beyond mean field theory by including second-order connected correlations, there are other possible routes as well, such as Keldysh field theory [87, 99] or cluster mean-field approaches [216]. If one can determine which high-order correlations are likely to be important with a reasonable degree of accuracy, this could provide a better way to reduce the exponential number of equations of motion while still capturing the effects of high-order correlations. The success of our phenomenological rate equations may also provide insight into other systems involving dipole-dipole interactions or a path towards a more rigorous derivation of similar rate equations, as has been done for the case of diagonal interactions in Ref. [204]. Furthermore, the regimes where the rate equations performed poorly were where the Rydberg population was smaller, so they may be amenable to methods which take advantage of this. This regime is also where there is likely to be an interesting interplay between dipole-dipole interactions and van der Waals interactions, which we have neglected here. So far, both theory and experiment have been primarily focused on the effect of the interactions on the total Rydberg population, so determining the details of the many-body correlations theoretically and experimentally remains an interesting open problem.

Appendix A: Appendices to Chapter 2

A.1 Langevin Equations Near the Multicritical Points

In this section, we present the details of the derivation of the Langevin equations in the main text. To this end, we follow the procedure detailed in Ref. [82]. We begin by constructing the Keldysh path integral, then identify a semi-classical limit, and derive a pair of complex Langevin equations that describe the dynamics near the steady state. Finally, we identify a pair of two massless real fields (i.e., soft modes) and two massive real fields (i.e., fast modes). We adiabatically eliminate the massive fields to obtain a pair of Langevin equations presented in the main text.

We first ignore the sublattice symmetry for simplicity; this would not affect the analysis presented here. We shall return to the latter symmetry once we identify the semi-classical limit and corresponding Langevin equations. We cast our model in terms of a Keldysh path integral as

$$Z = \int \mathcal{D}[\psi_q, \psi_{cl}] e^{iS_K}, \tag{A.1}$$

where the action S_K is defined as

$$S_K = \int_{\mathbf{x},t} \psi_q^* \partial_t \psi_{cl} + \psi_q \partial_t \psi_{cl}^* - \int_{\mathbf{x},t} (H_n(\psi_{cl} + \psi_q) - H_n(\psi_{cl} - \psi_q)) \\ + i\Gamma \int_{\mathbf{x},t} (|\psi_q|^2 - \psi_{cl}\psi_q^*/2 - \psi_{cl}^*\psi_q/2), \quad \text{(A.2)}$$

with $\psi_{cl/q}$ the classical/quantum fields and $H_n(\psi)$ the normal-ordered form of the Hamiltonian. The third line corresponds to the particular case of the Lindblad operator $\sqrt{\Gamma}a$, although this approach may easily be extended to more general Lindbladians [99]. With the Hamiltonian in Eq. (2.1), the action in the continuum (with the nearest-neighbor interactions expanded in powers of the gradient) is given by

$$\begin{aligned} S_K = &\int_{\mathbf{x},t} \psi_q^* \left(i\partial_t + J\nabla^2 + \Delta + \mathfrak{z}J + i\frac{\Gamma}{2} \right) \psi_{cl} + c.c. \\ &- \int_{\mathbf{x},t} V|\psi_{cl}|^2(\nabla^2 + \mathfrak{z})\psi_{cl}\psi_q^* - \sqrt{2}\Omega\psi_q^* + c.c. \\ &+ \int_{\mathbf{x},t} i\Gamma|\psi_q|^2 - V|\psi_q|^2(\nabla^2 + \mathfrak{z})\psi_{cl}\psi_q^* + c.c., \end{aligned} \quad \text{(A.3)}$$

where $\mathfrak{z} = 2d$ is the coordination number. This expression bears a close resemblance to the action of Eq. (12) in Ref. [82], but they differ in the form of their interactions (which involve gradient terms here) and due to our use of normal ordering rather than the Weyl ordering of Ref. [82]. This motivates a similar rescaling of the parameters as

$$\begin{aligned} \Psi_{cl} = \psi_{cl}/\sqrt{\mathcal{N}}, \quad \Psi_q = \psi_q\sqrt{\mathcal{N}}, \\ \tilde{\Omega} = \Omega/\sqrt{\mathcal{N}}, \qquad v = \mathfrak{z}V\mathcal{N}. \end{aligned} \quad \text{(A.4)}$$

The parameter $\mathcal{N}$ effectively describes a density scale for the microscopic model via $|\psi_{cl}|^2 = \mathcal{N}|\Psi_{cl}|^2$, where $|\Psi_{cl}|^2$ is $\mathcal{O}(1)$. Since varying the density scale also modifies the interaction energy per particle, the interaction strength should be reduced cor-

respondingly such that $V|\psi_{cl}|^2 = v|\Psi_{cl}|^2$; similarly, the drive should be increased so that $\Omega\psi_q = \tilde{\Omega}\Psi_q$. We can then rewrite the action as

$$\begin{aligned} S_K = &\int_{\mathbf{x},t} \Psi_q^* \left(i\partial_t + J\nabla^2 + \Delta + \mathfrak{z}J + i\frac{\Gamma}{2} \right) \Psi_{cl} + c.c. \\ &- \int_{\mathbf{x},t} v|\Psi_{cl}|^2(\nabla^2/\mathfrak{z} + 1)\Psi_{cl}\Psi_q^* - \sqrt{2}\tilde{\Omega}\Psi_q^* + c.c. \\ &+ \int_{\mathbf{x},t} i\frac{\Gamma}{\mathcal{N}}|\Psi_q|^2 - \frac{v}{\mathcal{N}^2}|\Psi_q|^2(\nabla^2/\mathfrak{z} + 1)\Psi_{cl}\Psi_q^* + c.c. \end{aligned} \tag{A.5}$$

In the limit of large $\mathcal{N}$, the last term (the second term in the last line) can be dropped, leading to an action that is at most quadratic in Ψ_q. This is simply because a large population $\mathcal{N}$ corresponds to the semi-classical limit represented by a large classical field ψ_{cl} and small fluctuations due to the quantum field ψ_q. Using this fact, we can map the action to a Langevin equation as [128]

$$i\partial_t\Psi = -(J\nabla^2 + \Delta + \mathfrak{z}J + i\Gamma/2 - v(1 + \nabla^2/\mathfrak{z})|\Psi|^2)\Psi + \tilde{\Omega} + \xi, \tag{A.6a}$$

$$\langle \xi^*(\mathbf{x}, t)\xi(\mathbf{x}', t')\rangle = \frac{\Gamma}{\mathcal{N}}\delta(\mathbf{x} - \mathbf{x}')\delta(t - t'),\ \langle\xi\rangle = 0. \tag{A.6b}$$

Note that the noise level is further suppressed at larger $\mathcal{N}$ as should be expected from our semi-classical treatment.

Next we include the sublattice symmetry by defining Ψ_1 as the sublattice average and Ψ_2 as the sublattice difference of the field Ψ; see Eq. (2.15), which differs by a factor of $\sqrt{\mathcal{N}}$ due to our semi-classical limit. Our new Langevin equations are now

$$i\partial_t\Psi_1 = -(\Delta + J + i\Gamma/2)\Psi_1 + v(\Psi_1^2 - \Psi_2^2)\Psi_1^* + \tilde{\Omega} + \xi_1, \tag{A.7a}$$

$$i\partial_t\Psi_2 = -(\Delta - J + i\Gamma/2)\Psi_2 + v(\Psi_2^2 - \Psi_1^2)\Psi_2^* + \xi_2, \tag{A.7b}$$

$$\langle \xi_i^*(\mathbf{x}, t)\xi_j(\mathbf{x}', t')\rangle = \frac{\Gamma}{\mathcal{N}}\delta_{ij}\delta(\mathbf{x} - \mathbf{x}')\delta(t - t'),\ \langle\xi_i\rangle = 0. \tag{A.7c}$$

	κ_1	$\mathfrak{z}D_1$	h	r_1	A_{20}	A_{02}	A_{30}	A_{12}
$\Delta_c = 1/3$	$\frac{2v\Gamma}{3}$	$\frac{4\sqrt{3}}{9}$	$\frac{\delta_\Gamma}{\sqrt{6}} - \frac{2}{\sqrt{3}}\delta_{\tilde{\Omega}}$	$\frac{\delta_\Gamma}{2}$	$\frac{\sqrt{3}}{2}\delta_{\tilde{\Omega}} - \frac{\sqrt{6}}{4}\delta_\Gamma$	$\frac{2\sqrt{2}}{9}$	$-\frac{1}{\sqrt{3}}$	$-\frac{7}{9\sqrt{3}}$
$\Delta_c = 2/3$	$\frac{2v\Gamma}{3}$	$\frac{\sqrt{3}}{3}$	$\frac{\delta_\Gamma}{\sqrt{6}} - \frac{2}{\sqrt{3}}\delta_{\tilde{\Omega}}$	$\frac{\delta_\Gamma}{2}$	$\frac{\sqrt{3}}{2}\delta_{\tilde{\Omega}} - \frac{\sqrt{6}}{4}\delta_\Gamma$	$\frac{\sqrt{2}}{9}$	$-\frac{1}{\sqrt{3}}$	$-\frac{5}{9\sqrt{3}}$

(a)

	κ_2	$\mathfrak{z}D_2$	r_2	B_{11}	B_{03}	B_{21}
$\Delta_c = 1/3$	$2v\Gamma$	$\frac{4\sqrt{3}}{9}$	$\frac{2\sqrt{3}}{3}\delta_\Delta + \frac{5}{6}\delta_\Gamma - \frac{\sqrt{2}}{3}\delta_{\tilde{\Omega}}$	$-\frac{2\sqrt{2}}{3}$	$-\frac{5}{9\sqrt{3}}$	$-\frac{1}{3\sqrt{3}}$
$\Delta_c = 2/3$	$2v\Gamma$	$\frac{\sqrt{3}}{3}$	$\frac{2\sqrt{3}}{3}\delta_\Delta + \frac{5}{6}\delta_\Gamma - \frac{\sqrt{2}}{3}\delta_{\tilde{\Omega}}$	$-\frac{2\sqrt{2}}{3}$	$-\frac{1}{9\sqrt{3}}$	$-\frac{1}{3\sqrt{3}}$

(b)

Table A.1: Langevin equation parameters for soft modes (a) ϕ_1 and (b) ϕ_2 in Eq. (A.12).

Notice that we have dropped all the gradient terms as they do not play a role in identifying the massive fields and their adiabatic elimination. We also follow our convention in the main text to set $\mathfrak{z}J \to J$.

Our model exhibits two multicritical points where two modes (each a component of one of the two fields Ψ_i) become critical. Due to the sublattice symmetry, $\Psi_2 = 0$ at the multicritical points up to fluctuations. Working in units where $\Delta + J = 1$, the two multicritical points occur at

$$\begin{aligned} (\Delta_c, J_c) &= \left(\frac{1}{3}, \frac{2}{3}\right), \left(\frac{2}{3}, \frac{1}{3}\right), \\ \Gamma_c &= \sqrt{4/3}, \quad \tilde{\Omega}_c = (2/3)^{3/2}/\sqrt{v}, \end{aligned} \tag{A.8}$$

with $\Psi_1 = \Psi_c = \sqrt{2/3v}e^{-i\pi/3}$.

Next, we expand the Langevin equations in the vicinity of the two multicritical

points as

$$\begin{aligned} \Delta = \Delta_c + \delta_\Delta, \qquad & J_c = J_c - \delta_\Delta, \\ \Gamma = \Gamma_c + \delta_\Gamma, \quad & \tilde{\Omega} = \tilde{\Omega}_c + \delta_{\tilde{\Omega}}/\sqrt{v}, \\ \Psi_1 = \Psi_c + \psi_1/\sqrt{v}, \qquad & \Psi_2 = \psi_2/\sqrt{v}. \end{aligned} \tag{A.9}$$

The soft and gapped modes can be determined as linear combinations of the real and imaginary parts of the two fields ψ_1, ψ_2. As in the case of bistability, the first pair is identified as [82]

$$\psi_1 = \phi_1' + e^{i\pi/3}\phi_1, \tag{A.10}$$

where ϕ_1' is massive and relaxes quickly while ϕ_1 defines the slow field. Identifying the massive/massless components of the field ψ_2 depends on the corresponding multicritical point as

$$\begin{aligned} \Delta_c = 1/3: \quad \psi_2 &= \frac{1}{\sqrt{3}}(\phi_2 e^{-i\pi/6} + \phi_2' e^{i\pi/6}), \\ \Delta_c = 2/3: \qquad \psi_2 &= \frac{1}{\sqrt{3}}(\phi_2 + \phi_2' e^{i\pi/3}), \end{aligned} \tag{A.11}$$

where again the primed (unprimed) field indicates the massive (massless) field. Note that these differ from the main text by a factor of $\sqrt{V}$, which is done to simplify the resulting parameters in the Langevin equations by moving all the V dependence to the noise term.

Upon adiabatically eliminating the massive fields and restoring the gradient terms, we arrive at the Langevin equations

$$\dot{\phi_1} = \; h - r_1\phi_1 + D_1\nabla^2\phi_1 + \xi_1 + A_{20}\phi_1^2 + A_{02}\phi_2^2 + A_{12}\phi_1\phi_2^2 + A_{30}\phi_1^3, \tag{A.12a}$$

$$\dot{\phi_2} = -r_2\phi_2 + D_2\nabla^2\phi_2 + \xi_2 + B_{11}\phi_1\phi_2 + B_{21}\phi_1^2\phi_2 + B_{03}\phi_2^3, \tag{A.12b}$$

with Gaussian noise

$$\langle \xi_i(\mathbf{x},t)\xi_j(\mathbf{x}',t')\rangle = 2\frac{\kappa_i}{\mathcal{N}}\delta_{ij}\delta(\mathbf{x}-\mathbf{x}')\delta(t-t'). \tag{A.13}$$

The various numerical factors are summarized in Table A.1 for the two multicritical points under consideration. Note that $\gamma_i = 1$ and $T_i = \kappa_i/\mathcal{N}$. We can see at this point that the opposite signs of A_{02} and B_{11} indicate that no Hamiltonian description is possible. Indeed, as will be discussed in the following section, this will carry over to the signs of g_{12} and g_{21}, leading to the critical behavior defined by the NEFPs.

A.2 Redundant Operators

In this section, we identify the redundant operators in the Langevin equations (A.12). In general, this can be done at the level of the Schwinger-Keldysh action; however, we shall focus on the equivalent description in terms of the Langevin equations. This perspective is particularly suitable in dealing with the (Itô) regularization that is required to properly define the stochastic equations.

Consider a pair of Langevin equations that define an *Itô process* in the differential form [217]

$$d\phi_1 = f_1(\phi_1,\phi_2)dt + \sqrt{\kappa_1}dW_1, \tag{A.14a}$$

$$d\phi_2 = f_2(\phi_1,\phi_2)dt + \sqrt{\kappa_2}dW_2, \tag{A.14b}$$

where dW_i is the stochastic noise that obeys the Itô rules:

$$dW_i dW_j = \delta_{ij}dt, \tag{A.15a}$$

$$dW_i dt = dt dW_i = 0, \tag{A.15b}$$

$$dt^2 = 0. \tag{A.15c}$$

At the multicritical point, where the effective masses and the magnetic field are set to zero, the Langevin equations (A.12) can be written in the form of Eq. (A.14) with

$$f_1(\phi_1, \phi_2) = D_1 \nabla^2 \phi_1 + A_{20}\phi_1^2 + A_{02}\phi_2^2 + A_{12}\phi_1\phi_2^2 + A_{30}\phi_1^3, \tag{A.16a}$$

$$f_2(\phi_1, \phi_2) = D_2 \nabla^2 \phi_2 + B_{11}\phi_1\phi_2 + B_{21}\phi_1^2\phi_2 + B_{03}\phi_2^3. \tag{A.16b}$$

In order to identify the redundant operators, we should examine the Langevin equations under a general change of the field variables. We should then find the dynamics in terms of new variables defined as $\Phi_1 = g_1(\phi_1, \phi_2)$ and $\Phi_2 = g_2(\phi_1, \phi_2)$; the functions g_i are general (but local) nonlinear maps which are invertible in a neighborhood around the multicritical point and preserve the sublattice symmetry $\phi_2 \to -\phi_2$. The equations governing the dynamics of the new variables take the form

$$\begin{aligned} d\Phi_1 &= \frac{\partial g_1}{\partial \phi_1} d\phi_1 + \frac{\partial g_1}{\partial \phi_2} d\phi_2 + \frac{1}{2}\frac{\partial^2 g_1}{\partial \phi_1^2} d\phi_1^2 + \frac{1}{2}\frac{\partial^2 g_1}{\partial \phi_2^2} d\phi_2^2 + \frac{\partial g_1}{\partial \phi_1 \partial \phi_2} d\phi_1 d\phi_2 \\ &= \left(f_1 \frac{\partial g_1}{\partial \phi_1} + f_2 \frac{\partial g_1}{\partial \phi_2} + \frac{\kappa_1}{2}\frac{\partial^2 g_1}{\partial \phi_1^2} + \frac{\kappa_2}{2}\frac{\partial^2 g_1}{\partial \phi_2^2} \right) dt + \sqrt{\kappa_1}\frac{\partial g_1}{\partial \phi_1} dW_1 + \sqrt{\kappa_2}\frac{\partial g_1}{\partial \phi_2} dW_2. \end{aligned} \tag{A.17}$$

We have used the Itô rules to derive the above equation, which is known as Itô's formula or Itô's lemma [217]. A similar stochastic equation can be derived for Φ_2 by switching $1 \leftrightarrow 2$. Note that the terms on the rhs should be expressed in terms of Φ_i through the inverse functions g_i^{-1}. One notices that there are new contributions to the deterministic dynamics due to the noise. However, since we

are working under the assumption that the noise is parametrically small compared to the deterministic terms (with a strength proportional to $1/\mathcal{N}$), we can ignore such terms. Additionally, the noise terms are no longer additive but are instead multiplicative, which introduces new terms in the action. However, since $\kappa_i \neq 0$, the latter are irrelevant in the sense of RG and can be neglected as well. The same holds for nonlinear terms (beyond quadratic terms) that involve gradients.

We shall assume without loss of generality that

$$\left.\frac{\partial g_i}{\partial \phi_j}\right|_{\phi_i,\phi_j=0} = \delta_{ij}; \tag{A.18}$$

rescaling the fields by a constant factor does not allow us any additional freedom while rotations obscure the symmetry $\phi_2 \to -\phi_2$. Additionally, we do not consider a constant shift in the field ϕ_1 (a shift in ϕ_2 is disallowed due to symmetry) for now, but discuss it separately later in this section. Based on the structure of Eq. (A.17), we notice that the quadratic terms in f_i and g_i result in additional cubic terms. All other new terms in the deterministic part of the dynamics involve fourth- or higher-order terms which are irrelevant under RG. Expressing a general nonlinear transformation as

$$g_1(\phi_1, \phi_2) = \phi_1 + c_{20}\phi_1^2 + c_{02}\phi_2^2, \tag{A.19a}$$

$$g_2(\phi_1, \phi_2) = \phi_2 + c_{11}\phi_1\phi_2, \tag{A.19b}$$

the modification of the cubic terms to lowest order in the coefficients and interaction

terms are given by

$$\begin{pmatrix} A_{12} \\ B_{21} \\ B_{03} \end{pmatrix} \to \begin{pmatrix} A_{12} \\ B_{21} \\ B_{03} \end{pmatrix} + \mathbf{M} \begin{pmatrix} c_{20} \\ c_{02} \\ c_{11} \end{pmatrix}, \tag{A.20}$$

where the matrix $\mathbf{M}$ is given by

$$\mathbf{M} = \begin{pmatrix} 2A_{02} & 2B_{11} - 2A_{20} & -2A_{02} \\ -B_{11} & 0 & A_{20} \\ 0 & -B_{11} & A_{02} \end{pmatrix}. \tag{A.21}$$

Notice that the coefficient A_{30} is left unchanged. The rank of matrix $\mathbf{M}$ is 2, which then determines the number of corresponding redundant operators.

In addition to the two redundant operators above, a third one emerges due to a constant shift $\phi_1 \to \phi_1 + c_{00}$. Under this transformation, the quadratic terms transform as

$$\begin{pmatrix} A_{20} \\ A_{02} \\ B_{11} \end{pmatrix} \to \begin{pmatrix} A_{20} \\ A_{02} \\ B_{11} \end{pmatrix} + \begin{pmatrix} 3A_{30} \\ A_{12} \\ 4A_{21} \end{pmatrix} c_{00}. \tag{A.22}$$

The effective mass and magnetic field terms also change, but this simply shifts the location of the critical point.

The three redundant operators derived here can be used to always set the terms A_{20}, A_{02}, B_{11} to zero. This can be understood by noting that the transformation corresponding to $\mathbf{M}$ allows one to adjust the ratios of A_{12} and A_{21} relative to A_{30} without changing the quadratic terms. By properly using this redundancy, these ratios can be tuned until the constant shift in Eq. (A.22) shifts all three quadratic

terms to zero. At the same time, the cubic terms transform as

$$A_{30} \to A_{30}, \tag{A.23a}$$

$$B_{03} \to B_{03} - \frac{A_{12}A_{20}B_{11} - 6A_{02}A_{30}B_{11} + 2A_{02}A_{20}B_{21}}{2A_{20}(A_{20} - B_{11})}, \tag{A.23b}$$

$$A_{12} \to 2A_{02}\frac{3A_{30}}{2A_{20}}, \tag{A.23c}$$

$$B_{21} \to B_{11}\frac{3A_{30}}{2A_{20}}. \tag{A.23d}$$

Having exhausted the three redundant operators to remove the three quadratic terms, there is no further freedom in tuning other terms and, specifically, all the cubic terms are fixed. While we could in principle include cubic or higher-order terms in the nonlinear transformation [Eq. (A.19)], these would only modify the fourth- or higher-order terms which are irrelevant under RG due to the presence of the cubic terms. We also see that the relative sign of A_{12} and B_{21} is indeed directly determined by the relative sign of A_{02} and B_{11}, leading to criticality described by the NEFPs. Finally, we note that the coefficient A_{20} appears in the denominator of the above transformations. We assumed that this term is generated under coarse-graining and thus should pose no problem in making the above transformations. However, if there is a mechanism where this coefficient could be tuned to zero, the above transformations are no longer valid and the two nonzero cubic terms should be kept.

A.3 Perturbative RG

In this section, we discuss the details of the calculations in our perturbative RG analysis. In the first part, we introduce the diagrammatic techniques we have

(a) (b)

Figure A.1: Diagrammatic representation of Gaussian propagators. Solid (dotted) lines correspond to classical (response) fields. The two fields are later distinguished by thickness and color. In this figure, we have shown (a) the response propagator, and (b) the correlation propagator.

used in the main text. In the second part, we compute the one-loop diagrams, while, in the third part, we compute the two-loop diagrams for terms which are unrenormalized at one loop.

A.3.1 Diagrammatic Techniques

To define the Gaussian propagators, we start with the Gaussian model with the corresponding action

$$\mathcal{A}_0[\tilde{\phi}_i, \phi_i] = \sum_i \int_{t,\mathbf{x}} \tilde{\phi}_i(\gamma_i \partial_t - D_i \nabla^2 + r_i)\phi_i - \gamma_i T_i \tilde{\phi}_i^{\,2}. \tag{A.24}$$

The Gaussian response and correlation functions are then given by

$$\chi_0^i(\mathbf{q}, \omega) = \mathcal{F}\langle \tilde{\phi}_i(\mathbf{0}, 0)\phi_i(\mathbf{r}, t)\rangle = \frac{1}{-i\gamma_i\omega + D_i\mathbf{q}^2 + r_i}, \tag{A.25a}$$

$$C_0^i(\mathbf{q}, \omega) = \mathcal{F}\langle \phi_i(\mathbf{0}, 0)\phi_i(\mathbf{r}, t)\rangle = \frac{2\gamma_i T_i}{\gamma_i^2\omega^2 + (D_i\mathbf{q}^2 + r_i)^2}, \tag{A.25b}$$

where $\mathcal{F}$ denotes the Fourier transform in both space and time. These propagators can be expressed in a diagrammatic representation as shown in Fig. A.1.

The four interaction vertices from Eq. (2.27b) are illustrated in Fig. A.2. Due to the structure of the action, one can find the corresponding Z factors for ϕ_2 by switching the subscripts $1 \leftrightarrow 2$ and multiplying u_{12} by a factor of σ.

(a) (b) (c) (d)

Figure A.2: Interaction vertices. Thin black (thick cyan) lines correspond to the first (second) field and solid (dashed) lines correspond to the classical (response) field. (a) $u_1\phi_1^3\tilde{\phi}_1$. (b) $u_2\phi_2^3\tilde{\phi}_2$. (c) $u_{12}\phi_2^2\phi_1\tilde{\phi}_1$. (d) $\sigma u_{12}\phi_1^2\phi_2\tilde{\phi}_2$.

Finally, we quote identities which will prove useful in computing the integrals in various Feynman diagrams:

$$\frac{1}{A^r B^s} = \frac{\Gamma(r+s)}{\Gamma(r)\Gamma(s)} \int_0^1 \frac{x^{r-1}(1-x)^{s-1}}{[xA+(1-x)B]^{r+s}} dx, \tag{A.26a}$$

$$\int \frac{d^d\mathbf{p}}{(2\pi)^d} \frac{1}{(m^2 + 2\mathbf{q}\cdot\mathbf{p} + D\mathbf{p}^2)^s} = \frac{\Gamma(s-d/2)}{(4\pi)^{d/2}\Gamma(s)} \frac{D^{-d/2}}{(m^2 - \mathbf{q}^2/D)^{s-d/2}}, \tag{A.26b}$$

where $\Gamma(x)$ is Euler's Gamma function. Finally, in order to determine the Z factors, we employ the minimal subtraction procedure. This means that only the ultraviolet divergences, in the form of powers of $1/\epsilon$, are incorporated into the Z factors. For simplicity, we only present these divergences in the evaluation of integrals in the following sections; non-divergent terms are dropped.

A.3.2 One-Loop Diagrams

A.3.2.1 Mass Terms

In this section, we consider corrections to r_1. The corrections to r_2 can be obtained by switching the roles of ϕ_1 and ϕ_2. There are two diagrams that provide corrections, which are illustrated in Fig. A.3. The combinatorial and interaction factors are (a) $3\times u_1$ and (b) u_{12}. Thus the one-loop contribution to the renormalization

(a) (b)

Figure A.3: One-loop corrections to $r_1\phi_1\tilde{\phi}_1$. Analogous diagrams for $\phi_2\tilde{\phi}_2$ can be obtained by switching thin black and thick cyan lines.

of r_1 is

$$\int \frac{d^d\mathbf{p}}{(2\pi)^d}\int \frac{d\omega}{2\pi}\left[3u_1 C_0^1(\mathbf{p},\omega)+u_{12}C_0^2(\mathbf{p},\omega)\right], \tag{A.27}$$

so we should evaluate the integral of C_0^i. The latter can be written as

$$\begin{aligned} &2\gamma_i T_i\int \frac{d^d\mathbf{p}}{(2\pi)^d}\int \frac{d\omega}{2\pi}\frac{1}{\gamma_i^2\omega^2+(D_i\mathbf{p}^2+r_i)^2}\\ =&T_i\int \frac{d^d\mathbf{p}}{(2\pi)^d}\frac{1}{D_i\mathbf{p}^2+r_i}, \end{aligned} \tag{A.28}$$

where the last line follows once we integrate over frequency.

The phase transition occurs where the renormalized mass term vanishes. The critical value of the mass parameter r_{i_c} is then determined by

$$r_{1_c}=-3u_1T_1\int \frac{d^d\mathbf{p}}{(2\pi)^d}\frac{1}{D_1\mathbf{p}^2}-u_{12}T_2\int \frac{d^d\mathbf{p}}{(2\pi)^d}\frac{1}{D_2\mathbf{p}^2}, \tag{A.29}$$

and similarly for r_{2_c}; note that the factors of r in the denominator have been dropped as they introduce $O(u^2)$ corrections. Defining an additive renormalized mass term $\overline{r}_i=r_i-r_{i_c}$, we can determine the Z factors for $\overline{r}_i$. To this end, we need to compute integrals of the form

$$\int \frac{d^d\mathbf{p}}{(2\pi)^d}\frac{\overline{r}_i}{D_i\mathbf{p}^2(D_i\mathbf{p}^2+\overline{r}_i)}=\frac{A_d\mu^{-\epsilon}}{\epsilon}\frac{\overline{r}_i}{D_i^2}, \tag{A.30}$$

where we have included the geometrical factor A_d. We can then compute the corre-

sponding Z factors as

$$Z_{\bar{r}_1} = 1 - 3u_1 \frac{A_d \mu^{-\epsilon}}{\epsilon} \frac{T_1}{D_1^2} - u_{12} \frac{A_d \mu^{-\epsilon}}{\epsilon} \frac{T_2}{D_2^2} \frac{\bar{r}_2}{\bar{r}_1}, \tag{A.31a}$$

$$Z_{\bar{r}_2} = 1 - 3u_2 \frac{A_d \mu^{-\epsilon}}{\epsilon} \frac{T_2}{D_2^2} - \sigma u_{12} \frac{A_d \mu^{-\epsilon}}{\epsilon} \frac{T_1}{D_1^2} \frac{\bar{r}_1}{\bar{r}_2}. \tag{A.31b}$$

From this point on, we simply write $\bar{r}_i$ as r_i.

A.3.2.2 Coupling Terms

We first consider one-loop corrections to u_1. We need to consider two diagrams as illustrated in Fig. A.4. The combinatorial and interaction factors are (a) $-3 \times 2 \times 3 \times u_1^2$ and (b) $-2 \times \sigma u_{12}^2$. Thus the one-loop contribution to the renormalization of u_1 is

$$-\int \frac{d\mathbf{p}}{(2\pi)^d} \int \frac{d\omega}{2\pi} \left[18 u_1^2 \chi_0^1(\mathbf{p}, \omega) C_0^1(-\mathbf{p}, -\omega) \right. \tag{A.32}$$

$$\left. + 2\sigma u_{12}^2 \chi_0^2(\mathbf{p}, \omega) C_0^2(-\mathbf{p}, -\omega) \right], \tag{A.33}$$

whose evaluation we shall put aside for the moment.

The renormalization of u_{12} involves eight diagrams, four of which are illustrated in Fig. A.5 and renormalize $u_{12}\phi_2^2\phi_1\tilde{\phi}_1$. The combinatorial and interaction factors are (a) $-2 \times 2 \times u_{12}^2$, (b) $-2 \times 2 \times \sigma u_{12}^2$, (c) $-2 \times 3 \times u_2 \times \sigma u_{12}$, and (d) $-3 \times 2 \times u_1 \times u_{12}$. The remaining four diagrams, corresponding to the renormalization of $\sigma u_{12}\phi_1^2\phi_2\tilde{\phi}_2$, can be simply obtained by interchanging the two fields. The resulting set of internal diagrams and combinatorial factors are the same up to a factor of σ, so $\phi_2^2\phi_1\tilde{\phi}_1$ and $\phi_1^2\phi_2\tilde{\phi}_2$ are renormalized in the same way at this order. Indeed, this reflects the fact fact that g_{12}/g_{21} is not renormalized at the one-loop order.

(a) (b)

Figure A.4: One-loop corrections to $u_1\phi_1^3\tilde{\phi}_1$. Analogous diagrams for $\phi_2^3\tilde{\phi}_2$ can be obtained by switching thin black and thick cyan lines.

(a) (b)

(c) (d)

Figure A.5: One-loop corrections to $u_{12}\phi_2^2\phi_1\tilde{\phi}_1$. Analogous diagrams for $\sigma u_{12}\phi_1^2\phi_2\tilde{\phi}_2$ can be obtained by switching thin black and thick cyan lines.

Thus the one-loop contribution to the renormalization of u_{12} is

$$-\int \frac{d\mathbf{p}}{(2\pi)^d}\int \frac{d\omega}{2\pi}\left[4u_{12}^2\chi_0^1(\mathbf{p},\omega)C_0^2(-\mathbf{p},-\omega)+4\sigma u_{12}^2\chi_0^2(\mathbf{p},\omega)C_0^1(-\mathbf{p},-\omega)\right.$$
$$\left.+6\sigma u_1 u_{12}\chi_0^2(\mathbf{p},\omega)C_0^2(-\mathbf{p},-\omega)+6u_2u_{12}\chi_0^1(\mathbf{p},\omega)C_0^1(-\mathbf{p},-\omega)\right]. \quad \text{(A.34)}$$

This expression involves a nontrivial integral of the form

$$U_{ij} = -\int \frac{d\mathbf{p}}{(2\pi)^d}\int \frac{d\omega}{2\pi}\chi_0^i(\mathbf{p},\omega)C_0^j(-\mathbf{p},-\omega)$$
$$= -\int \frac{d\mathbf{p}}{(2\pi)^d}\int \frac{d\omega}{2\pi}\frac{1}{-i\gamma_i\omega+D_i\mathbf{p}^2+r_i}\frac{2\gamma_jT_j}{\gamma_j^2\omega^2+(D_j\mathbf{p}^2+r_j)^2}. \quad \text{(A.35)}$$

Integrating out frequency, the latter integral becomes

$$-\frac{T_j}{\gamma_i\gamma_j}\int \frac{d\mathbf{p}}{(2\pi)^d}\frac{1}{(\tilde{D}_j\mathbf{p}^2+\tilde{r}_j)((\tilde{D}_i+\tilde{D}_j)\mathbf{p}^2+\gamma_j\tilde{r}_i+\gamma_i\tilde{r}_j)}, \quad \text{(A.36)}$$

where $D_i = \gamma_i\tilde{D}_i$ and $r_i = \gamma_i\tilde{r}_i$. Using Feynman's parametrization, this may be

rewritten

$$-\frac{T_j}{\gamma_i\gamma_j}\int\frac{d\mathbf{p}}{(2\pi)^d}\int_0^1 dx\frac{1}{[(1-x)(\tilde{D}_j\mathbf{p}^2+\tilde{r}_j)+x(\tilde{D}_i+\tilde{D}_j)\mathbf{p}^2+x\tilde{r}_i+x\tilde{r}_j]^2}, \quad \text{(A.37)}$$

allowing us to integrate over momentum to find

$$-\frac{T_j}{\gamma_i}\frac{\Gamma(2-d/2)}{(4\pi)^{d/2}}\int_0^1 dx\frac{(\tilde{D}_j+\tilde{D}_i x)^{-d/2}}{(\tilde{r}_j+\tilde{r}_i x)^{2-d/2}}. \quad \text{(A.38)}$$

Noting that $\tilde{r}_i = \mu^2\tilde{r}_{i_R} + \mathcal{O}(u)$ and $\tilde{r}_{i_R}$ is a finite constant, then according to the minimal subtraction procedure, $(\tilde{r}_j+\tilde{r}_i x)^{2-d/2} \approx \mu^{-\epsilon}(\tilde{r}_{j_R}+\tilde{r}_{i_R}x)^0 = \mu^{-\epsilon}$, where ϵ has been set to 0 in the non-divergent part to extract the residue of the pole. Similarly, we expand $\Gamma(2-d/2) = 2/\epsilon + \mathcal{O}(1)$ to extract the pole. Thus the above integral becomes

$$U_{ij} = -\frac{T_j}{\gamma_i\gamma_j}\frac{1}{\tilde{D}_j(\tilde{D}_i+\tilde{D}_j)}\frac{A_d\mu^{-\epsilon}}{\epsilon}, \quad \text{(A.39)}$$

where we have included the geometrical factor A_d. This result in combination with the diagrams considered above results in the following Z factors

$$Z_{u_1} = 1 + 18U_{11}u_1 + 2U_{22}\sigma u_{12}^2/u_1, \quad \text{(A.40a)}$$

$$Z_{u_2} = 1 + 18U_{22}u_2 + 2U_{11}\sigma u_{12}^2/u_2, \quad \text{(A.40b)}$$

$$Z_{u_{12}} = 1 + 4U_{21}u_{12} + 4U_{12}\sigma u_{12} + 6U_{11}u_1 + 6U_{22}\sigma u_2. \quad \text{(A.40c)}$$

A.3.3 Two-Loop Diagrams

First, we consider the two-loop corrections which arise from the $\tilde{\phi}_i\phi_i$ terms. There are three two-loop diagrams that renormalize γ_1 and D_1 as shown in Fig. A.6. The corresponding combinatorial and interaction factors are (a) $-\frac{2!}{2!}\times 3\times 2\times 3\times u_1^2$, (b) $-\frac{2!}{2!}\times 2\times u_{12}^2$, and (c) $-2\times 2\times\sigma u_{12}^2$.

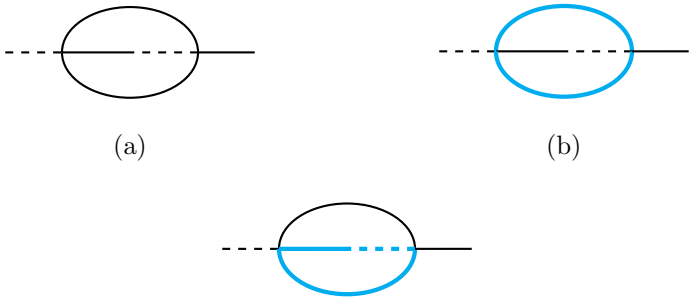

(a) (b) (c)

Figure A.6: Two-loop corrections to γ_1 and D_1. Analogous diagrams for γ_2, D_2 can be obtained by switching thin black and thick cyan lines.

As in the case of the coupling terms, the internal diagrams are all of the same form, so we consider a generic internal diagram in the form of Fig. A.7.

This diagram corresponds to the integral

$$I_{ij}^k = \int \frac{d^d\mathbf{p}d^d\mathbf{q}}{(2\pi)^{2d}} \int \frac{d\omega_1 d\omega_2}{(2\pi)^2} \chi_0^k(\mathbf{k}-\mathbf{p}-\mathbf{q}, \omega-\omega_1-\omega_2) C_0^i(\mathbf{p},\omega_1) C_0^j(\mathbf{q},\omega_2), \quad \text{(A.41)}$$

or

$$\int \frac{d^d\mathbf{p}d^d\mathbf{q}}{(2\pi)^{2d}} \int \frac{d\omega_1 d\omega_2}{(2\pi)^2} \frac{4\gamma_i\gamma_j T_i T_j}{[(D_i\mathbf{p}^2+r_i)^2+\gamma_i^2\omega_1^2][(D_j\mathbf{q}^2+r_j)^2+\gamma_j^2\omega_2^2]} \times \frac{1}{-i\gamma_k(\omega-\omega_1-\omega_2)+D_k(\mathbf{k}-\mathbf{p}-\mathbf{q})^2+r_k} \quad \text{(A.42)}$$

Integrating out the frequencies, this becomes

$$\frac{T_iT_j}{\gamma_i\gamma_j\gamma_k} \int \frac{d^d\mathbf{p}d^d\mathbf{q}}{(2\pi)^{2d}} \frac{2}{(\tilde{D}_i\mathbf{p}^2+\tilde{r}_i)(\tilde{D}_j\mathbf{q}^2+\tilde{r}_j)} \times \frac{1}{\tilde{D}_i\mathbf{p}^2+\tilde{D}_j\mathbf{q}^2+\tilde{D}_k(\mathbf{k}-\mathbf{p}-\mathbf{q})^2+\tilde{r}_i+\tilde{r}_j+\tilde{r}_k-i\omega}. \quad \text{(A.43)}$$

Once more, we use Feynman parameters to integrate over momenta, first combining the second two factors in the denominator as

$$\frac{T_iT_j}{\gamma_i\gamma_j\gamma_k} \int \frac{d\mathbf{p}}{(2\pi)^d} \frac{1}{\tilde{D}_i\mathbf{p}^2+\tilde{r}_i} \int_0^1 dx \int \frac{d\mathbf{q}}{(2\pi)^d} \frac{1}{(\alpha_0+2\boldsymbol{\alpha}_1\cdot\mathbf{q}+\alpha_2\mathbf{q}^2)^2}, \quad \text{(A.44)}$$

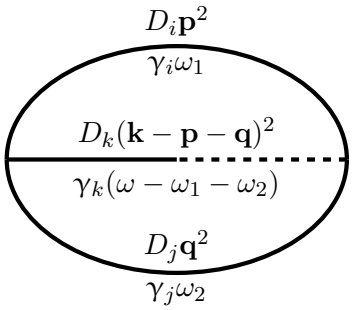

Figure A.7: A generic internal two-loop diagram leading to a renormalization of $\boldsymbol{\gamma}_i$ and D_i.

where

$$\alpha_0 = \tilde{r}_j(1-x) + x(\tilde{D}_j\mathbf{q}^2 + \tilde{D}_k(\mathbf{k}-\mathbf{q})^2 + \tilde{r}_i + \tilde{r}_j + \tilde{r}_k - i\omega), \tag{A.45a}$$

$$\boldsymbol{\alpha}_1 = x\tilde{D}_k(\mathbf{p}-\mathbf{k}), \tag{A.45b}$$

$$\alpha_2 = \tilde{D}_i + x\tilde{D}_k. \tag{A.45c}$$

Integrate over $\mathbf{q}$ yields

$$\frac{T_iT_j}{\boldsymbol{\gamma}_i\boldsymbol{\gamma}_j\boldsymbol{\gamma}_k}\frac{\Gamma(2-d/2)}{(4\pi)^{d/2}}\int_0^1 dx\int\frac{d^d\mathbf{p}}{(2\pi)^d}\frac{1}{(\tilde{D}_i\mathbf{p}^2+\tilde{r}_i)}\frac{\alpha_2^{-d/2}}{(\alpha_0-\boldsymbol{\alpha}_1^2/\alpha_2)^{2-d/2}}. \tag{A.46}$$

Again taking advantage of a second Feynman parameter, we write this as

$$\frac{T_iT_j}{\boldsymbol{\gamma}_i\boldsymbol{\gamma}_j\boldsymbol{\gamma}_k}\frac{\Gamma(2-d/2)}{(4\pi)^{d/2}}\frac{\Gamma(3-d/2)}{\Gamma(2-d/2)}\int_0^1\int_0^1 dxdy\int\frac{d^d\mathbf{p}}{(2\pi)^d}\frac{\alpha_2^{-d/2}y^{1-d/2}}{(\beta_0+2\boldsymbol{\beta}_1\cdot\mathbf{p}+\beta_2\mathbf{p}^2)^{3-d/2}}, \tag{A.47}$$

where

$$\beta_0 = (1-y)\tilde{r}_i + y(\tilde{r}_j + x\tilde{D}_k)\mathbf{k}^2 + \tilde{r}_kx + \tilde{r}_ix - ix\omega - \frac{x^2\tilde{D}_k^2\mathbf{k}^2}{\tilde{D}_j+x\tilde{D}_k}, \tag{A.48a}$$

$$\boldsymbol{\beta}_1 = \frac{-xy\tilde{D}_k\tilde{D}_j}{\tilde{D}_j+x\tilde{D}_k}\mathbf{k}, \tag{A.48b}$$

$$\beta_2 = (1-y)\tilde{D}_i + xy\left(\tilde{D}_i + \frac{\tilde{D}_k\tilde{D}_j}{\tilde{D}_j+\tilde{D}_kx}\right). \tag{A.48c}$$

Integrating over $\mathbf{p}$, we are left with the expression

$$I_{ij}^k = \frac{T_i T_j}{\gamma_i \gamma_j \gamma_k} \frac{\Gamma(2-d/2)}{(4\pi)^d} \frac{\Gamma(3-d/2)}{\Gamma(2-d/2)} \frac{\Gamma(3-d)}{\Gamma(3-d/2)} \int_0^1 \int_0^1 dxdy \frac{(\alpha_2\beta_2)^{-d/2} y^{1-d/2}}{(\beta_0 - \boldsymbol{\beta}_1^2/\beta_2)^{3-d}}. \tag{A.49}$$

In order to determine corrections to ω and $\mathbf{k}^2$, we consider $W_{ij}^k \equiv \frac{\partial I_{ij}^k}{\partial(-i\omega)}$ and $K_{ij}^k \equiv \frac{\partial I_{ij}^k}{\partial(\mathbf{k}^2)}$, respectively, in the limit $\omega \to 0, \mathbf{k} \to 0$. Additionally, noting $\Gamma(3-d) = -\frac{1}{\epsilon} + \mathcal{O}(1)$ and taking $d \to 4$ while extracting a factor $\mu^{-2\epsilon}$, we have

$$W_{ij}^k = -\frac{T_i T_j}{4\gamma_i \gamma_j \gamma_k} \frac{A_d^2 \mu^{-2\epsilon}}{\epsilon} \int_0^1 \int_0^1 \frac{x}{(\tilde{D}_k \tilde{D}_j xy + \tilde{D}_i(\tilde{D}_j + \tilde{D}_k x)(1-y+xy))^2} dxdy, \tag{A.50a}$$

$$K_{ij}^k = -\frac{T_i T_j}{4\gamma_i \gamma_j \gamma_k} \frac{A_d^2 \mu^{-2\epsilon}}{\epsilon} \int_0^1 \int_0^1 \frac{\tilde{D}_i \tilde{D}_j \tilde{D}_k x(1-y+xy)}{(\tilde{D}_k \tilde{D}_j xy + \tilde{D}_i(\tilde{D}_j + \tilde{D}_k x)(1-y+xy))^3} dxdy, \tag{A.50b}$$

where we have included the geometrical factor A_d^2. We evaluate both of these integrals exactly to find the resulting corrections

$$W_{ij}^k = -\frac{T_i T_j}{4\gamma_i \gamma_j \gamma_k} \frac{A_d^2 \mu^{-2\epsilon}}{\epsilon} \frac{1}{\tilde{D}_k^2 \tilde{D}_i \tilde{D}_j} \log\left(\frac{(\tilde{D}_k + \tilde{D}_i)(\tilde{D}_k + \tilde{D}_j)}{\tilde{D}_i \tilde{D}_j + \tilde{D}_k(\tilde{D}_i + \tilde{D}_j)}\right), \tag{A.51a}$$

$$K_{ij}^k = -\frac{T_i T_j}{4\gamma_i \gamma_j \gamma_k} \frac{A_d^2 \mu^{-2\epsilon}}{\epsilon} \frac{(\tilde{D}_i + \tilde{D}_j)\tilde{D}_k^2 + 2\tilde{D}_i \tilde{D}_j \tilde{D}_k}{2\tilde{D}_i \tilde{D}_j (\tilde{D}_i + \tilde{D}_k)(\tilde{D}_j + \tilde{D}_k)(\tilde{D}_i \tilde{D}_j + \tilde{D}_i \tilde{D}_k + \tilde{D}_j \tilde{D}_k)}, \tag{A.51b}$$

from which we identify the following Z factors

$$Z_{\gamma_1} = 1 - (18u_1^2 W_{11}^1 + 2u_{12}^2 W_{22}^1 + 4\sigma u_{12}^2 W_{12}^2)/\gamma_1, \tag{A.52a}$$

$$Z_{\gamma_2} = 1 - (18u_2^2 W_{22}^2 + 2u_{12}^2 W_{11}^2 + 4\sigma u_{12}^2 W_{21}^1)/\gamma_2, \tag{A.52b}$$

$$Z_{D_1} = 1 - (18u_1^2 K_{11}^1 + 2u_{12}^2 K_{22}^1 + 4\sigma u_{12}^2 K_{12}^2)/D_1, \tag{A.52c}$$

$$Z_{D_2} = 1 - (18u_2^2 K_{22}^2 + 2u_{12}^2 K_{11}^2 + 4\sigma u_{12}^2 K_{21}^1)/D_2, \tag{A.52d}$$

(a) (b)

Figure A.8: Two-loop corrections to $\gamma_1 T_1$. Analogous diagrams for $\gamma_2 T_2$ can be obtained by switching thin black and thick cyan lines.

where the three corrections correspond to diagrams (a), (b), and (c) in Fig. A.6, respectively.

Next, we consider the two-loop corrections to the $\tilde{\phi}_i^2$ terms. There are two such diagrams, which are illustrated in Fig. A.8. The combinatorial and interactions factors are (a) $\frac{2!}{2!} \times 3! \times u_1^2$ and (b) $\frac{2!}{2!} \times 2 \times u_{12}^2$. Note the lack of minus sign due to the sign difference in $\mathcal{A}[\tilde{\phi}_i, \phi_i]$.

Again, the internal diagrams are all of the same form, so we instead consider the generic internal diagram in Fig. A.9. The integral corresponding to this diagram is

$$S_{ijk} = \int \frac{d^d\mathbf{p} d^d\mathbf{q}}{(2\pi)^{2d}} \int \frac{d\omega_1 d\omega_2}{(2\pi)^2} \chi_0^i(\mathbf{p}, \omega_1) \chi_0^j(\mathbf{q}, \omega_2) \chi_0^k(\mathbf{p}+\mathbf{q}, \omega_1+\omega_2), \tag{A.53}$$

or

$$\frac{T_i T_j T_k}{\gamma_i \gamma_j \gamma_k} \int \frac{d^d\mathbf{p} d^d\mathbf{q}}{(2\pi)^{2d}} \int \frac{d\omega_1 d\omega_2}{(2\pi)^2} \frac{8}{[(\tilde{D}_i \mathbf{p}^2 + \tilde{r}_i)^2 + \omega_1^2][(\tilde{D}_j \mathbf{q}^2 + \tilde{r}_j)^2 + \omega_2^2]} \times \frac{1}{(\tilde{D}_k(\mathbf{p}+\mathbf{q})^2 + \tilde{r}_k)^2 + (\omega_1+\omega_2)^2}. \tag{A.54}$$

Integrating out the frequencies, this becomes

$$\frac{T_i T_j T_k}{\gamma_i \gamma_j \gamma_k} \int \frac{d^d\mathbf{p} d^d\mathbf{q}}{(2\pi)^{2d}} \frac{2}{(\tilde{D}_i \mathbf{p}^2 + \tilde{r}_i)(\tilde{D}_j \mathbf{q}^2 + \tilde{r}_j)(\tilde{D}_k(\mathbf{p}+\mathbf{q})^2 + \tilde{r}_k)} \times \frac{1}{\tilde{D}_i \mathbf{p}^2 + \tilde{D}_j \mathbf{q}^2 + \tilde{D}_k(\mathbf{p}+\mathbf{q})^2 + \tilde{r}_i + \tilde{r}_j + \tilde{r}_k}. \tag{A.55}$$

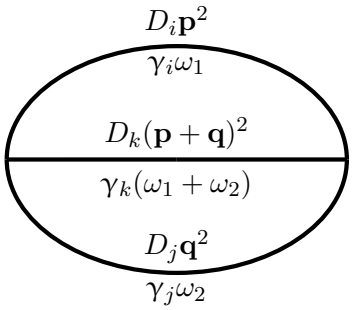

Figure A.9: Generic internal two-loop diagram leading to corrections to $\gamma_i T_i$.

As before, we use Feynman parametrization to integrate over $\mathbf{q}$. However, since there are three terms in the denominator that involve $\mathbf{q}$, we should introduce two Feynman parameters x, y. The integral then becomes

$$2\frac{T_iT_jT_k}{\gamma_i\gamma_j\gamma_k}\Gamma(3)\int\frac{d^d\mathbf{p}}{(2\pi)^d}\frac{1}{\tilde{D}_i\mathbf{p}^2+\tilde{r}_i}\int_0^1\int_0^1 dxdy\int\frac{d^d\mathbf{q}}{(2\pi)^d}\frac{y}{(\alpha_0+2\boldsymbol{\alpha}_1\cdot\mathbf{q}+\alpha_2\mathbf{q}^2)^3}, \tag{A.56}$$

where

$$\alpha_0=(1-y)(\tilde{D}_i+\tilde{D}_k)\mathbf{p}^2+xy\tilde{D}_k\mathbf{p}^2+(1-y)\tilde{r}_i+(1-xy)\tilde{r}_j+(1-y+xy)\tilde{r}_k, \tag{A.57a}$$

$$\boldsymbol{\alpha}_1=\tilde{D}_k(1-y+xy)\mathbf{p}, \tag{A.57b}$$

$$\alpha_2=(1-xy)\tilde{D}_j+(1-y+xy)\tilde{D}_k. \tag{A.57c}$$

Integrating over $\mathbf{q}$, we obtain

$$2\frac{T_iT_jT_k}{\gamma_i\gamma_j\gamma_k}\frac{\Gamma(3-d/2)}{(4\pi)^{d/2}}\int_0^1\int_0^1 dxdy\int\frac{d^d\mathbf{p}}{(2\pi)^d}\frac{y\alpha_2^{-d/2}}{(\tilde{D}_i\mathbf{p}^2+\tilde{r}_i)(\alpha_0-\boldsymbol{\alpha}_1^2/\alpha_2)^{3-d/2}}. \tag{A.58}$$

Introducing a third Feynman parameter, we write this as

$$2\frac{T_iT_jT_k}{\gamma_i\gamma_j\gamma_k}\frac{\Gamma(4-d/2)}{(4\pi)^{d/2}}\int_0^1\int_0^1\int_0^1 dxdydz\int\frac{d^d\mathbf{p}}{(2\pi)^d}\frac{yz^{2-d/2}\alpha_2^{-d/2}}{(\beta_0+2\boldsymbol{\beta}_1\cdot\mathbf{q}+\beta_2\mathbf{p}^2)^{4-d/2}}, \tag{A.59}$$

where

$$\beta_0=(1-yz)\tilde{r}_i+(1-xy)z\tilde{r}_j+(1-y+xy)z\tilde{r}_k, \tag{A.60a}$$

$$\boldsymbol{\beta}_1 = 0, \tag{A.60b}$$

$$\beta_2 = (1-yz)\tilde{D}_i + (1-y+xy)z\tilde{D}_k - \frac{\tilde{D}_k^2(1-y+xy)^2 z}{\tilde{D}_k(1-y+xy)+\tilde{D}_j(1-xy)}. \tag{A.60c}$$

Integrating over $\mathbf{q}$ leaves us with the integral

$$2\frac{T_iT_jT_k}{\gamma_i\gamma_j\gamma_k}\frac{\Gamma(4-d)}{(4\pi)^d}\int_0^1\int_0^1\int_0^1 dxdydz\frac{yz^{2-d/2}(\alpha_2\beta_2)^{-d/2}}{(\beta_0-\boldsymbol{\beta}_1^2/\beta_2)^{4-d}}. \tag{A.61}$$

Several of the Γ factors cancel out; also, we note that $\Gamma(4-d) = 1/\epsilon + \mathcal{O}(1)$. Taking the limit $d \to 4$ and extracting a factor $\mu^{-2\epsilon}$, we rewrite the latter integral as

$$C\int_0^1\int_0^1\int_0^1 dxdydzf(x,y,z,\tilde{D}_i,\tilde{D}_j,\tilde{D}_k), \tag{A.62a}$$

$$f(x,y,z,\tilde{D}_i,\tilde{D}_j,\tilde{D}_k) = \frac{y}{\tilde{D}_j\tilde{D}_k(-1+y-xy^2+x^2y^2)z+\tilde{D}_i(\tilde{D}_j(1-xy)+\tilde{D}_k(1-y+xy)(-1+yz))^2} \tag{A.62b}$$

$$C = \frac{T_iT_jT_k}{2\gamma_i\gamma_j\gamma_k}\frac{A_d^2\mu^{-2\epsilon}}{\epsilon}, \tag{A.62c}$$

where we have included the geometrical factor A_d^2. Taking advantage of the fact that at least two of the $\tilde{D}$ must be the same, this integral can be evaluated analytically as

$$S_{ijj} = S_j^i = \frac{T_iT_j^2}{2\gamma_i\gamma_j^2}\frac{A_d^2\mu^{-2\epsilon}}{\epsilon}\frac{1}{\tilde{D}_i^2\tilde{D}_j^2}\log\left(2^{2\tilde{D}_i/\tilde{D}_j}\frac{\tilde{D}_i+\tilde{D}_j}{\tilde{D}_i}\left(\frac{\tilde{D}_i+\tilde{D}_j}{2\tilde{D}_i+\tilde{D}_j}\right)^{1+2\tilde{D}_i/\tilde{D}_j}\right), \tag{A.63}$$

where $\tilde{D}_i$ corresponds to the field with one propagator and $\tilde{D}_j$ to the field with two.

Thus we identify the corresponding Z factors

$$Z_{\gamma_1}Z_{T_1} = 1 + (3u_1^2S_1^1 + u_{12}^2S_2^1)/(\gamma_1T_1), \tag{A.64a}$$

$$Z_{\gamma_2} Z_{T_2} = 1 + (3u_2^2 S_2^2 + u_{12}^2 S_1^2)/(\gamma_2 T_2), \tag{A.64b}$$

where the two corrections correspond to diagrams (a) and (b) in Fig. A.8, respectively. Note that the factors are half of their combinatorial factors. This is because the zeroth order vertex is $2\gamma_i T_i$ rather than $\gamma_i T_i$.

A.4 Method of Characteristics

In this section, we employ the method of characteristics in order to derive the scaling behavior of the correlation and response functions at or near a given fixed point. Since the correlation and response functions do not depend on the renormalized parameters, they are independent of the momentum scale of renormalization μ. Thus,

$$\mu \frac{d}{d\mu} C_i(\mathbf{q}/\mu, \omega/\mu^2, \{p_R\}, \{u_R\}) = 0, \tag{A.65a}$$

$$\mu \frac{d}{d\mu} \chi_i(\mathbf{q}/\mu, \omega/\mu^2, \{p_R\}, \{u_R\}) = 0, \tag{A.65b}$$

where $\{p\} = \{r_i, \gamma_i, D_i, T_i\}$ and $\{u\} = \{u_1, u_2, u_{12}\}$ are the interaction strengths. Additionally, we define dimensionless scaling functions via $C_i = \mu^{-4} \hat{C}_i$ and $\chi_i = \mu^{-2} \hat{\chi}_i$, where the scaling factors are due to the scaling dimensions of the fields as well as the delta functions—which are factored out—corresponding to momentum and energy conservation. In each case, we can rewrite the total derivative $\mu \frac{d}{d\mu}$ in

terms of the partial derivatives with respect to other parameters as

$$\mu \frac{d}{d\mu} C_i = \mu^{-4} \left(\sum_p \gamma_p p_R \partial_{p_R} + \sum_s \beta_u \partial_{u_R} - 4 \right) \hat{C}_i, \tag{A.66a}$$

$$\mu \frac{d}{d\mu} \chi_i = \mu^{-2} \left(\sum_p \gamma_p p_R \partial_{p_R} + \sum_s \beta_u \partial_{u_R} - 2 \right) \hat{\chi}_i, \tag{A.66b}$$

Next we employ the method of characteristics and define $\tilde{\mu}(l) = \mu l$. We then introduce the flowing dimensionless parameters $\tilde{p}(l)$, $\tilde{u}(l)$ via

$$l \frac{d\tilde{p}(l)}{dl} = \gamma_p(l) \tilde{p}(l), \qquad \tilde{p}(1) = p_R, \tag{A.67}$$

$$l \frac{d\tilde{u}(l)}{dl} = \beta_u(l), \qquad \tilde{u}(1) = u_R. \tag{A.68}$$

Casting the correlation and response functions in terms of the new flowing parameters and l, the scaling functions satisfy the differential equations

$$\left(\frac{d}{dl} - 4 \right) \hat{C}_i(\mathbf{q}/(\mu l), \omega/(\mu l)^2, \{\tilde{p}(l)\}, \{\tilde{u}(l)\}) = 0, \tag{A.69a}$$

$$\left(\frac{d}{dl} - 2 \right) \hat{\chi}_i(\mathbf{q}/(\mu l), \omega/(\mu l)^2, \{\tilde{p}(l)\}, \{\tilde{u}(l)\}) = 0. \tag{A.69b}$$

At the fixed point, $\beta_u(l) = 0$ for all u and the parameters and flow functions assume their fixed-point values $\tilde{u}(l) = u^*$ and $\gamma_p(l) = \gamma_p^*$. This allows us to easily solve the flowing parameters as

$$\tilde{p}(l) = p_R l^{\gamma_p^*}. \tag{A.70}$$

Thus, at the fixed point, we can solve Eq. (A.69) and find the scaling form of the correlation and response functions as

$$C_i(\mathbf{q}, \omega, \{p_R\}) = (\mu l)^{-4} \hat{C}_i(\mathbf{q}/(\mu l), \omega/(\mu l)^2, \{p_R l^{\gamma_p^*}\}), \tag{A.71a}$$

$$\chi_i(\mathbf{q}, \omega, \{p_R\}) = (\mu l)^{-2} \hat{\chi}_i(\mathbf{q}/(\mu l), \omega/(\mu l)^2, \{p_R l^{\gamma_p^*}\}), \tag{A.71b}$$

where the u arguments have been dropped since they approach a constant at the fixed point and do not affect the universal scaling behavior. Since all the terms in the perturbation series involve integrals of Gaussian propagators, we can simplify reduce the scaling functions to [cf. Eq. (A.25)],

$$\hat{C}_i\left(\frac{\mathbf{q}}{\mu l}, \frac{\omega}{(\mu l)^2}, D_R l^{\gamma_D^*}, T_R l^{\gamma_T^*}, \boldsymbol{\gamma}_{i_R} l^{\gamma_\gamma^*}, \{r_{j_R} l^{\gamma_{r_j}}\}\right) \to \frac{\boldsymbol{\gamma}_{i_R} T_R}{D_R^2} l^{\gamma_\gamma^* + \gamma_T^* - 2\gamma_D^*} \hat{C}_i\left(\frac{\mathbf{q}}{\mu l}, \frac{\boldsymbol{\gamma}_{i_R}\omega}{\mu^2 D_R^2} l^{-2-\gamma_D^*+\gamma_\gamma^*}, 1, 1, 1, \left\{\frac{r_{j_R}}{D_R} l^{\gamma_{r_j}^* - \gamma_D^*}\right\}\right), \quad \text{(A.72a)}$$

$$\hat{\chi}_i\left(\frac{\mathbf{q}}{\mu l}, \frac{\omega}{(\mu l)^2}, D_R l^{\gamma_D^*}, T_R l^{\gamma_T^*}, \boldsymbol{\gamma}_{i_R} l^{\gamma_\gamma^*}, \{r_{j_R} l^{\gamma_{r_j}}\}\right) \to D_R^{-1} l^{-\gamma_D^*} \hat{\chi}_i\left(\frac{\mathbf{q}}{\mu l}, \frac{\boldsymbol{\gamma}_{i_R}\omega}{\mu^2 D_R^2} l^{-2-\gamma_D^*+\gamma_\gamma^*}, 1, 1, 1, \left\{\frac{r_{j_R}}{D_R} l^{\gamma_{r_j}^* - \gamma_D^*}\right\}\right), \quad \text{(A.72b)}$$

where we have utilized the fact that the scaling behavior of $\boldsymbol{\gamma}, D, T$ is the same for both fields. The above simplification was made by noting that in the Gaussian propagators, we can absorb some arguments into others, e.g., by absorbing a factor $\boldsymbol{\gamma}_i$ into the definition of ω or noting that T_i enters only as an overall multiplicative constant in C_i. Upon applying the matching condition $|\mathbf{q}| = \mu l$, we can express the correlation and response functions as

$$C_i(\mathbf{q}, \omega, \{r_j\}) \propto |\mathbf{q}|^{-4+\gamma_\gamma^*+\gamma_T^*-2\gamma_D^*} \hat{C}_i\left(\frac{\omega}{|\mathbf{q}|^{2+\gamma_D^*-\gamma_\gamma^*}}, \left\{\frac{r_{j_R}}{|\mathbf{q}|^{-\gamma_{r_j}^*+\gamma_D^*}}\right\}\right), \quad \text{(A.73a)}$$

$$\chi_i(\mathbf{q}, \omega, \{r_j\}) \propto |\mathbf{q}|^{-2-\gamma_D^*} \hat{\chi}_i\left(\frac{\omega}{|\mathbf{q}|^{2+\gamma_D^*-\gamma_\gamma^*}}, \left\{\frac{r_{j_R}}{|\mathbf{q}|^{-\gamma_{r_j}^*+\gamma_D^*}}\right\}\right), \quad \text{(A.73b)}$$

where we have further simplified the arguments of the scaling functions by dropping factors of μ and p_R and excluding arguments involving only a constant in a slight abuse of notation. Comparing these scaling functions against those in Eq. (2.8), we

identify the critical exponents

$$\eta = \gamma_T^* - \gamma_D^*, \quad \eta' = -\gamma_D^*, \quad z = 2 + \gamma_D^* - \gamma_\Upsilon^*. \tag{A.74}$$

Simiarly, we can identify $\nu_j^{-1} = -\gamma_{r_j}^* + \gamma_D^*$ although the subtleties of a complex-valued exponent ν at the NEFPs are discussed in detail in the main text.

Appendix B: Appendices to Chapter 3

B.1 Gutzwiller Mean Field Theory

In Sec. 3.2, we motivated our use of a cumulant expansion approximation due to the fact that Gutzwiller mean field theory fails to provide any insight into our model. In this section, we provide the reasons for this failure. Using an inhomogeneous Gutzwiller mean-field approximation, we assume the density matrix has the form

$$\rho = \bigotimes_i \rho_i, \tag{B.1}$$

which assumes there are no correlations between different atoms [137, 138]. The method is inhomogeneous in the sense that each atom has its own density matrix, whereas in homogeneous Gutzwiller mean field theory all atoms have the same density matrix. This results in an effective local Hamiltonian

$$H_i^{\text{eff}} = -\delta\sigma_i^{ss} + \Omega(\sigma_i^{sg} + \sigma_i^{gs}) + \sum_j [V_{ij}\sigma_i^{ps}\langle\sigma_j^{sp}\rangle + H.c.]. \tag{B.2}$$

Under this approximation, the interactions behave as an effective driving term between the s and p states whose strength and phase are determined by the $\langle\sigma^{sp}\rangle$ coherences of the surrounding atoms. This explicitly assumes a breaking of the $U(1)$ symmetry $|p\rangle \to e^{i\phi}|p\rangle$. If it is not broken, then the system behaves as if there are

no interactions. Additionally, in the full master equation's steady state, the ratio of s to p atoms is fixed because the number of p atoms only changes due to single-site decay processes. However, under the mean-field approximation, the effective drive between s and p states will inevitably change this ratio in steady state.

If we want to keep the ratio of s to p atoms reasonably close to the true value, the effective Rabi frequency must be small. In this limit, we can easily solve perturbatively for the steady state value of $\langle \sigma^{sp} \rangle$ as a function of the effective Rabi frequency $\Omega_{\text{eff}} = \sum_j V_{ij} \langle \sigma_j^{sp} \rangle$

$$\langle \sigma_i^{sp} \rangle \approx \frac{i(\langle \sigma_{V=0}^{ss} \rangle - \langle \sigma_{V=0}^{pp} \rangle)}{i\delta - \frac{\gamma_s + \gamma_p + \gamma_R}{2}} \Omega_{\text{eff}}, \tag{B.3}$$

where $\langle \sigma_{V=0}^{ss} \rangle$ and $\langle \sigma_{V=0}^{pp} \rangle$ are the s and p populations with no interactions. In this limit, the coherence depends linearly on the effective Rabi frequency, which can be written as a matrix equation

$$\langle \sigma_i^{sp} \rangle \approx C \sum_j V_{ij} \langle \sigma_j^{sp} \rangle, \tag{B.4}$$

where C is some complex constant with nonzero imaginary part. Equation (B.4) may be thought of in terms of finding the eigenvector associated with an eigenvalue $1/C$ of the matrix defined by V_{ij} where $V_{ii} = 0$. However, since V_{ij} is a symmetric, real matrix, it has only real eigenvalues, so $1/C$ cannot be an eigenvalue and the only solution to Eq. (B.4) is $\langle \sigma_i^{sp} \rangle = 0$. Thus the only possibility of a low effective Rabi frequency mean-field solution with nonzero coherences is one which is not constant in time, such as a limit cycle.

In order to determine whether other nontrivial solutions are possible, we initialize a cubic lattice of randomized density matrices for each lattice site and evolve

the system according to the mean field equations of motion. This was done for a variety of numerically feasible parameters, while the nearest neighbor interaction strength remained at least two orders of magnitude above Ω and all decay rates.

In all cases, including those with large initial Ω_{eff}, we found that the $\langle \sigma^{sp} \rangle$ coherences all decay to zero in steady state, in which case the system behaves as if there are no interactions. This would not occur if the interactions were of the form

$$\sum_{i \neq j} V_{ij} \sigma_i^{ss} \sigma_j^{pp}. \tag{B.5}$$

Collective decay between the s and p states does result in nonzero $\langle \sigma^{sp} \rangle$ coherences in steady state, but we find numerically that the effect of interactions when collective decay is included is small. Furthermore, the experimental results in Refs. [64, 198] indicate that collective decay is not the source of the observed broadening and is suppressed by the dipole-dipole interactions. For these reasons, we do not consider collective decay in the above mean field analysis.

B.2 Cumulant Expansion Equations of Motion

In this section, in order to illustrate how the cumulant expansion approximation truncates the hierarchy of differential equations, we will present example derivations for a single-atom expectation value $\langle \sigma_i^{sg} \rangle$ as well as a two-atom expectation value $\langle \sigma_i^{sp} \sigma_j^{pg} \rangle$ while taking advantage of the symmetries mentioned in Sec. 3.2.1. In the full master equation, we can consider the evolution of the expectation value of an operator $\mathcal{O}$ via $\partial_t \langle \mathcal{O} \rangle = Tr(\dot{\rho} \mathcal{O})$. Thus the corresponding differential equations

for the two operators are

$$\partial_t\langle\sigma_i^{sg}\rangle = i\Omega(\langle\sigma_i^{gg}\rangle - \langle\sigma_i^{ss}\rangle) + i\sum_{k\neq i} V_{ki}\langle\sigma_k^{sp}\sigma_i^{pg}\rangle - \frac{\gamma_s+\gamma_R+2\gamma_d}{2}\langle\sigma_i^{sg}\rangle, \tag{B.6}$$

$$\begin{aligned}\partial_t\langle\sigma_i^{sp}\sigma_j^{pg}\rangle = {} & i\Omega(\langle\sigma_i^{gp}\sigma_j^{pg}\rangle - \langle\sigma_i^{sp}\sigma_j^{ps}\rangle) - \frac{\gamma_s+\gamma_R+2\gamma_p+3\gamma_d}{2}\langle\sigma_i^{sp}\sigma_j^{pg}\rangle \\ & + i\sum_{k\neq i} V_{ki}(\langle\sigma_i^{pp}\sigma_k^{sp}\sigma_j^{pg}\rangle - \langle\sigma_i^{ss}\sigma_k^{sp}\sigma_j^{pg}\rangle) + \ i\sum_{k\neq j} V_{kj}\langle\sigma_i^{sp}\sigma_j^{sg}\sigma_k^{ps}\rangle,\end{aligned} \tag{B.7}$$

where the sums are only over k. Note that some of the three-atom operators may sometimes be two-atom operators if two of the indices are the same, in which case no approximation is necessary and they are treated exactly.

In the above equations of motion, only the interaction terms couple operators involving a different number of atoms. The driving terms and decay terms always couple to the same sites. Additionally, since the interaction is composed of only two-atom terms, n-atom operators can only couple to operators involving n or $n\pm1$ sites. As a result, assuming three-atom connected correlations to be zero implies all higher-order connected correlations are zero, truncating the hierarchy of equations that results from the interactions.

Once we apply translational invariance, single-atom expectation values are site-independent, e.g. $\langle\sigma_i^{sg}\rangle = \langle\sigma^{sg}\rangle$, and two-atom expectation values depend only on their displacement vector, e.g. $\langle\sigma_i^{sp}\sigma_j^{pg}\rangle = \langle\sigma_0^{sp}\sigma_{j-i}^{pg}\rangle$. Furthermore, the $U(1)$ symmetry of $|p\rangle \to |p\rangle e^{i\phi}$ implies terms like $\langle\sigma_i^{sp}\rangle$ or $\langle\sigma_i^{pg}\sigma_j^{ss}\rangle$ are zero in steady state. Applying the cumulant expansion approximation, the terms in the equations of motion due solely to the interactions become

$$\partial_t\langle\sigma^{sg}\rangle = \cdots + i\sum_{j\neq0} V_{0j}\langle\sigma_0^{sp}\sigma_j^{pg}\rangle, \tag{B.8}$$

$$\partial_t\langle\sigma_0^{sp}\sigma_i^{pg}\rangle = \cdots + iV_{0i}\langle\sigma_0^{pp}\sigma_i^{sg}\rangle + i\sum_{j\neq 0,i} V_{ji}\langle\sigma_0^{sp}\sigma_j^{pg}\rangle(\langle\sigma^{pp}\rangle - \langle\sigma^{ss}\rangle) + i\sum_{j\neq 0,i} V_{ji}\langle\sigma_0^{sp}\sigma_j^{ps}\rangle\langle\sigma^{sg}\rangle. \tag{B.9}$$

Note that there are two types of interaction terms present above. The first involves terms whose interaction strength and two-atom operator correspond to the same atoms, while in the second only one index matches.

B.3 Quantum Trajectories

In this section, we verify that the cumulant expansion approach is a reasonable approach by comparing it to the exact numerical approach of quantum trajectories [211–214]. However, the quantum trajectories approach can be applied for at most 10 atoms due to computational constraints, which puts a limit on the range of C_3 we can consider if we want to keep boundary effects to a minimum. Here, we focus on a 1D lattice of atoms with periodic boundary conditions. To take this into account, the interaction between two given atoms is taken to be

$$V_{ij} = \frac{C_3}{r_1^3} + \frac{C_3}{r_2^3}, \tag{B.10}$$

where $r_{1,2}$ are the two smallest distances between atoms i and j.

We can consider in general a quantum master equation of the following form

$$\dot{\rho} = -i[H,\rho] + \sum_i \gamma_i \left(\mathcal{O}_i\rho\mathcal{O}_i^\dagger - \frac{1}{2}\{\mathcal{O}_i^\dagger\mathcal{O}_i,\rho\}\right), \tag{B.11}$$

which may be rewritten in terms of an effective non-Hermitian Hamiltonian and recycling terms

$$\dot{\rho} = -i(H_{\text{eff}}\rho - \rho H_{\text{eff}}^\dagger) + \sum_i \gamma_i\mathcal{O}_i\rho\mathcal{O}_i^\dagger, \tag{B.12a}$$

$$H_{\text{eff}} = H - \frac{i}{2}\sum_i \gamma_i \mathcal{O}_i^\dagger \mathcal{O}_i. \tag{B.12b}$$

Rather than considering the evolution of the density matrix, we will instead consider stochastic evolution of a normalized state $|\psi(t)\rangle$ according to H_{eff}. As a result of the non-Hermitian part of the effective Hamiltonian, the norm of $|\psi(t)\rangle$ is not conserved, and after a time dt it will have a norm of $\langle\tilde{\psi}(t+dt)|\tilde{\psi}(t+dt)\rangle = 1-p$. The deviation p corresponds directly to the probability that a quantum jump has occurred due to the Lindbladian. In the case where several possible types of quantum jumps are possible, as is the case here, each process is weighted according to

$$p_i = w_i p, \tag{B.13a}$$

$$w_i = \frac{\gamma_i \langle\psi(t)|\mathcal{O}_i^\dagger \mathcal{O}_i|\psi(t)\rangle}{\sum_i \gamma_i \langle\psi(t)|\mathcal{O}_i^\dagger \mathcal{O}_i|\psi(t)\rangle}. \tag{B.13b}$$

Thus with probability p_i the new state is

$$|\psi(t+dt)\rangle = \mathcal{O}_i|\psi(t)\rangle / \sqrt{\langle\mathcal{O}_i^\dagger \mathcal{O}_i\rangle}, \tag{B.14}$$

and with probability $1-p$ the new state is

$$|\psi(t+dt)\rangle = |\tilde{\psi}(t+dt)\rangle / \sqrt{1-p}. \tag{B.15}$$

In contrast to a density matrix approach, there is no specific steady-state $|\psi\rangle$ which is constant in time. Instead, we extract the corresponding steady-state density matrix by considering time averages of $|\psi\rangle$ once it has evolved sufficiently long to exhibit steady-state behavior. This is effectively equivalent to averaging over many runs to a specific time which is large compared to the steady-state relaxation time. In Fig. B.1, we compare the results from quantum trajectories to the results from

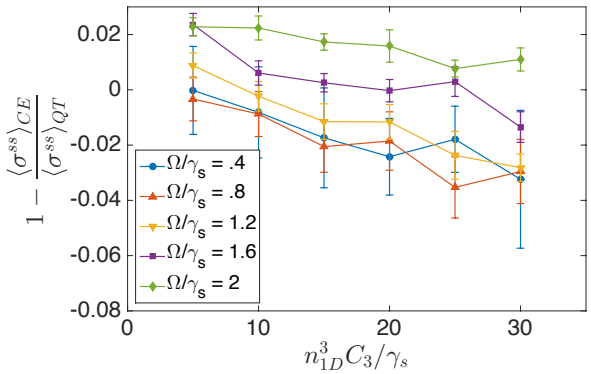

Figure B.1: Relative error of cumulant expansion (CE) with respect to quantum trajectories (QT). Error bars denote standard error from quantum trajectories sampling. The total sampling time is 4500 γ_s^{-1}.

cumulant expansion. We see that at least in the limit of small interaction strengths and densities, the steady-state error due to the cumulant expansion is not too large.

B.4 Comparison of Different Rate Equation Approaches

In this section, we compare the different implementations of the decoherence in the rate equation model. In particular, we will consider how the distribution of atoms and the summation of the interaction terms in the decoherence affect the lineshapes and scaling behavior of the populations. The two distributions we consider will be a Gaussian distribution, as in the main text, and a lattice distribution. The two methods of summing the interaction terms are expressed below

$$\Gamma_i = \gamma_s + \gamma_R + C_3 \left| \sum_{j \neq i} V_{ij} p_j \right|, \tag{B.16a}$$

$$\Gamma_i = \gamma_s + \gamma_R + C_3 \sum_{j \neq i} |V_{ij} p_j| . \tag{B.16b}$$

The first of these two methods is used in the main text and allows for the decoherence due to some p atoms to reduce the decoherence due to other p atoms when the

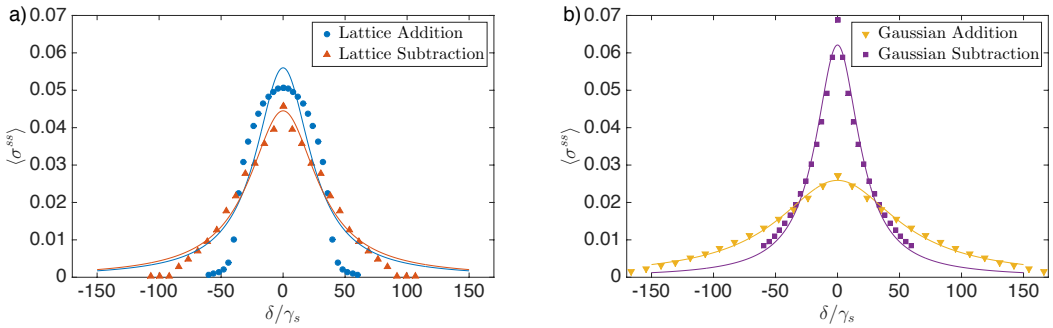

Figure B.2: Example lineshapes for several implementations of decoherence, where lines correspond to Lorentzian fits. (a) Lattice implementations of the rate equations. (b) Gaussian distribution implementation of the rate equations.

interactions are of a different sign. The second of these two methods only allows different sources of decoherence to add together. As a shorthand, we will refer to the former as the subtraction method and the latter as the addition method.

We will focus on how the different approaches affect the lineshapes of the Rydberg populations. Since the experimentally observed lineshapes are quite Lorentzian [64, 198], we should hope to reproduce this behavior as well. Example lineshapes are shown for each implementation of decoherence in Fig. B.2.

In both of the lattice distribution approaches, we see that although there is clear broadening evident, the population drops off in the wings too fast to be considered Lorentzian, although this is less extreme for the subtraction method. Additionally, the dome lineshapes of the lattice addition method are nearly identical to the uniform approach of Ref. [198]. This occurs because the rate equations for the internal lattice sites are all nearly identical. Since each atom behaves identically, if there is a particular detuning at which a given atom's population is no longer drastically enhanced, then this will be the case for the entire sample, leading to a sharp cutoff. By introducing more inhomogeneity, different atoms experience this

cutoff at different detunings, leading to a more gradual decline in population.

The lineshapes produced by the Gaussian distributions are fairly Lorentzian for both choices of implementing the decoherence. We find that the populations from the addition method tend to fall off slightly faster than Lorentzian at large detunings, while the populations from the subtraction method tend to have a sharper peak on resonance than a Lorentzian.

Additionally, in spite of the fact that these approaches result in quite different lineshapes, their scaling behavior is qualitatively the same. For example, if the parameters are changed such that either the width or the resonant population doubles for one approach, the width or the resonant population of the other approaches will approximately double as well.

B.5 Experimental Methods

In this section, we describe the experimental methods used in the main text. The details of the experimental setup are described in Refs. [64, 218]. In a nutshell, the basis for the apparatus is a ^{87}Rb Bose-Einstein condensate (BEC) machine producing a BEC composed of $N \approx 4 \times 10^4$ atoms every 16 seconds. We excite the atoms to the $18s_{1/2}$ state using a two-photon transition via the $5p_{1/2}$ state with intermediate detuning $\Delta/2\pi \approx 240$ MHz. The lower and upper Rabi frequencies are independently calibrated to $\Omega_1/2\pi = 0$ MHz to 5 MHz and $\Omega_2/2\pi \approx 12.5$ MHz. In keeping with the notation of the main text, these are both half the typical definition of the Rabi frequency. The two lasers are locked to the same high-finesse optical

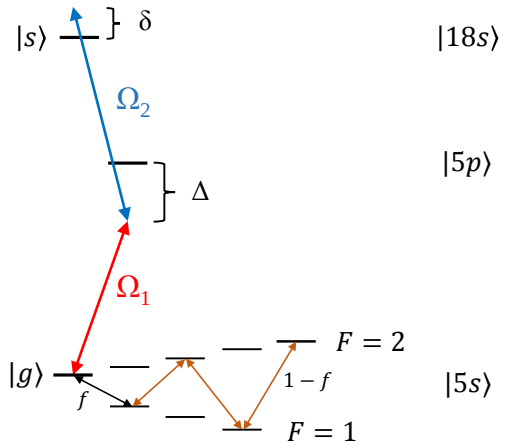

Figure B.3: Experimental excitation and measurement scheme. The ground-state manifold is initially populated with a fraction f in the $|g\rangle = |F = 2, m_F = -2\rangle$ state and $1 - f$ in the $|F = 2, m_F = 2\rangle$ state using three applications of microwave rapid adiabatic passage. The $|F = 2, m_F = -2\rangle$ state is then driven via an off-resonant two-photon transition through the $5p_{1/2}$ state to the $18s_{1/2}$ state with intermediate detuning Δ, two-photon detuning δ, and lower and upper Rabi frequencies Ω_1 and Ω_2.

cavity with < 10 kHz linewidth and are tuned for the transition $|g\rangle = |5s, F = 2, m_F = -2\rangle \rightarrow |s\rangle = |18s, F = 2, m_F = -2\rangle$. The BEC is created in the $|F = 1, m_F = -1\rangle$ state, and we control the fraction f transferred to $|5s, F = 2, m_F = -2\rangle$ via microwave rapid adiabatic passage. The remaining atoms are then transferred to the shelving state $|F = 2, m_F = 2\rangle$. This offers control over the fractional density of atoms participating to the Rydberg excitation. This process is shown in Fig. B.3.

The post-excitation populations in the ground hyperfine manifold are separated in time-of-flight with a Stern-Gerlach magnetic field gradient and measured via absorption imaging. Experiments are done in a 3D optical lattice made with 812 nm light, resulting in a lattice spacing of 406 nm. This distance is comparable to the $18s$ van der Waals blockade radius. We measure the resonant Rydberg pumping rate R_0 as a function of the two-photon Rabi frequency $\Omega = \Omega_1\Omega_2/\Delta$ for two

fractional densities f. This is achieved by measuring the post-excitation population in the $|5s, F = 2, m_F = -2\rangle$ initial state as a function of the excitation time, to which we fit an exponential to extract the pumping rate. We obtain the resonant rate R_0 due to the Rydberg s state by subtracting the off-resonant $5s - 5p$ optical pumping rate. The measurements presented in the main text are done with two different fractional densities: $f = 25\%$ and $f = 100\%$.

Bibliography

[1] Rudolf Grimm, Matthias Weidemüller, and Yurii B. Ovchinnikov. Optical Dipole Traps for Neutral Atoms. In *Advances in Atomic, Molecular, and Optical Physics*, volume 42, pages 95–170. 2000.

[2] Immanuel Bloch. Ultracold quantum gases in optical lattices. *Nat. Phys.*, 1(1):23–30, October 2005.

[3] Daniel Barredo, Sylvain de Léséleuc, Vincent Lienhard, Thierry Lahaye, and Antoine Browaeys. An atom-by-atom assembler of defect-free arbitrary two-dimensional atomic arrays. *Science*, 354(6315):1021–1023, November 2016.

[4] Manuel Endres, Hannes Bernien, Alexander Keesling, Harry Levine, Eric R Anschuetz, Alexandre Krajenbrink, Crystal Senko, Vladan Vuletic, Markus Greiner, and Mikhail D Lukin. Atom-by-atom assembly of defect-free one-dimensional cold atom arrays. *Science*, 354(6315):1024–1027, November 2016.

[5] M. A. Norcia, A. W. Young, and A. M. Kaufman. Microscopic Control and Detection of Ultracold Strontium in Optical-Tweezer Arrays. *Phys. Rev. X*, 8(4):041054, December 2018.

[6] Johann G. Danzl, Elmar Haller, Mattias Gustavsson, Manfred J. Mark, Russell Hart, Nadia Bouloufa, Olivier Dulieu, Helmut Ritsch, and H.-C. Nagerl. Quantum Gas of Deeply Bound Ground State Molecules. *Science*, 321(5892):1062–1066, August 2008.

[7] Amodsen Chotia, Brian Neyenhuis, Steven A. Moses, Bo Yan, Jacob P. Covey, Michael Foss-Feig, Ana Maria Rey, Deborah S. Jin, and Jun Ye. Long-Lived Dipolar Molecules and Feshbach Molecules in a 3D Optical Lattice. *Phys. Rev. Lett.*, 108(8):080405, February 2012.

[8] L. R. Liu, J. D. Hood, Y. Yu, J. T. Zhang, K. Wang, Y.-W. Lin, T. Rosenband, and K.-K. Ni. Molecular Assembly of Ground-State Cooled Single Atoms. *Phys. Rev. X*, 9(2):021039, May 2019.

[9] D. J. Wineland, J. C. Bergquist, Wayne M. Itano, J. J. Bollinger, and C. H. Manney. Atomic-Ion Coulomb Clusters in an Ion Trap. *Phys. Rev. Lett.*, 59(26):2935–2938, December 1987.

[10] M. G. Raizen, J. M. Gilligan, J. C. Bergquist, W. M. Itano, and D. J. Wineland. Ionic crystals in a linear Paul trap. *Phys. Rev. A*, 45(9):6493–6501, May 1992.

[11] M.J. Hartmann, F.G.S.L. Brandão, and M.B. Plenio. Quantum many-body phenomena in coupled cavity arrays. *Laser Photonics Rev.*, 2(6):527–556, December 2008.

[12] Andrew A. Houck, Hakan E. Türeci, and Jens Koch. On-chip quantum simulation with superconducting circuits. *Nat. Phys.*, 8(4):292, 2012.

[13] Iacopo Carusotto and Cristiano Ciuti. Quantum fluids of light. *Rev. Mod. Phys.*, 85(1):299–366, February 2013.

[14] Markus Greiner, Olaf Mandel, Tilman Esslinger, Theodor W. Hänsch, and Immanuel Bloch. Quantum phase transition from a superfluid to a Mott insulator in a gas of ultracold atoms. *Nature (London)*, 415(6867):39–44, January 2002.

[15] Xibo Zhang, C.-L. Hung, S.-K. Tung, and Cheng Chin. Observation of Quantum Criticality with Ultracold Atoms in Optical Lattices. *Science*, 335(6072):1070–1072, March 2012.

[16] M. Aidelsburger, M. Atala, M. Lohse, J. T. Barreiro, B. Paredes, and I. Bloch. Realization of the Hofstadter Hamiltonian with Ultracold Atoms in Optical Lattices. *Phys. Rev. Lett.*, 111(18):185301, October 2013.

[17] M. Hafezi, S. Mittal, J. Fan, A. Migdall, and J. M. Taylor. Imaging topological edge states in silicon photonics. *Nat. Photonics*, 7(12):1001–1005, December 2013.

[18] N. Goldman, J. C. Budich, and P. Zoller. Topological quantum matter with ultracold gases in optical lattices. *Nat. Phys.*, 12(7):639–645, July 2016.

[19] N. R. Cooper, J. Dalibard, and I. B. Spielman. Topological bands for ultracold atoms. *Rev. Mod. Phys.*, 91(1):015005, March 2019.

[20] A. V. Gorshkov, M. Hermele, V. Gurarie, C. Xu, P. S. Julienne, J. Ye, P. Zoller, E. Demler, M. D. Lukin, and A. M. Rey. Two-orbital S U(N) magnetism with ultracold alkaline-earth atoms. *Nat. Phys.*, 6(4):289–295, April 2010.

[21] X. Zhang, M. Bishof, S. L. Bromley, C. V. Kraus, M. S. Safronova, P. Zoller, A. M. Rey, and J. Ye. Spectroscopic observation of SU(N)-symmetric interactions in Sr orbital magnetism. *Science*, 345(6203):1467–1473, September 2014.

[22] A. W. Glaetzle, M. Dalmonte, R. Nath, I. Rousochatzakis, R. Moessner, and P. Zoller. Quantum Spin-Ice and Dimer Models with Rydberg Atoms. *Phys. Rev. X*, 4(4):041037, November 2014.

[23] Immanuel Bloch, Jean Dalibard, and Wilhelm Zwerger. Many-body physics with ultracold gases. *Rev. Mod. Phys.*, 80(3):885–964, July 2008.

[24] Peter Schauß, Marc Cheneau, Manuel Endres, Takeshi Fukuhara, Sebastian Hild, Ahmed Omran, Thomas Pohl, Christian Gross, Stefan Kuhr, and Immanuel Bloch. Observation of spatially ordered structures in a two-dimensional Rydberg gas. *Nature (London)*, 491(7422):87–91, November 2012.

[25] Philip Richerme, Zhe Xuan Gong, Aaron Lee, Crystal Senko, Jacob Smith, Michael Foss-Feig, Spyridon Michalakis, Alexey V. Gorshkov, and Christopher Monroe. Non-local propagation of correlations in quantum systems with long-range interactions. *Nature (London)*, 511(7508):198–201, July 2014.

[26] Renate Landig, Lorenz Hruby, Nishant Dogra, Manuele Landini, Rafael Mottl, Tobias Donner, and Tilman Esslinger. Quantum phases from competing short- and long-range interactions in an optical lattice. *Nature (London)*, 532(7600):476–479, April 2016.

[27] Darrick E. Chang, Vladan Vuletić, and Mikhail D. Lukin. Quantum nonlinear optics — photon by photon. *Nat. Photonics*, 8(9):685–694, September 2014.

[28] J. I. Cirac and P. Zoller. Quantum Computations with Cold Trapped Ions. *Phys. Rev. Lett.*, 74(20):4091–4094, May 1995.

[29] D. Kielpinski, C. Monroe, and D. J. Wineland. Architecture for a large-scale ion-trap quantum computer. *Nature (London)*, 417(6890):709–711, June 2002.

[30] M. Saffman, T. G. Walker, and K. Mølmer. Quantum information with Rydberg atoms. *Rev. Mod. Phys.*, 82(3):2313–2363, August 2010.

[31] T. Xia, M. Lichtman, K. Maller, A. W. Carr, M. J. Piotrowicz, L. Isenhower, and M. Saffman. Randomized BenchMarchking of Single-Qubit Gates in a 2D Array of Neutral-Atom Qubits. *Phys. Rev. Lett.*, 114(10):100503, March 2015.

[32] K. M. Maller, M. T. Lichtman, T. Xia, Y. Sun, M. J. Piotrowicz, A. W. Carr, L. Isenhower, and M. Saffman. Rydberg-blockade controlled-not gate and entanglement in a two-dimensional array of neutral-atom qubits. *Phys. Rev. A*, 92(2):022336, August 2015.

[33] J. P. Gaebler, T. R. Tan, Y. Lin, Y. Wan, R. Bowler, A. C. Keith, S. Glancy, K. Coakley, E. Knill, D. Leibfried, and D. J. Wineland. High-Fidelity Universal Gate Set for 9Be+ Ion Qubits. *Phys. Rev. Lett.*, 117(6):060505, August 2016.

[34] Harry Levine, Alexander Keesling, Giulia Semeghini, Ahmed Omran, Tout T. Wang, Sepehr Ebadi, Hannes Bernien, Markus Greiner, Vladan Vuletić, Hannes Pichler, and Mikhail D. Lukin. Parallel Implementation of High-Fidelity Multiqubit Gates with Neutral Atoms. *Phys. Rev. Lett.*, 123(17):170503, October 2019.

[35] C. Figgatt, A. Ostrander, N. M. Linke, K. A. Landsman, D. Zhu, D. Maslov, and C. Monroe. Parallel entangling operations on a universal ion-trap quantum computer. *Nature (London)*, 572(7769):368–372, August 2019.

[36] S. Diehl, A. Micheli, A. Kantian, B. Kraus, H. P. Büchler, and P. Zoller. Quantum states and phases in driven open quantum systems with cold atoms. *Nat. Phys.*, 4(11):878–883, November 2008.

[37] Frank Verstraete, Michael M Wolf, and J Ignacio Cirac. Quantum computation and quantum-state engineering driven by dissipation. *Nat. Phys.*, 5(9):633–636, September 2009.

[38] Julio T. Barreiro, Markus Müller, Philipp Schindler, Daniel Nigg, Thomas Monz, Michael Chwalla, Markus Hennrich, Christian F. Roos, Peter Zoller, and Rainer Blatt. An open-system quantum simulator with trapped ions. *Nature (London)*, 470(7335):486–491, February 2011.

[39] Y. Lin, J. P. Gaebler, F. Reiter, T. R. Tan, R. Bowler, A. S. Sørensen, D. Leibfried, and D. J. Wineland. Dissipative production of a maximally entangled steady state of two quantum bits. *Nature (London)*, 504(7480):415–418, December 2013.

[40] S. Shankar, M. Hatridge, Z. Leghtas, K. M. Sliwa, A. Narla, U. Vool, S. M. Girvin, L. Frunzio, M. Mirrahimi, and M. H. Devoret. Autonomously stabilized entanglement between two superconducting quantum bits. *Nature (London)*, 504(7480):419–422, December 2013.

[41] C. W. Gardiner and P. Zoller. *Quantum Noise*. Springer-Verlag Berlin Heidelberg, 3rd edition, 2004.

[42] Heinz-Peter Breuer and Francesco Petruccione. *The Theory of Open Quantum Systems*. Oxford University Press, New York, January 2007.

[43] John Cardy. *Scaling and Renormalization in Statistical Physics*. Cambridge University Press, Cambridge, 2000.

[44] P. M. Chaikin and T. C. Lubensky. *Principles of Condensed Matter Physics*. Cambridge University Press, Cambridge, 1995.

[45] Leo P. Kadanoff. Scaling laws for ising models near T_c. *Phys. Phys. Fiz.*, 2(6):263–272, June 1966.

[46] Ernst Ising. Beitrag zur Theorie des Ferromagnetismus. *Zeitschrift für Phys.*, 31(1):253–258, February 1925.

[47] M. Gell-Mann and F. E. Low. Quantum Electrodynamics at Small Distances. *Phys. Rev.*, 95(5):1300–1312, September 1954.

[48] B. I. Halperin and P. C. Hohenberg. Scaling Laws for Dynamic Critical Phenomena. *Phys. Rev.*, 177(2):952–971, January 1969.

[49] K. Symanzik. Small distance behaviour in field theory and power counting. *Commun. Math. Phys.*, 18(3):227–246, September 1970.

[50] C. G. Bollini and J. J. Giambiagi. Dimensional renorinalization: The number of dimensions as a regularizing parameter. *Nuovo Cim.*, 12(1):20–26, February 1972.

[51] G. 't Hooft and M. Veltman. Regularization and renormalization of gauge fields. *Nucl. Phys. B*, 44(1):189–213, July 1972.

[52] Kenneth G. Wilson and Michael E. Fisher. Critical Exponents in 3.99 Dimensions. *Phys. Rev. Lett.*, 28(4):240–243, January 1972.

[53] Farid Taherkhani, Hamed Akbarzadeh, Hadi Abroshan, Shahram Ranjbar, Alessandro Fortunelli, and Gholamabbas Parsafar. Study of two dimensional anisotropic Ising models via a renormalization group approach. *Phys. A Stat. Mech. its Appl.*, 392(22):5604–5614, November 2013.

[54] D. Farsal, M. Snina, M. Badia, and M. Bennai. Critical Properties of Two-dimensional Anisotropic Ising Model on a Square Lattice. *J. Supercond. Nov. Magn.*, 30(8):2187–2195, August 2017.

[55] Leo P. Kadanoff, Wolfgang Götze, David Hamblen, Robert Hecth, E. A. S. Lewis, V. V. Palciauskas, Martin Rayl, and J. Swift. Static Phenomena Near Critical Points: Theory and Experiment. *Rev. Mod. Phys.*, 39(2):395–431, April 1967.

[56] P. C. Hohenberg and B. I. Halperin. Theory of dynamic critical phenomena. *Rev. Mod. Phys.*, 49(3):435–479, July 1977.

[57] Géza Ódor. Universality classes in nonequilibrium lattice systems. *Rev. Mod. Phys.*, 76(3):663–724, August 2004.

[58] Thomas F. Gallagher. *Rydberg Atoms*. Cambridge University Press, Cambridge, 1994.

[59] N. Šibalić, J.D. Pritchard, C.S. Adams, and K.J. Weatherill. ARC: An open-source library for calculating properties of alkali Rydberg atoms. *Comput. Phys. Commun.*, 220:319–331, November 2017.

[60] E. Urban, T. A. Johnson, T. Henage, L. Isenhower, D. D. Yavuz, T. G. Walker, and M. Saffman. Observation of Rydberg blockade between two atoms. *Nat. Phys.*, 5(2):110–114, February 2009.

[61] Martin Gärttner, Kilian P. Heeg, Thomas Gasenzer, and Jörg Evers. Dynamic formation of Rydberg aggregates at off-resonant excitation. *Phys. Rev. A*, 88(4):043410, October 2013.

[62] H. Schempp, G. Günter, M. Robert-de Saint-Vincent, C. S. Hofmann, D. Breyel, A. Komnik, D. W. Schönleber, M. Gärttner, J. Evers, S. Whitlock, and M. Weidemüller. Full Counting Statistics of Laser Excited Rydberg Aggregates in a One-Dimensional Geometry. *Phys. Rev. Lett.*, 112(1):013002, January 2014.

[63] A. Urvoy, F. Ripka, I. Lesanovsky, D. Booth, J. P. Shaffer, T. Pfau, and R. Löw. Strongly Correlated Growth of Rydberg Aggregates in a Vapor Cell. *Phys. Rev. Lett.*, 114(20):203002, May 2015.

[64] E. A. Goldschmidt, T. Boulier, R. C. Brown, S. B. Koller, J. T. Young, A. V. Gorshkov, S. L. Rolston, and J. V. Porto. Anomalous Broadening in Driven Dissipative Rydberg Systems. *Phys. Rev. Lett.*, 116(11):113001, March 2016.

[65] H. Deng, G. Weihs, C. Santori, J. Bloch, and Y. Yamamoto. Condensation of Semiconductor Microcavity Exciton Polaritons. *Science*, 298(5591):199, October 2002.

[66] J. Kasprzak, M. Richard, S. Kundermann, A. Baas, P. Jeambrun, J. M. J. Keeling, F. M. Marchetti, M. H. Szymańska, R. André, J. L. Staehli, V. Savona, P. B. Littlewood, B. Deveaud, and L. S. Dang. Bose-Einstein condensation of exciton polaritons. *Nature*, 443(7110):409, September 2006.

[67] M. H. Szymańska, J. Keeling, and P. B. Littlewood. Nonequilibrium Quantum Condensation in an Incoherently Pumped Dissipative System. *Phys. Rev. Lett.*, 96:230602, June 2006.

[68] T. Byrnes, N. Y. Kim, and Y. Yamamoto. Exciton-polariton condensates. *Nat. Phys.*, 10(11):803, October 2014.

[69] S. R. K. Rodriguez, A. Amo, I. Sagnes, L. Le Gratiet, E. Galopin, A. Lemaître, and J. Bloch. Interaction-induced hopping phase in driven-dissipative coupled photonic microcavities. *Nat. Commun.*, 7:11887, June 2016.

[70] S. R. K. Rodriguez, W. Casteels, F. Storme, N. Carlon Zambon, I. Sagnes, L. Le Gratiet, E. Galopin, A. Lemaître, A. Amo, C. Ciuti, and J. Bloch. Probing a Dissipative Phase Transition via Dynamical Optical Hysteresis. *Phys. Rev. Lett.*, 118(24):247402, June 2017.

[71] J. G. Bohnet, B. C. Sawyer, J. W. Britton, M. L. Wall, A. M. Rey, M. Foss-Feig, and J. J. Bollinger. Quantum spin dynamics and entanglement generation with hundreds of trapped ions. *Science*, 352(6291):1297, June 2016.

[72] P. Schindler, M. Müller, D. Nigg, J. T. Barreiro, E. A. Martinez, M. Hennrich, T. Monz, S. Diehl, P. Zoller, and R. Blatt. Quantum simulation of dynamical maps with trapped ions. *Nat. Phys.*, 9(6):361, May 2013.

[73] T. Peyronel, O. Firstenberg, Q.-Y. Liang, S. Hofferberth, A. V. Gorshkov, T. Pohl, M. D. Lukin, and V. Vuletić. Quantum nonlinear optics with single photons enabled by strongly interacting atoms. *Nature (London)*, 488:57, July 2012.

[74] O. Firstenberg, T. Peyronel, Q.-Y. Liang, A. V. Gorshkov, M. D. Lukin, and V. Vuletić. Attractive photons in a quantum nonlinear medium. *Nature (London)*, 502:71, October 2013.

[75] C. Carr, R. Ritter, C. G. Wade, C. S. Adams, and K. J. Weatherill. Nonequilibrium Phase Transition in a Dilute Rydberg Ensemble. *Phys. Rev. Lett.*, 111(11):113901, September 2013.

[76] N. Malossi, M. M. Valado, S. Scotto, P. Huillery, P. Pillet, D. Ciampini, E. Arimondo, and O. Morsch. Full Counting Statistics and Phase Diagram of a Dissipative Rydberg Gas. *Phys. Rev. Lett.*, 113(2):023006, July 2014.

[77] Mattias Fitzpatrick, Neereja M. Sundaresan, Andy C. Y. Li, Jens Koch, and Andrew A. Houck. Observation of a Dissipative Phase Transition in a One-Dimensional Circuit QED Lattice. *Phys. Rev. X*, 7(1):011016, February 2017.

[78] Aditi Mitra, So Takei, Yong Baek Kim, and A. J. Millis. Nonequilibrium Quantum Criticality in Open Electronic Systems. *Phys. Rev. Lett.*, 97(23):236808, December 2006.

[79] M. Wouters and I. Carusotto. Absence of long-range coherence in the parametric emission of photonic wires. *Phys. Rev. B*, 74(24):245316, December 2006.

[80] Alexandre Le Boité, Giuliano Orso, and Cristiano Ciuti. Steady-State Phases and Tunneling-Induced Instabilities in the Driven Dissipative Bose-Hubbard Model. *Phys. Rev. Lett.*, 110(23):233601, June 2013.

[81] Hendrik Weimer. Variational Principle for Steady States of Dissipative Quantum Many-Body Systems. *Phys. Rev. Lett.*, 114(4):040402, January 2015.

[82] M. Foss-Feig, P. Niroula, J. T. Young, M. Hafezi, A. V. Gorshkov, R. M. Wilson, and M. F. Maghrebi. Emergent equilibrium in many-body optical bistability. *Phys. Rev. A*, 95(4):043826, April 2017.

[83] Filippo Vicentini, Fabrizio Minganti, Riccardo Rota, Giuliano Orso, and Cristiano Ciuti. Critical slowing down in driven-dissipative Bose-Hubbard lattices. *Phys. Rev. A*, 97(1):013853, January 2018.

[84] C. Carr, R. Ritter, C. G. Wade, C. S. Adams, and K. J. Weatherill. Nonequilibrium Phase Transition in a Dilute Rydberg Ensemble. *Phys. Rev. Lett.*, 111:113901, September 2013.

[85] Vincent R. Overbeck, Mohammad F. Maghrebi, Alexey V. Gorshkov, and Hendrik Weimer. Multicritical behavior in dissipative Ising models. *Phys. Rev. A*, 95(4):042133, April 2017.

[86] Matteo Marcuzzi, Emanuele Levi, Sebastian Diehl, Juan P. Garrahan, and Igor Lesanovsky. Universal Nonequilibrium Properties of Dissipative Rydberg Gases. *Phys. Rev. Lett.*, 113(21):210401, November 2014.

[87] Mohammad F. Maghrebi and Alexey V. Gorshkov. Nonequilibrium many-body steady states via Keldysh formalism. *Phys. Rev. B*, 93(1):014307, January 2016.

[88] E. T. Owen, J. Jin, D. Rossini, R. Fazio, and M. J. Hartmann. Quantum correlations and limit cycles in the driven-dissipative Heisenberg lattice. *New J. Phys.*, 20(4):045004, April 2018.

[89] Ching-Kit Chan, Tony E. Lee, and Sarang Gopalakrishnan. Limit-cycle phase in driven-dissipative spin systems. *Phys. Rev. A*, 91(5):051601, May 2015.

[90] Ryan M. Wilson, Khan W. Mahmud, Anzi Hu, Alexey V. Gorshkov, Mohammad Hafezi, and Michael Foss-Feig. Collective phases of strongly interacting cavity photons. *Phys. Rev. A*, 94(3):033801, September 2016.

[91] Tony E. Lee, H. Häffner, and M. C. Cross. Antiferromagnetic phase transition in a nonequilibrium lattice of Rydberg atoms. *Phys. Rev. A*, 84(3):031402, September 2011.

[92] Tony E. Lee, Sarang Gopalakrishnan, and Mikhail D. Lukin. Unconventional Magnetism via Optical Pumping of Interacting Spin Systems. *Phys. Rev. Lett.*, 110(25):257204, June 2013.

[93] Jiasen Jin, Davide Rossini, Rosario Fazio, Martin Leib, and Michael J. Hartmann. Photon Solid Phases in Driven Arrays of Nonlinearly Coupled Cavities. *Phys. Rev. Lett.*, 110(16):163605, April 2013.

[94] Jiasen Jin, Davide Rossini, Martin Leib, Michael J. Hartmann, and Rosario Fazio. Steady-state phase diagram of a driven QED-cavity array with cross-Kerr nonlinearities. *Phys. Rev. A*, 90(2):023827, August 2014.

[95] Michael Hoening, Wildan Abdussalam, Michael Fleischhauer, and Thomas Pohl. Antiferromagnetic long-range order in dissipative Rydberg lattices. *Phys. Rev. A*, 90(2):021603, August 2014.

[96] L. M. Sieberer, S. D. Huber, E. Altman, and S. Diehl. Dynamical Critical Phenomena in Driven-Dissipative Systems. *Phys. Rev. Lett.*, 110(19):195301, May 2013.

[97] Uwe C. Täuber and Sebastian Diehl. Perturbative Field-Theoretical Renormalization Group Approach to Driven-Dissipative Bose-Einstein Criticality. *Phys. Rev. X*, 4(2):021010, April 2014.

[98] Ehud Altman, Lukas M. Sieberer, Leiming Chen, Sebastian Diehl, and John Toner. Two-Dimensional Superfluidity of Exciton Polaritons Requires Strong Anisotropy. *Phys. Rev. X*, 5(1):011017, February 2015.

[99] L M Sieberer, M Buchhold, and S Diehl. Keldysh field theory for driven open quantum systems. *Reports Prog. Phys.*, 79(9):096001, September 2016.

[100] G. Roumpos, M. Lohse, W. H. Nitsche, J. Keeling, M. H. Szymanska, P. B. Littlewood, A. Loffler, S. Hofling, L. Worschech, A. Forchel, and Y. Yamamoto. Power-law decay of the spatial correlation function in exciton-polariton condensates. *Proc. Natl. Acad. Sci. USA*, 109(17):6467–6472, April 2012.

[101] Wolfgang H. Nitsche, Na Young Kim, Georgios Roumpos, Christian Schneider, Martin Kamp, Sven Höfling, Alfred Forchel, and Yoshihisa Yamamoto. Algebraic order and the Berezinskii-Kosterlitz-Thouless transition in an exciton-polariton gas. *Phys. Rev. B*, 90(20):205430, November 2014.

[102] Jamir Marino and Sebastian Diehl. Driven Markovian Quantum Criticality. *Phys. Rev. Lett.*, 116(7):070407, February 2016.

[103] Emanuele G. Dalla Torre, Eugene Demler, Thierry Giamarchi, and Ehud Altman. Quantum critical states and phase transitions in the presence of non-equilibrium noise. *Nat. Phys.*, 6(10):806–810, October 2010.

[104] H. F. H. Cheung, Y. S. Patil, and M. Vengalattore. Emergent phases and critical behavior in a non-Markovian open quantum system. *Phys. Rev. A*, 97(5):052116, May 2018.

[105] Riccardo Rota, Fabrizio Minganti, Cristiano Ciuti, and Vincenzo Savona. Quantum Critical Regime in a Quadratically Driven Nonlinear Photonic Lattice. *Phys. Rev. Lett.*, 122(11):110405, March 2019.

[106] K. E. Bassler and B. Schmittmann. Critical Dynamics of Nonconserved Ising-Like Systems. *Phys. Rev. Lett.*, 73(25):3343–3346, December 1994.

[107] P. L. Garrido and J. Marro. Effective Hamiltonian description of nonequilibrium spin systems. *Phys. Rev. Lett.*, 62(17):1929–1932, April 1989.

[108] Jian Sheng Wang and Joel L. Lebowitz. Phase transitions and universality in nonequilibrium steady states of stochastic Ising models. *J. Stat. Phys.*, 51(5-6):893–906, June 1988.

[109] M. C. Marques. Critical behaviour of the non-equilibrium Ising model with locally competing temperatures. *J. Phys. A*, 22(20):4493–4497, October 1989.

[110] M.C. Marques. Nonequilibrium Ising model with competing dynamics: A MFRG approach. *Phys. Lett. A*, 145(6-7):379–382, April 1990.

[111] T. Tome, M J de Oliveira, and M. A. Santos. Non-equilibrium Ising model with competing Glauber dynamics. *J. Phys. A*, 24(15):3677–3686, August 1991.

[112] M J de Oliveira, J F F Mendes, and M. A. Santos. Nonequilibrium spin models with Ising universal behaviour. *J. Phys. A*, 26(10):2317–2324, May 1993.

[113] A. Achahbar, J. J. Alonso, and M. A. Muñoz. Simple nonequilibrium extension of the Ising model. *Phys. Rev. E*, 54(5):4838–4843, November 1996.

[114] Mauricio Godoy and Wagner Figueiredo. Nonequilibrium antiferromagnetic mixed-spin Ising model. *Phys. Rev. E*, 66(3):036131, September 2002.

[115] Thomas Risler, Jacques Prost, and Frank Jülicher. Universal Critical Behavior of Noisy Coupled Oscillators. *Phys. Rev. Lett.*, 93:175702, October 2004.

[116] Thomas Risler, Jacques Prost, and Frank Jülicher. Universal critical behavior of noisy coupled oscillators: A renormalization group study. *Phys. Rev. E*, 72:016130, July 2005.

[117] G. Grinstein, D.-H. Lee, and Subir Sachdev. Conservation laws, anisotropy, and "self-organized criticality" in noisy nonequilibrium systems. *Phys. Rev. Lett.*, 64:1927–1930, April 1990.

[118] Pedro L. Garrido, Joel L. Lebowitz, Christian Maes, and Herbert Spohn. Long-range correlations for conservative dynamics. *Phys. Rev. A*, 42:1954–1968, August 1990.

[119] Z Cheng, P. L Garrido, J. L Lebowitz, and J. L Vallés. Long-Range Correlations in Stationary Nonequilibrium Systems with Conservative Anisotropic Dynamics. *Europhys. Lett.*, 14(6):507–513, March 1991.

[120] Uwe C. Täuber and Zoltán Rácz. Critical behavior of O(n)-symmetric systems with reversible mode-coupling terms: Stability against detailed-balance violation. *Phys. Rev. E*, 55(4):4120–4136, April 1997.

[121] Uwe C. Täuber, Vamsi K. Akkineni, and Jaimie E. Santos. Effects of Violating Detailed Balance on Critical Dynamics. *Phys. Rev. Lett.*, 88(4):045702, January 2002.

[122] M. Kounalakis, C. Dickel, A. Bruno, N. K. Langford, and G. A. Steele. Tuneable hopping and nonlinear cross-Kerr interactions in a high-coherence superconducting circuit. *npj Quantum Inf.*, 4(1):38, December 2018.

[123] Sarang Gopalakrishnan, Benjamin L. Lev, and Paul M. Goldbart. Atom-light crystallization of Bose-Einstein condensates in multimode cavities: Nonequilibrium classical and quantum phase transitions, emergent lattices, supersolidity, and frustration. *Phys. Rev. A*, 82(4):043612, October 2010.

[124] Emanuele G. Dalla Torre, Eugene Demler, Thierry Giamarchi, and Ehud Altman. Dynamics and universality in noise-driven dissipative systems. *Phys. Rev. B*, 85(18):184302, May 2012.

[125] Emanuele G. Dalla Torre, Sebastian Diehl, Mikhail D. Lukin, Subir Sachdev, and Philipp Strack. Keldysh approach for nonequilibrium phase transitions in quantum optics: Beyond the Dicke model in optical cavities. *Phys. Rev. A*, 87(2):023831, February 2013.

[126] L. M. Sieberer, S. D. Huber, E. Altman, and S. Diehl. Nonequilibrium functional renormalization for driven-dissipative Bose-Einstein condensation. *Phys. Rev. B*, 89(13):134310, April 2014.

[127] Mohammad F. Maghrebi. Fragile fate of driven-dissipative XY phase in two dimensions. *Phys. Rev. B*, 96(17):174304, November 2017.

[128] Uwe C. Täuber. *Critical Dynamics: A Field Theory Approach to Equilibrium and Non-Equilibrium Scaling Behavior*. 2014.

[129] Didier Sornette. Discrete-scale invariance and complex dimensions. *Phys. Rep.*, 297(5):239–270, April 1998.

[130] Michael E. Fisher and David R. Nelson. Spin Flop, Supersolids, and Bicritical and Tetracritical Points. *Phys. Rev. Lett.*, 32(24):1350–1353, June 1974.

[131] David R. Nelson, J. M. Kosterlitz, and Michael E. Fisher. Renormalization-Group Analysis of Bicritical and Tetracritical Points. *Phys. Rev. Lett.*, 33(14):813–817, September 1974.

[132] Alastair D. Bruce and Amnon Aharony. Coupled order parameters, symmetry-breaking irrelevant scaling fields, and tetracritical points. *Phys. Rev. B*, 11(1):478–499, January 1975.

[133] J. M. Kosterlitz, David R. Nelson, and Michael E. Fisher. Bicritical and tetracritical points in anisotropic antiferromagnetic systems. *Phys. Rev. B*, 13(1):412–432, January 1976.

[134] R. Folk, Yu Holovatch, and G. Moser. Field theory of bicritical and tetracritical points. I. Statics. *Phys. Rev. E*, 78(4):041124, October 2008.

[135] R. Folk, Yu Holovatch, and G. Moser. Field theory of bicritical and tetracritical points. II. Relaxational dynamics. *Phys. Rev. E*, 78(4):041125, October 2008.

[136] Astrid Eichhorn, David Mesterházy, and Michael M. Scherer. Multicritical behavior in models with two competing order parameters. *Phys. Rev. E*, 88(4):042141, October 2013.

[137] Daniel S. Rokhsar and B. G. Kotliar. Gutzwiller projection for bosons. *Phys. Rev. B*, 44(18):10328–10332, November 1991.

[138] Sebastian Diehl, Andrea Tomadin, Andrea Micheli, Rosario Fazio, and Peter Zoller. Dynamical Phase Transitions and Instabilities in Open Atomic Many-Body Systems. *Phys. Rev. Lett.*, 105(1):015702, July 2010.

[139] D. Jaksch, J. I. Cirac, P. Zoller, S. L. Rolston, R. Côté, and M. D. Lukin. Fast Quantum Gates for Neutral Atoms. *Phys. Rev. Lett.*, 85(10):2208–2211, September 2000.

[140] M D Lukin, M Fleischhauer, R Cote, L M Duan, D Jaksch, J I Cirac, and P Zoller. Dipole Blockade and Quantum Information Processing in Mesoscopic Atomic Ensembles. *Phys. Rev. Lett.*, 87(3):037901, June 2001.

[141] C. Ates, T. Pohl, T. Pattard, and J. M. Rost. Antiblockade in Rydberg Excitation of an Ultracold Lattice Gas. *Phys. Rev. Lett.*, 98(2):023002, January 2007.

[142] Thomas Amthor, Christian Giese, Christoph S. Hofmann, and Matthias Weidemüller. Evidence of Antiblockade in an Ultracold Rydberg Gas. *Phys. Rev. Lett.*, 104(1):013001, January 2010.

[143] Peter D. Drummond and Kaled Dechoum. Universality of quantum critical dynamics in a planar optical parametric oscillator. *Phys. Rev. Lett.*, 95:083601, August 2005.

[144] Kaled Dechoum, Laura Rosales-Zárate, and Peter D. Drummond. Critical fluctuations in an optical parametric oscillator: when light behaves like magnetism. *J. Opt. Soc. Am. B*, 33(5):871, May 2016.

[145] J. HARLIM and W. F. LANGFORD. THE CUSP–HOPF BIFURCATION. *Int. J. Bifurc. Chaos*, 17(08):2547–2570, August 2007.

[146] F. J. Wegner. Some invariance properties of the renormalization group. *J. Phys. C Solid State Phys.*, 7(12):2098–2108, June 1974.

[147] C. De Dominicis and L. Peliti. Deviations from Dynamic Scaling in Helium and Antiferromagnets. *Phys. Rev. Lett.*, 38(9):505–508, February 1977.

[148] Volker Dohm and Hans-Karl Janssen. Dynamic Scaling near Bicritical Points. *Phys. Rev. Lett.*, 39(15):946–949, October 1977.

[149] Jean Zinn-Justin. *Quantum field theory and critical phenomena*. Clarendon Press, 4th edition, 1996.

[150] JAMES A. FEIGENBAUM and PETER G.O. FREUND. DISCRETE SCALE INVARIANCE IN STOCK MARKETS BEFORE CRASHES. *Int. J. Mod. Phys. B*, 10(27):3737–3745, December 1996.

[151] Didier Sornette and Charles G. Sammis. Complex Critical Exponents from Renormalization Group Theory of Earthquakes: Implications for Earthquake Predictions. *J. Phys. I*, 5(5):607–619, May 1995.

[152] Dragi Karevski and Loïc Turban. Log-periodic corrections to scaling: exact results for aperiodic Ising quantum chains. *J. Phys. A*, 29(13):3461–3470, July 1996.

[153] G. Jona-Lasinio. The renormalization group: A probabilistic view. *Nuovo Cim. B Ser. 11*, 26(1):99–119, March 1975.

[154] M. Nauenberg. Scaling representation for critical phenomena. *J. Phys. A*, 8(6):925–928, 1975.

[155] T. Niemeijer and J. M. J. Van Leeuwen. Renormalization Theory for Ising Like Spin Systems. In *Phase Transitions and Critical Phenomena*, volume 6, pages 425–505, 1976.

[156] Jamir Marino and Sebastian Diehl. Quantum dynamical field theory for nonequilibrium phase transitions in driven open systems. *Phys. Rev. B*, 94:085150, August 2016.

[157] Jeff Maki, Li-Ming Zhao, and Fei Zhou. Nonperturbative dynamical effects in nearly-scale-invariant systems: The action of breaking scale invariance. *Phys. Rev. A*, 98(1):013602, July 2018.

[158] Eric Braaten and H.-W. Hammer. Universality in few-body systems with large scattering length. *Phys. Rep.*, 428(5-6):259–390, June 2006.

[159] V. Efimov. Energy levels arising from resonant two-body forces in a three-body system. *Phys. Lett. B*, 33(8):563–564, December 1970.

[160] A. Leclair, J. M. Roman, and Germán Sierra. Russian Doll Renormalization Group, Kosterlitz-Thouless Flows, and the Cyclic sine-Gordon model. *Nucl. Phys. B*, 675(3):584–606, January 2003.

[161] David B. Kaplan, Jong-Wan Lee, Dam T. Son, and Mikhail A. Stephanov. Conformality lost. *Phys. Rev. D*, 80(12):125005, December 2009.

[162] Amnon Aharony. Critical properties of random and constrained dipolar magnets. *Phys. Rev. B*, 12:1049–1056, August 1975.

[163] Jing-Huei Chen and T. C. Lubensky. Mean field and ϵ-expansion study of spin glasses. *Phys. Rev. B*, 16:2106–2114, September 1977.

[164] D.E. Khmelnitskii. Impurity effect on the phase transition at $T = 0$ in magnets. Critical oscillations in corrections to the scaling laws. *Phys. Lett. A*, 67(1):59, July 1978.

[165] Abel Weinrib and B. I. Halperin. Critical phenomena in systems with long-range-correlated quenched disorder. *Phys. Rev. B*, 27:413–427, January 1983.

[166] Daniel Boyanovsky and John L. Cardy. Critical behavior of m-component magnets with correlated impurities. *Phys. Rev. B*, 26:154–170, July 1982.

[167] Sean A. Hartnoll, David M. Ramirez, and Jorge E. Santos. Thermal conductivity at a disordered quantum critical point. *J. High Energy Phys.*, 2016(4):1–24, April 2016.

[168] Alexandre Blais, Jay Gambetta, A. Wallraff, D. I. Schuster, S. M. Girvin, M. H. Devoret, and R. J. Schoelkopf. Quantum-information processing with circuit quantum electrodynamics. *Phys. Rev. A*, 75(3):032329, March 2007.

[169] M. H. Devoret and R. J. Schoelkopf. Superconducting Circuits for Quantum Information: An Outlook. *Science*, 339(6124):1169–1174, March 2013.

[170] A. Tomadin and Rosario Fazio. Many-body phenomena in QED-cavity arrays [Invited]. *J. Opt. Soc. Am. B*, 27(6):A130–136, April 2010.

[171] Borja Peropadre, David Zueco, Friedrich Wulschner, Frank Deppe, Achim Marx, Rudolf Gross, and Juan José García-Ripoll. Tunable coupling engineering between superconducting resonators: From sidebands to effective gauge fields. *Phys. Rev. B*, 87(13):134504, April 2013.

[172] Matteo Biondi, Gianni Blatter, Hakan E. Türeci, and Sebastian Schmidt. Nonequilibrium gas-liquid transition in the driven-dissipative photonic lattice. *Phys. Rev. A*, 96(4):043809, October 2017.

[173] F. Iemini, A. Russomanno, J. Keeling, M. Schirò, M. Dalmonte, and R. Fazio. Boundary Time Crystals. *Phys. Rev. Lett.*, 121(3):035301, July 2018.

[174] Shwetank Kumar and David P. DiVincenzo. Exploiting Kerr cross nonlinearity in circuit quantum electrodynamics for nondemolition measurements. *Phys. Rev. B*, 82(1):014512, July 2010.

[175] Io-Chun Hoi, Anton F. Kockum, Tauno Palomaki, Thomas M. Stace, Bixuan Fan, Lars Tornberg, Sankar R. Sathyamoorthy, Göran Johansson, Per Delsing, and C. M. Wilson. Giant Cross–Kerr Effect for Propagating Microwaves Induced by an Artificial Atom. *Phys. Rev. Lett.*, 111(5):053601, August 2013.

[176] E. T. Holland, B. Vlastakis, R. W. Heeres, M. J. Reagor, U. Vool, Z. Leghtas, L. Frunzio, G. Kirchmair, M. H. Devoret, M. Mirrahimi, and R. J. Schoelkopf. Single-Photon-Resolved Cross-Kerr Interaction for Autonomous Stabilization of Photon-Number States. *Phys. Rev. Lett.*, 115(18):180501, October 2015.

[177] Andy C. Y. Li and Jens Koch. Mapping repulsive to attractive interaction in driven–dissipative quantum systems. *New J. Phys.*, 19(11):115010, November 2017.

[178] Kristian Baumann, Christine Guerlin, Ferdinand Brennecke, and Tilman Esslinger. Dicke quantum phase transition with a superfluid gas in an optical cavity. *Nature (London)*, 464(7293):1301, April 2010.

[179] R Mottl, F Brennecke, K Baumann, R Landig, T Donner, and T Esslinger. Roton-Type Mode Softening in a Quantum Gas with Cavity-Mediated Long-Range Interactions. *Science*, 336(6088):1570–1573, June 2012.

[180] Julian Léonard, Andrea Morales, Philip Zupancic, Tilman Esslinger, and Tobias Donner. Supersolid formation in a quantum gas breaking a continuous translational symmetry. *Nature (London)*, 543(7643):87–90, March 2017.

[181] Julian Léonard, Andrea Morales, Philip Zupancic, Tobias Donner, and Tilman Esslinger. Monitoring and manipulating Higgs and Goldstone modes in a supersolid quantum gas. *Science*, 358(6369):1415–1418, December 2017.

[182] T. Pohl, C. S. Adams, and H. R. Sadephpour. Cold Rydberg gases and ultracold plasmas. *J. Phys. B*, 44(18):180201, September 2011.

[183] Michael Höning, Dominik Muth, David Petrosyan, and Michael Fleischhauer. Steady-state crystallization of Rydberg excitations in an optically driven lattice gas. *Phys. Rev. A*, 87(2):023401, February 2013.

[184] Tony E. Lee, H. Häffner, and M. C. Cross. Collective Quantum Jumps of Rydberg Atoms. *Phys. Rev. Lett.*, 108(2):023602, January 2012.

[185] A. Dauphin, M. Müller, and M. A. Martin-Delgado. Rydberg-atom quantum simulation and Chern-number characterization of a topological Mott insulator. *Phys. Rev. A*, 86(5):053618, November 2012.

[186] R. M. W. van Bijnen and T. Pohl. Quantum Magnetism and Topological Ordering via Rydberg Dressing near Förster Resonances. *Phys. Rev. Lett.*, 114(24):243002, June 2015.

[187] Hendrik Weimer, Markus Müller, Igor Lesanovsky, Peter Zoller, and Hans Peter Büchler. A Rydberg quantum simulator. *Nat. Phys.*, 6(5):382–388, May 2010.

[188] N. Henkel, R. Nath, and T. Pohl. Three-Dimensional Roton Excitations and Supersolid Formation in Rydberg-Excited Bose-Einstein Condensates. *Phys. Rev. Lett.*, 104(19):195302, May 2010.

[189] Y.-Y. Jau, A. M. Hankin, T. Keating, I. H. Deutsch, and G. W. Biedermann. Entangling atomic spins with a Rydberg-dressed spin-flip blockade. *Nat. Phys.*, 12(1):71–74, January 2016.

[190] Alexander W. Glaetzle, Marcello Dalmonte, Rejish Nath, Christian Gross, Immanuel Bloch, and Peter Zoller. Designing Frustrated Quantum Magnets with Laser-Dressed Rydberg Atoms. *Phys. Rev. Lett.*, 114(17):173002, April 2015.

[191] G. Pupillo, A. Micheli, M. Boninsegni, I. Lesanovsky, and P. Zoller. Strongly Correlated Gases of Rydberg-Dressed Atoms: Quantum and Classical Dynamics. *Phys. Rev. Lett.*, 104(22):223002, June 2010.

[192] Adriano Angelone, Fabio Mezzacapo, and Guido Pupillo. Superglass Phase of Interaction-Blockaded Gases on a Triangular Lattice. *Phys. Rev. Lett.*, 116(13):135303, April 2016.

[193] Jens Honer, Hendrik Weimer, Tilman Pfau, and Hans Peter Büchler. Collective Many-Body Interaction in Rydberg Dressed Atoms. *Phys. Rev. Lett.*, 105(16):160404, October 2010.

[194] J. E. Johnson and S. L. Rolston. Interactions between Rydberg-dressed atoms. *Phys. Rev. A*, 82(3):033412, September 2010.

[195] S. Helmrich, A. Arias, N. Pehoviak, and S. Whitlock. Two-body interactions and decay of three-level Rydberg-dressed atoms. *J. Phys. B*, 49(3):03LT02, February 2016.

[196] A. W. Glaetzle, R. Nath, B. Zhao, G. Pupillo, and P. Zoller. Driven-dissipative dynamics of a strongly interacting Rydberg gas. *Phys. Rev. A*, 86(4):043403, October 2012.

[197] J. A. Aman, B. J. DeSalvo, F. B. Dunning, T. C. Killian, S. Yoshida, and J. Burgdörfer. Trap losses induced by near-resonant Rydberg dressing of cold atomic gases. *Phys. Rev. A*, 93(4):043425, April 2016.

[198] T. Boulier, E. Magnan, C. Bracamontes, J. Maslek, E. A. Goldschmidt, J. T. Young, A. V. Gorshkov, S. L. Rolston, and J. V. Porto. Spontaneous avalanche dephasing in large Rydberg ensembles. *Phys. Rev. A*, 96(5):053409, November 2017.

[199] Johannes Zeiher, Rick van Bijnen, Peter Schauß, Sebastian Hild, Jae-Yoon Choi, Thomas Pohl, Immanuel Bloch, and Christian Gross. Many-body interferometry of a Rydberg-dressed spin lattice. *Nat. Phys.*, 12(12):1095–1099, December 2016.

[200] D. Tong, S. M. Farooqi, J. Stanojevic, S. Krishnan, Y. P. Zhang, R. Côté, E. E. Eyler, and P. L. Gould. Local Blockade of Rydberg Excitation in an Ultracold Gas. *Phys. Rev. Lett.*, 93(6):063001, August 2004.

[201] Rolf Heidemann, Ulrich Raitzsch, Vera Bendkowsky, Björn Butscher, Robert Löw, Luis Santos, and Tilman Pfau. Evidence for Coherent Collective Rydberg Excitation in the Strong Blockade Regime. *Phys. Rev. Lett.*, 99(16):163601, October 2007.

[202] Hendrik Weimer, Robert Löw, Tilman Pfau, and Hans Peter Büchler. Quantum Critical Behavior in Strongly Interacting Rydberg Gases. *Phys. Rev. Lett.*, 101(25):250601, December 2008.

[203] Robert Löw, Hendrik Weimer, Ulrich Krohn, Rolf Heidemann, Vera Bendkowsky, Björn Butscher, Hans Peter Büchler, and Tilman Pfau. Universal scaling in a strongly interacting Rydberg gas. *Phys. Rev. A*, 80(3):033422, September 2009.

[204] Igor Lesanovsky and Juan P. Garrahan. Kinetic Constraints, Hierarchical Relaxation, and Onset of Glassiness in Strongly Interacting and Dissipative Rydberg Gases. *Phys. Rev. Lett.*, 111(21):215305, November 2013.

[205] Rüdiger Schack and Axel Schenzle. Moment hierarchies and cumulants in quantum optics. *Phys. Rev. A*, 41(7):3847–3852, April 1990.

[206] D Meiser and M J Holland. Steady-state superradiance with alkaline-earth-metal atoms. *Phys. Rev. A*, 81(3):033847, March 2010.

[207] Kathrin Henschel, Johannes Majer, Jörg SchmiedMayer, and Helmut Ritsch. Cavity QED with an ultracold ensemble on a chip: Prospects for strong magnetic coupling at finite temperatures. *Phys. Rev. A*, 82(3):033810, September 2010.

[208] B Zhu, J SchachenMayer, M Xu, F Herrera, J G Restrepo, M J Holland, and A M Rey. Synchronization of interacting quantum dipoles. *New J. Phys.*, 17(8):083063, September 2015.

[209] Fabian Letscher, Oliver Thomas, Thomas Niederprüm, Herwig Ott, and Michael Fleischhauer. Anomalous excitation facilitation in inhomogeneously broadened Rydberg gases. *Phys. Rev. A*, 95(2):023410, February 2017.

[210] F. Letscher, O. Thomas, T. Niederprüm, M. Fleischhauer, and H. Ott. Bistability Versus Metastability in Driven Dissipative Rydberg Gases. *Phys. Rev. X*, 7(2):021020, May 2017.

[211] Jean Dalibard, Yvan Castin, and Klaus Mølmer. Wave-function approach to dissipative processes in quantum optics. *Phys. Rev. Lett.*, 68(5):580–583, February 1992.

[212] R. Dum, P. Zoller, and H. Ritsch. Monte Carlo simulation of the atomic master equation for spontaneous emission. *Phys. Rev. A*, 45(7):4879–4887, April 1992.

[213] M. B. Plenio and P. L. Knight. The quantum-jump approach to dissipative dynamics in quantum optics. *Rev. Mod. Phys.*, 70(1):101–144, January 1998.

[214] Andrew J. Daley. Quantum trajectories and open many-body quantum systems. *Adv. Phys.*, 63(2):77–149, March 2014.

[215] Johannes Zeiher, Peter Schauß, Sebastian Hild, Tommaso Macrì, Immanuel Bloch, and Christian Gross. Microscopic Characterization of Scalable Coherent Rydberg Superatoms. *Phys. Rev. X*, 5(3):031015, August 2015.

[216] Jiasen Jin, Alberto Biella, Oscar Viyuela, Leonardo Mazza, Jonathan Keeling, Rosario Fazio, and Davide Rossini. Cluster Mean-Field Approach to the Steady-State Phase Diagram of Dissipative Spin Systems. *Phys. Rev. X*, 6(3):031011, July 2016.

[217] Crispin W. Gardiner. *Stochastic Methods: A Handbook for the Natural and Social Sciences*. Springer-Verlag Berlin Heidelberg, New York, 4th edition, 2009.

[218] Y.-J. Lin, R. Compton, A. Perry, W. Phillips, J. Porto, and I. Spielman. Bose-Einstein Condensate in a Uniform Light-Induced Vector Potential. *Phys. Rev. Lett.*, 102(13):130401, March 2009.